Fall 9-11-2018

OXYGEN AND SILVER-OXYGEN DEFECTS IN Ge2Se3 ELECTROCHEMICAL METALLIZATION BRIDGE MEMRISTORS

Jau-Tzuoo Chen
University of New Mexico

Jau-Tzuoo Chen
Candidate

Electrical and Computer Engineering
Department

This thesis is approved, and it is acceptable in quality and form for publication:

Approved by the Thesis Committee:

Dr. Marek Osinski, Chair

Dr. Mark Gilmore

Dr. Arthur Edwards

Dr. Susan Atlas

OXYGEN AND SILVER-OXYGEN DEFECTS IN Ge_2Se_3 ELECTROCHEMICAL METALLIZATION BRIDGE MEMRISTORS

by

Jau-Tzuoo Chen

B.S., Physics, Auburn University, 2011

THESIS

Submitted in Partial Fulfillment of the

Requirements for the Degree of

Master of Science

Electrical Engineering

The University of New Mexico

Albuquerque, New Mexico

December, 2018

DEDICATION

(This page intentionally left blank)

ACKNOWLEDGMENT

To the members of my thesis committee, Dr. Marek Osinski, Dr. Mark Gilmore, Dr. Arthur Edwards and Dr. Susan Atlas, I wish to hereby express my gratitude. The journey for this degree has been long and difficult, and I thank you for seeing it through to completion.

To Dr. Marek Osinski, my thesis committee chair, I want to thank you for several items. As a stranger, you decided to take on the committee chair role at such a late stage and help me complete this journey. As a mentor, no matter how brief, you have taught valuable lessons and acknowledged the value of my work. As a mediator, you are an integral part of in the final stages of this degree. I thank you for all this and more.

To Dr. Mark Gilmore, my academic advisor, you are the constant through this journey. In 2013, I could not get into any graduate school due to political circumstances. I came to Albuquerque because of you. You got me into the graduate program here, and I wanted to study under you with the recommendation of Dr. Edward Thomas. Throughout the years, I saw that you always had the best intentions. You have supported me, one way or another, through everything. I cannot express my gratitude of you supporting me for the last one and a half years of this journey. My only regret is I have not had the opportunity to formally study experimental plasma physics under you.

To Dr. Arthur Edwards, my research advisor, I thank you for exposing me to and teaching me quantum chemistry/electronic structure modelling. You have also greatly impacted me in technical writing during the thesis writing process. Your attitude and philosophy regarding scientific research and writing style are part of me as a scientist moving forward.

To Dr. Susan Atlas, teacher and editor, I thank you for teaching me quantum chemistry/density functional theory and your help in the thesis writing process. Your

scientific and technical rigor and writing style have greatly improved the thesis. Your writing style are part of me as well as a scientist moving forward.

To Dr. Andrew Pineda, research advisor, I thank you also for exposing me to and teaching me quantum chemistry/electronic structure modelling. Throughout the years, you have helped me greatly in computation specific areas. Your writing style are also part of me as a scientist moving forward.

To Angela Gonzales, my confidant, thank you for being there every step of the way. That is all I can say.

To Dinesh Mahadeo, Dr. Dustin Fisher, Dr. Jesse Mee and countless friends, acquaintances and peers, I thank you all for your help on this journey, your help in the thesis writing and defense preparation processes.

OXYGEN AND SILVER-OXYGEN DEFECTS IN Ge_2Se_3 ELECTROCHEMICAL METALLIZATION BRIDGE MEMRISTORS

by

Jau-Tzuoo Chen

B.S., Physics, Auburn University, 2011

M.S., Electrical Engineering, University of New Mexico, 2018

Abstract

We present density functional theory (DFT) calculations of oxygen and silver defects in a crystalline model of amorphous Ge_2Se_3. We studied defects arising from atomic oxygen and dioxygen, as well as interstitial silver and silver displacing germanium, following Campbell's conjecture on the mechanism of dendrite formation. For oxygen defect concentrations below 2%, we show that O_2 dissociates in Ge_2Se_3, oxygen atoms are immobile, and oxygen atoms do not cluster. Within this model, the most preferred oxygen defect in intrinsic Ge_2Se_3 is Ge-O-Ge bridge. We conclude that oxygen defects will not severely alter the electrical properties of Ge_2Se_3. Our results

on silver defects in Ge_2Se_3 agree with and extend previous work using a similar model; the two most preferred silver defect types are intralayer silver interstitial and silver displacement of germanium. We also studied the interaction between silver defects and the most preferred oxygen defect. We learned that discounting the highest defect concentrations, oxygen defects will not severely change the behavior of silver defects in Ge_2Se_3, but it will inhibit the formation of Ag-Ge dimers.

Contents

List of Figures

List of Tables

Chapter 1: Introduction

1.1 Device Background

Since Chua's exploration of memristors in 1971 [2], we have known that these non-volatile memory[1] technologies hold great promise in certain novel applications, such as artificial neurons for neuromorphic computing [4, 5], configuration memory in field-programmable gate arrays [6] and threshold logic [7]. Flash memory [3], the pervasive non-volatile memory technology, suffers from slow writing speed,[2] low endurance[3] and high write operation voltage[4] requirements [9]. Electrochemical metallization bridge (EMB)[5] memristors[6] are non-volatile memory technologies capable of replacing flash memory due to lower write operation voltage,[7] higher endurance[8] and competitive scalability [9] and write speed [9].

EMB memristor-based memory switches are based on ion motion and electrochemical reactions in their semiconductor layers [9, 11]. Campbell has been utilizing the

[1]Non-volatile memory retains its memory after being powercycled. For more information about non-volatile memory and flash memory, refer to Ref. [3].

[2]The 2007 International Technology Roadmap for Semiconductors (ITRS) Emerging Research Devices (ERD) chapter states that the write/erase times of floating-gate NAND are 1 ms/0.1 ms [8];Valov *et al.*[9] state that the write time of NAND flash is ~1 µs. Derbenwick and Brewer [10] wrote that write speeds of typical flash memories are around 10 µs to 2 ms. Regardless of this discrepancy, referencing again the Emerging Research Devices chapter, the write/erase times of stand-alone DRAM are 1 ns.

[3]DRAM's endurance is 10^{15} program/erase cycles [9]. The 2007 ITRS ERD chapter [8] states that the endurance of floating-gate NAND is 100,000 program/erase cycles.

[4]The 2007 ITRS ERD chapter [8] states that the write operation voltages of floating-gate NOR and NAND devices are 12 V and 15 V, respectively. The voltages of these two devices are by far the highest of all devices mentioned in the chapter.

[5]EMB is the official term used by the ITRS ERD chapter. The EMB memristor is one of four major categories of redox RAM technologies [6].

[6]EMB memristors are also known as ionic memristors [11], electrochemical metalization (ECM) cells [9] and condutive bridging random access memory (CBRAM) [12].

[7]In Ref. [13], the write/erase operation sweep voltages of self-directed channel (SDC) memristor are 0 to 1 V and 0 to -1 V, respectively. Campbell's SDC memristor is an EMB memristor and uses Ge_2Se_3, the chalcogenide material this thesis is about. Compared to the previously stated 15 V write operation voltage of floating-gate NAND, the write operation voltage requirement of SDC memristors is 15 times smaller.

[8]Campbell [13] demonstrated that the endurance of the SDC device is at least 1,000,000,000 program/erase cycles; this is much greater than the endurance of floating-gate NAND.

chalcogenide glass, Ge_2Se_3, as the electrolyte layer material and silver as the active metal in these memristors [13, 14, 15]. In addition to the usual metal-insulator-metal design, Campbell also included a SnSe metal-chalcogenide layer. EMB memristors of this layer composition are more reliable than ones that use selenium-rich Ge_xSe_{1-x}, with more consistent and lower threshold voltages [16]. A new class of the EMB memristor, the self-directed channel (SDC) memristor, using these layer compositions is operational immediately after an one-step fabrication through sputtering or evaporation and can operate continuously at 150 °C or greater [13].

Campbell *et al.* proposed that germanium dimers in Ge_2Se_3 play a major role in the write and erase processes; specifically, silver displacing germanium and leading to permanent Ag-Ge bonds that form paths for future write processes [13, 14, 15]. Edwards *et al.* performed theoretical studies to understand the electrochemistry of EMB memristors with the layer compositions mentioned. In Ref. [1], they performed density functional theory calculations to study silver defects in Ge_2Se_3 and emphasized germanium dimers. In Refs. [16, 17], calculations showed tin is attracted to paired electrons self-trapped on germanium dimers and can assist in forming Ag-Ge bonds.

1.2 EMB Memristor

To put the details of active metal ion motion and electrochemistry in the electrolyte in better context, we refer to Figure 1 for a simplified depiction of the operation of an EMB memristor. This memristor is constructed with three layers: an active metal electrode layer (shown in blue), a solid electrolyte layer (shown in yellow) and an inactive metal electrode layer (shown in gray) [9].

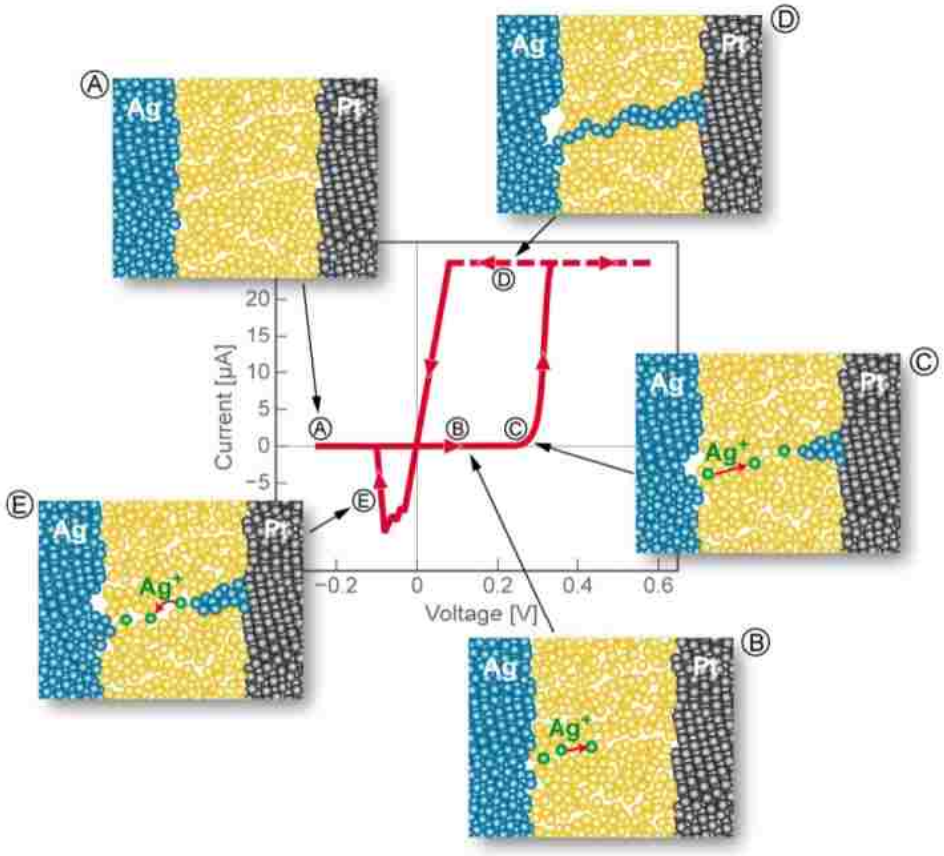

Figure 1: EMB memristor operation. This figure, taken from Ref. [9], displays simplified write (A-D) and erase (E) processes.

In Step A of Figure 1, the device is in its virgin state. When an electric field is applied through the device, atoms from the active metal layer oxidize[9] and travel through the electrolyte layer as shown in Step B [9]. Active metal ions deposit on the surface of the inactive metal electrode layer as shown in Step C [9]. The accompanying current-voltage plot of Figure 1 shows minimal current with increasing voltage from Step A to Step B due to lack of physical connection across the device. With repeated and concentrated deposition, a conductive metal dendrite forms across the electrolyte

[9]For our layer composition, the Ag donates an electron to the bulk Ge_2Se_3 and becomes Ag^+; bulk Ge_2Se_3 oxidizes Ag.

$$Ag \rightarrow Ag^+ + e^-$$

layer and connects the left and right[10] in a redox/oxidation process[11] as shown by Step C to Step D [9]. Referring to the current-voltage plot, the resistance of the device drops dramatically with this left to right connection [9]. Of course, the actual write process can be more complicated. During this process, active metal ions can interact and may permanently change the electrolyte layer [1], and the change affects future write and erase processes [9, 13, 14, 15, 17].

To break this left to right connection, an electric field is applied in the opposite direction, which returns active metal atoms to their original layer and causes disconnection as shown in Step D to Step E [9]. Shown in the current-voltage plot, the metal dendrite disconnection returns the current to zero. In short, the resistance, which is the memory of the device, depends on the continuity of the metal dendrite, and the continuity of the metal dendrite depends on the amount and duration of applied voltage [9]. However, the memory does not solely depend on the continuity of the dendrite; it also depends on the metal dendrite width, i.e. thick and thin dendrite respectively lead to lower and higher resistances. This means that after the connection, the write and erase processes need not involve dendrite continuity.

The memory[12] of the device can be read out by measuring the resistance with short and low-voltage pulses; in doing so, the read process does not disturb the actual memory of the device [9].

[10]Figure 1's orientation is active metal layer on the left and inactive metal layer on the right. Other publications may orientate the device from top to bottom.

[11]For our layer composition, Ag^+ acquires electrons from the bulk inactive metal and neutralizes; the bulk inactive metal reduces Ag^+. On the other hand, Ag^+ oxidizes the bulk inactive metal.

$$Ag^+ + e^- \rightarrow Ag$$

[12]For example, in binary, the on and off states.

1.3 Oxygen Defects in Ge_2Se_3

So far, we have briefly described some of the physics and chemistry of the basic/ideal memory mechanism of EMB memristors. In reality, the presence of impurities may negatively affect device operation. Slack *et al.* [18] have reported oxygen impurities and their effects in the semiconductors AlN and GaN. To date, we are not aware of any theoretical studies on oxygen defects in Ge_2Se_3, the electrolyte layer material we are interested in.

Concerned by the abundance and reactivity of oxygen, we were motivated to study the effects of oxygen on 1) electrical properties of Ge_2Se_3 and on 2) the behavior of silver within the Ge_2Se_3 environment to address potential disruption of device operation. Atomic oxygen and dioxygen/molecular oxygen, termed O_2 in this thesis, can disrupt device operation by directly changing the electrical properties of Ge_2Se_3 or by changing the behavior of silver solutes in Ge_2Se_3.

1.4 Overview

In Chapter 2, we briefly review the periodic quantum mechanical treatment used in these studies. Chapter 2 starts with density functional electronic structure theory (2.1.1 and 2.1.2) and geometry optimization (2.1.3). The chapter continues with additional frameworks, periodic approach (2.1.4) and pseudopotential theory (2.1.5). Discussions about defect modeling using a periodic approach (2.1.6) and calculation details (2.1.7) conclude the primary calculation topics. The chapter concludes with post-processing calculation topics, nudged elastic band method, a method to determine activation energy (2.1.8), and projected density of states (2.1.9).

In Chapter 3, we discuss the crystalline model of Ge_2Se_3 used by Edwards *et al.* in Refs. [1, 16, 17] to model Ge_2Se_3 and present preliminary calculations on the perfect cell. The crystalline model discussion includes past experimental and theoretical

results on short-range order and chemical order of Ge_2Se_3 (3.1.1) and characterization of the crystalline model (3.1.2). The chapter concludes with physical description of the crystalline model (3.2.1) and convergence studies for the $\boldsymbol{k}$-point sampling mesh (3.2.2) and real space sampling grid (3.2.3).

In Chapter 4, we present results on oxygen defects. Section 4.1 covers the approach (4.1.1) and analytical interpretation (4.1.2, 4.1.3 and 4.1.4) utilized in the studies in this thesis. Our analysis used statistical thermodynamics and kinetics with the operational temperature provided by K. Campbell to interpret the results. Section 4.2 begins our oxygen defect result presentation. The atomic oxygen defect convergence study (4.2.1) determined the 80-atom unit cell is sufficient for the majority of our calculations. In the next two subsections, we report a preference for low spin intralayer atomic oxygen defect configurations in Ge_2Se_3 (4.2.2 and 4.2.3). Section 4.3 discusses the effects of intralayer atomic oxygen defects on Ge_2Se_3. We found that atomic oxygen energetically prefers to form defects in the intralayer environment and specifically to occupy germanium dimers[13] (4.3.1). Electrical properties of Ge_2Se_3 do not change significantly in the presence of atomic oxygen defects (4.3.2 and 4.3.3).

In Chapter 5, we present results on silver defects and silver/oxygen interactions. The chapter begins with past theoretical work by Edwards *et al.* on silver defects and self-trapped electrons (5.1.1). The next subsection begins our silver defect result presentation. The silver defect convergence study determined the 80-atom unit cell is sufficient for the majority of our calculations (5.1.2). The results of these repeated silver defect calculations agree well with Edwards' results (5.1.3 and 5.1.4). Section 5.2 addresses interactions of intralayer atomic oxygen defects with silver defects in Ge_2Se_3. Electrical properties of Ge_2Se_3 with absorbed silver again do not change significantly in the presence of atomic oxygen defects (5.2.1 and 5.2.2). Localized states of silver defect configurations are preserved after incorporating atomic oxygen

[13] atomic oxygen occupies germanium dimers by bridging the dimers. That is by Ge-O-Ge.

(5.2.2). As mentioned, silver occupation of germanium dimers[14] is thought to be crucial to device operation, and oxygen tends to occupy germanium dimers. We show that germanium dimer occupation operates on a first-come-first-serve basis; i.e. the Ge-O-Ge moities repel silver, and the Ag-Ge moities repel oxygen.

Lastly, in Chapter 6, we summarize the conclusions reached in this thesis and outline relevant future work.

[14]Silver occupies germanium dimers by silver substitution/displacement of a germanium.

Chapter 2: General Background Theory

2.1 Quantum Mechanical Modeling of Defects in Crystals

In performing defect modeling, we must identify the statistically preferred, i.e. lowest energy, defect configurations to know their effects and behavior in a host material. We use energy of formation (ΔE_f),

$$\Delta E_f = E^{(\text{Defect})} - (E^{(\text{Host})} + \sum_i N_i \mu_i). \quad (1)$$

In Eq. 1, $E^{(\text{Defect})}$ is the defect configuration energy. $E^{(\text{Host})}$ is the host crystal[15] configuration energy. N_i is the number of atoms of the i^{th} element added ($N_i > 0$) or subtracted ($N_i < 0$) from the host system to form the defects, and μ_i is the chemical potential of the i^{th} element in its standard state.

To compute ΔE_f, we need chemically accurate energies[16] corresponding to the defect and reference states. In this section, we first briefly review the periodic quantum mechanical method used to atomically model Ge_2Se_3, the host material, and defect configurations.

2.1.1 Born-Oppenheimer Approximation

We begin with the separation of the time-independent Schrödinger equation (Eq. 2) into electronic and nuclear portions with the Born-Oppenheimer Approximation

[15] Host crystals do not have defects.

[16] Chemically accurate energies are accurate enough to calculate barriers and bond energies. This typically mean fractions of an eV; more specifically, this means energies accurate to 0.043 eV.

[19]. Through this approximation, the $N^{(N)}$-nuclei and $N^{(e)}$-electron quantum problem is separated into distinct electronic structure and nuclear structure problems.

$$\mathcal{H}\Psi = \Bigg\{ -\sum_{a}^{N^{(N)}} \frac{\hbar^2}{2m_a^{(N)}}\nabla_a^2 - \sum_{i}^{N^{(e)}} \frac{\hbar^2}{2m^{(e)}}\nabla_i^2 + \sum_{i>j} \frac{e^2}{|\boldsymbol{r}_i - \boldsymbol{r}_j|} - \sum_{i,a} \frac{Z_a e^2}{|\boldsymbol{r}_i - \boldsymbol{R}_a|} + \sum_{a>b} \frac{Z_a Z_b e^2}{|\boldsymbol{R}_a - \boldsymbol{R}_b|} \Bigg\} \Psi = E\Psi \tag{2}$$

Here, $\mathcal{H}$ is the total Hamiltonian operator, Ψ is the total wave function and E is the total energy of the complete system. The first term is the nuclear kinetic energy operator with the index, a, labeling each nucleus. The second term is the electronic kinetic energy operator with the index i labeling the electrons. The third term is the electronic-electronic potential energy operator with indices i and j labeling each electron. The fourth term is the electronic-nuclear potential energy operator. The fifth term is the nuclear-nuclear potential energy operator, with indices a and b labeling the nuclei. $\hbar = \frac{h}{2\pi}$ is the reduced Planck constant. $N^{(N)}$ and $N^{(e)}$ are the total number of nuclei and electrons, respectively. $m_a^{(N)}$ and $m^{(e)}$ are the masses of nuclei, a, and electrons, respectively. e is the elementary electron charge, and Z_a is the nuclear charge of the a^{th} nucleus.

In an ordinary solid state system, the nuclear and electronic motions operate on very different timescales due to the great mass difference between electrons and nuclei. Born and Oppenheimer showed using a perturbative approach that the time-independent Schrödinger equation is approximately separable; that is, for the l^{th} electronic energy level, we have,

$$\Psi_l(\{\boldsymbol{r}_i\}, \{\boldsymbol{R}_a\}) \approx \chi_l(\{\boldsymbol{R}_a\})\psi_l(\{\boldsymbol{r}_i\}; \{\boldsymbol{R}_a\}). \tag{3}$$

Here, χ_l is the nuclear wave function with $\{\boldsymbol{R}_a\}$ as the nuclear coordinates, and ψ_l is the electronic wave function with $\{\boldsymbol{r}_i\}$ as the electronic coordinates. Note that $\psi_l(\{\boldsymbol{r}_i\};\{\boldsymbol{R}_a\})$ depends explicitly on $\{\boldsymbol{r}_i\}$ and parametrically on $\{\boldsymbol{R}_a\}$, and $\chi_l(\{\boldsymbol{R}_a\})$ only depends on $\{\boldsymbol{R}_a\}$. After substituting Eq. 3 into Eq. 2, one obtains two equations, the electronic and nuclear Schrödinger equations. ψ_l can be determined through the electronic Schrödinger equation for fixed $\{\boldsymbol{R}_a\}$,

$$\mathcal{H}^{(e)}\psi_l = \Bigg\{ -\sum_i^{N^{(e)}} \frac{\hbar^2}{2m^{(e)}}\nabla_i^2 + \sum_{i>j} \frac{e^2}{|\boldsymbol{r}_i - \boldsymbol{r}_j|} - \sum_{i,a} \frac{Z_a e^2}{|\boldsymbol{r}_i - \boldsymbol{R}_a|} + \sum_{a>b} \frac{Z_a Z_b e^2}{|\boldsymbol{R}_a - \boldsymbol{R}_b|} \Bigg\} \psi_l = E_l^{(e)}(\{\boldsymbol{R}_a\})\psi_l. \tag{4}$$

Here, $\mathcal{H}^{(e)}$ is the electronic Hamiltonian operator. $E_l^{(e)}$ is the electronic energy. Since $\{\boldsymbol{R}_a\}$ are fixed while solving for $E_l^{(e)}(\{\boldsymbol{R}_a\})$ and $E_l^{(e)}$ does not depend on $\{\boldsymbol{r}_i\}$, the nuclear-nuclear potential energy term is a constant and can be removed from the equation and added on at the end of the calculation. $E_l^{(e)}(\{\boldsymbol{R}_a\})$ acts as the potential energy operator in the nuclear Schrödinger equation (Eq. 5). Solving the nuclear structure problem requires first solving the electronic structure problem, Eq. 4.

$$\left(-\sum_a^{N^{(N)}} \frac{\hbar^2}{2m_a^{(N)}}\nabla_a^2 + E_l^{(e)}(\{\boldsymbol{R}_a\}) \right) \chi_l = E\chi_l \tag{5}$$

2.1.2 Density Functional Theory

There are two popular families of methods to solve the electronic structure problem, Eq. 4, wave function (WF)-based methods, constituted by Hartree-Fock theory and its extensions, and density functional theory-based methods [20]. The former is formulated around the electronic wave function, $\psi_l(\{\boldsymbol{r}_i\})$, and the corresponding single-electron wave functions, $\psi_{l,i}(\boldsymbol{r}_i)$; the latter is formulated around the electron

density, $\rho(\boldsymbol{r})$. Modern applications of WF and DFT methods expand $\psi_{l,i}(\boldsymbol{r}_i)$ in a known basis set [21], such as plane waves [22, 23, 24, 25] and linear combinations of atomic orbitals (LCAO) [26].

Due to its historical impact and the physical insights it provides about its extensions – such as second and fourth order Møller-Plesset Perturbation Theories (MP2) [27] (MP4) [28] and configuration interaction [29, 30] – and DFT, a brief discussion of Hartree-Fock theory is warranted. This theory begins with a trial wave function in the form of a Slater determinant constructed from single-electron wave functions, $\psi_i(\boldsymbol{r})$ [31, 32, 33]. Eq. 4 becomes

$$\begin{aligned}\Bigg\{\Bigg(-\frac{\hbar^2}{2m^{(e)}}\nabla_1^2-\sum_a\frac{Z_ae^2}{|\boldsymbol{r}_1-\boldsymbol{R}_a|}\Bigg)\\ +\Bigg(\sum_{j\neq i}\int e^2\frac{|\psi_j(\boldsymbol{r}_2)|^2}{|\boldsymbol{r}_1-\boldsymbol{r}_2|}\,d\boldsymbol{r}_2\Bigg)\Bigg\}\psi_i(\boldsymbol{r}_1)\\ -\Bigg(\sum_{j\neq i}\int e^2\frac{\psi_j^*(\boldsymbol{r}_2)\psi_i(\boldsymbol{r}_2)}{|\boldsymbol{r}_1-\boldsymbol{r}_2|}\,d\boldsymbol{r}_2\psi_j(\boldsymbol{r}_1)\Bigg)=\epsilon_i\psi_i(\boldsymbol{r}_1),\\ i=1,\,2,\,3...N^{(e)}.\end{aligned}\tag{6}$$

These are the famous Hartree-Fock equations. The first two terms constitute the single-electron Hamiltonian operator, $\mathcal{H}_1^{(e)}$. The third term is the Coulomb potential operator as it corresponds to the classical electrostatic repulsion of the i^{th} electron with the remaining electrons. The exchange operator is defined as $\mathcal{K}_j\psi_i(\boldsymbol{r}_1)=\int e^2\frac{\psi_j^*(\boldsymbol{r}_2)\psi_i(\boldsymbol{r}_2)}{|\boldsymbol{r}_1-\boldsymbol{r}_2|}d\boldsymbol{r}_2\psi_j(\boldsymbol{r}_1)$. ϵ_i is the orbital energy for the i^{th} electron. The single Slater determinant ansatz allows $\psi_i(\boldsymbol{r})$ to have some but not enough quantum interaction, specifically exact exchange but no explicit correlation,[17] consequently Hartree-Fock does not provide sufficient overall chemical accuracy for computing atomization ener-

[17] We define quantum interaction, exchange and correlation, below. In short, quantum interaction is all energy not captured by the non-interacting kinetic energy and classical electrostatic energy.

Table 1: Atomization energies deviation of DFT versus Hartree-Fock and extensions. Deviation (kcal/mol) from experiment of DFT methods and WF methods 6-31G* atomization energies, for 32 neutral molecular systems. Taken from Table I of Ref. [35].

	DFT		WF	
	B-VWN	B-LYP	Hartree-Fock	MP2
Mean deviation	0.1	1.0	-85.8	-22.4
Mean absolute deviation	4.4	5.6	85.9	22.4

gies. But Hartree-Fock's extensions, through systematic improvements, can achieve greater chemical accuracy at the expense of greater computational effort [34, 35].

By contrast, DFT has better chemical accuracy and scaling with problem size than Hartree-Fock [35]. Table 1 shows the deviation from experiment of DFT methods and WF methods taken from an early paper comparing the two. The exchange functional for DFT was the Becke (B) functional [36], a generalized gradient approximation (GGA) exchange functional. The two correlation functionals for DFT were the Vosko, Wilk, and Nusair (VWN) parameterization [37], related to the local spin density approximation (LDSA) functional [38], and the Lee, Yang, and Parr (LYP) functional based on the Colle-Salvetti functional [39]. DFT, with a density-gradient corrected exchange, outperformed Hartree-Fock and MP2 in atomization energy chemical accuracy. Table 2 shows the formal scaling with problem size for WF methods versus DFT methods and modern applications of Hartree-Fock theory versus DFT in large systems. Researchers have used Hartree-Fock [40] and MP2 [41] of the WF family to model solids. In large systems, even modern, efficient implementations of Hartree-Fock, such as that in GAMESS [42], have worse problem size scaling than DFT in SeqQuest [43, 44].[18] While MP2 has acceptable chemical accuracy, its unfavorable scaling with problem size frequently limits the problem size that can be studied [35].

[18]SeqQuest scales O(N-N$^{1.5}$) with the problem size for calculations with less than 500 atoms [43]. This is the quantum electronic structure code we used.

Table 2: Atomic orbital basis function scaling for several methods. The formal atomic orbital basis function scaling of several methods and of modern applications in large systems with efficient implementations.

	Formal Scaling			
Method	HF [35]	MP2 [35]	MP4 [35]	DFT [35]
Scaling Order	$O(N^4)$	$O(N^5)$	$O(N^7)$	$O(N^3)$
	Modern Application in Large Systems			
Code	(GAMESS) (HF) [42]		SeqQuest (DFT) [43, 44]	
Scaling Order	$O(N^3)$		$O(N^{1\text{-}1.5})$	

Historically, researchers have used density-based methods as opposed to Hartree-Fock to model electronic structure in condensed matter due to the favorable scaling. One such method is the Thomas-Fermi model [45, 46, 47], and another is Slater's Xα method [48], which used self-consistent field (SCF) iteration with a density-based exchange-correlation functional. We should note that Slater first intended the Xα method as just a simplification of Hartree-Fock that used a density functional exchange energy functional to replace the exchange operator term [49]. In 1964, Hohenberg and Kohn formalized the density-based methods with the two Hohenberg-Kohn theorems of ground state DFT [50]. In 1965, Kohn and Sham made DFT practical with the Kohn-Sham method [38].

The two Hohenberg-Kohn theorems provide the formal theoretical basis for DFT. The first Hohenberg-Kohn theorem states, "the external potential $v(\boldsymbol{r})$[19] is determined, within a trivial additive constant, by the electron density $\rho(\boldsymbol{r})$ [51]." Since $v(\boldsymbol{r})$ uniquely determines the ground state energy (E_{gs}), ρ_{gs} uniquely determines E_{gs} [51].

The second Hohenberg-Kohn theorem is an energy variational principle for $\rho(\boldsymbol{r})$. Consider Eq. 4 for the ground state, we denote the electronic kinetic energy as $T[\rho] = \langle\psi| - \sum_i^{N^{(e)}} \frac{\hbar^2}{2m^{(e)}} \nabla_i^2 |\psi\rangle$, the electronic-electronic potential energy as $V^{(ee)}[\rho] =$

[19] In this thesis, the electronic-nuclear or external potential is notated as $V^{(Ne)}(\boldsymbol{r}) = -\sum_{i,a} \frac{Z_a e^2}{|\boldsymbol{r}_i - \boldsymbol{R}_a|}$.

$\langle\psi|\sum_{i>j}\frac{e^2}{|\boldsymbol{r}_i-\boldsymbol{r}_j|}|\psi\rangle$ and the electronic-nuclear potential energy as $V^{(Ne)}[\rho] = \langle\psi| - \sum_{i,a}\frac{Z_a e^2}{|\boldsymbol{r}_i-\boldsymbol{R}_a|}|\psi\rangle = -\int\sum_a \frac{Z_a e^2}{|\boldsymbol{r}-\boldsymbol{R}_a|}\rho(\boldsymbol{r})\,d\boldsymbol{r}$. Hohenberg and Kohn showed that there exists a universal functional valid for any external potential, $F_{HK}[\rho] = T[\rho] + V^{(ee)}[\rho]$, so the energy is then defined as $E[\rho] = F_{HK}[\rho] + V^{(Ne)}[\rho]$ [50]. For any particular $V^{(Ne)}[\rho]$, the E_{gs} of the system is the global minimum value of this functional, and the $\rho(\boldsymbol{r})$ that minimizes $E[\rho]$ is ρ_{gs} [52]. The electronic structure problem thus can be framed as the minimization of the total electronic energy with respect to the total electron density:

$$\begin{aligned} E_{gs} = E[\rho_{gs}] &= \min_{\rho}(E[\rho]) \\ &= \min_{\rho}\left(T[\rho] + V^{(ee)}[\rho] - \int\sum_a \frac{Z_a e^2}{|\boldsymbol{r}-\boldsymbol{R}_a|}\rho(\boldsymbol{r})\,d\boldsymbol{r}\right) \\ &\qquad + \sum_{a>b}\frac{Z_a Z_b e^2}{|\boldsymbol{R}_a - \boldsymbol{R}_b|}. \end{aligned} \tag{7}$$

As mentioned, $T[\rho]$ is the kinetic energy functional, and $V^{(ee)}[\rho]$ is the electronic-electronic potential energy functional.

Due to the difficulties of explicitly expressing $T[\rho]$ and coincidentally the importance of the single-electron wave functions in the analysis of solid state systems, Kohn and Sham turned to an approach that utilizes single-electron "wave functions"[20] as intermediate functions of $\rho(\boldsymbol{r})$, framed similarly to the Xα method [38, 48]. We start by rewriting two terms, the kinetic energy functional, $T[\rho]$, and the electron-electron interaction energy functional, $V^{(ee)}[\rho]$, as

$$T[\rho] = -\frac{\hbar^2}{2m^{(e)}}\sum_i^{N^{(e)}}\int\phi_i(\boldsymbol{r}_i)\nabla_i^2(\phi_i(\boldsymbol{r}_i))\,d\boldsymbol{r}_i + \Delta T[\rho] \tag{8}$$

[20]The physicality of the Kohn-Sham eigenfunctions is beyond the scope of this thesis.

$$V^{(ee)}[\rho] = \frac{e^2}{2}\int\int \frac{\rho(\boldsymbol{r})\rho(\boldsymbol{r}')}{|\boldsymbol{r}-\boldsymbol{r}'|}\,d\boldsymbol{r}\,d\boldsymbol{r}' + \Delta V^{(ee)}[\rho] \tag{9}$$

The first term of Eq. 8 is the kinetic energy functional of a fictitious Kohn-Sham system of noninteracting electrons with the $\{\phi_i(\boldsymbol{r})\}$ as the Kohn-Sham single-electron wave functions, conventionally known as the Kohn-Sham orbitals. Due to the noninteraction of the electrons, Φ, the Kohn-Sham system's total electronic wave function, is exactly a Slater determinant of the $\{\phi_i(\boldsymbol{r})\}$. The first term of Eq. 9 is the classical electrostatic energy functional.[21] $\Delta T[\rho]$ and $\Delta V^{(ee)}[\rho]$ are remaining terms that account for portions of the corresponding energies missed by rewriting $T[\rho]$ and $V^{(ee)}[\rho]$.

Kohn and Sham showed that the $\{\phi_i(\boldsymbol{r})\}$ can be obtained by solving the coupled set of Kohn-Sham single-electron equations,

$$\left\{\frac{-\hbar^2}{2m^{(e)}}\nabla^2 + e^2\int\frac{\rho(\boldsymbol{r}')}{|\boldsymbol{r}-\boldsymbol{r}'|}\,d\boldsymbol{r}' - \sum_a \frac{Z_a e^2}{|\boldsymbol{r}-\boldsymbol{R}_a|} + \frac{\delta E^{(XC)}[\rho]}{\delta\rho}\right\}\phi_i(\boldsymbol{r}) = e_i^{(mod)}\phi_i(\boldsymbol{r}) \tag{10}$$

$$i = 1,\ 2,\ 3 \ldots N^{(e)}$$

Here, $e^2\int\frac{\rho(\boldsymbol{r}')}{|\boldsymbol{r}-\boldsymbol{r}'|}\,d\boldsymbol{r}'$ is the classical electrostatic repulsion potential, and $-\sum_a \frac{Z_a e^2}{|\boldsymbol{r}-\boldsymbol{R}_a|}$ is the complete nuclear attraction on a single electron. The functional derivative of the exchange-correlation energy, $\frac{\delta E^{(XC)}[\rho]}{\delta\rho} = V^{(XC)}[\rho]$, is known as the exchange-correlation potential, where $E^{(XC)}[\rho] = \Delta T[\rho] + \Delta V^{(ee)}[\rho]$. $e_i^{(mod)}$ are the eigenvalues of the Kohn-Sham orbitals. Note that $e_i^{(mod)}$ are different from the real orbital energies due to the *modified* external potential used in the Kohn-Sham equations.

Notice the similarities between the Kohn-Sham equations and the Hartree-Fock

[21] The classical electrostatic energy is also known as Hartree energy.

equations. $-\frac{\hbar^2}{2m^{(e)}}\nabla^2 - \sum_a \frac{Z_a e^2}{|\boldsymbol{r}-\boldsymbol{R}_a|} = \mathcal{H}_1^{(e)}$ is the same as the corresponding terms in the Hartree-Fock equations; $e^2 \int \frac{\rho(\boldsymbol{r}')}{|\boldsymbol{r}-\boldsymbol{r}'|}\, d\boldsymbol{r}'$ of Eq. 10 closely resembles $\sum_{j\neq i} \int e^2 \frac{|\psi_j(\boldsymbol{r}_2)|^2}{|\boldsymbol{r}_1-\boldsymbol{r}_2|}\, d\boldsymbol{r}_2$ of Eq. 6.[22] Intuitively, the remaining term, $\frac{\delta E^{(XC)}[\rho]}{\delta[\rho]}$, must relate to exchange and correlation.

Once the $\{\phi_i\}$ have been found by solving Eqs. 10 with a given input $\rho(\boldsymbol{r})$, an updated output $\rho(\boldsymbol{r})$ can be obtained from the $\{\phi_i\}$ via

$$\rho(\boldsymbol{r}) = \sum_i^{N^{(e)}} |\phi_i|^2. \tag{11}$$

Eqs. 10 and Eq. 11 must be solved self-consistently. A trial density, ρ_{input}, is input into the Kohn-Sham equations to solve for the $\{\phi_i\}$. The $\{\phi_i\}$ are used to compute a new density, ρ_{output}. If ρ_{input} and ρ_{output} do not agree to within a small tolerance, we input ρ_{output} into the Kohn-Sham equations, and the iteration repeats until $\rho_{input} \approx \rho_{output}$. This ρ_{output} is ρ_{gs}. ρ_{gs} and the corresponding consistent $\{\phi_i\}$ are input into $E[\rho]$ to obtain E_{gs}, given in Eq. 12,

$$\begin{aligned} E_{gs} = &-\frac{\hbar^2}{2m^{(e)}} \sum_i^{N^{(e)}} \int \phi_i(\boldsymbol{r}_i) \nabla_i^2 (\phi_i(\boldsymbol{r}_i))\, d\boldsymbol{r}_i \\ &+ \frac{e^2}{2} \int\int \frac{\rho_{gs}(\boldsymbol{r})\rho_{gs}(\boldsymbol{r}')}{|\boldsymbol{r}-\boldsymbol{r}'|}\, d\boldsymbol{r}\, d\boldsymbol{r}' \\ &- \sum_a \int \frac{Z_a e^2}{|\boldsymbol{r}-\boldsymbol{R}_a|} \rho_{gs}\, d\boldsymbol{r} + E^{(XC)}[\rho_{gs}] \\ &+ \sum_{a>b} \frac{Z_a Z_b e^2}{|\boldsymbol{R}_a - \boldsymbol{R}_b|}. \end{aligned} \tag{12}$$

The difference between Eq. 7 and Eq. 12 is due to the new expressions of $T[\rho]$ and $V^{(ee)}[\rho]$.

[22] The Kohn-Sham equations also include $j = i$ terms. These self-interaction energy terms must be corrected with $E^{(XC)}[\rho]$.

2.1.3 Geometry Optimization

In Subsection 2.1.2 we reviewed the Kohn-Sham method of DFT. With it, we can compute the electronic ground state energy, E_{gs}, for a given atomic configuration or geometry, $\{\boldsymbol{R}_a\}$. A fully quantum mechanical treatment of the nuclear structure problem (Eq. 5) would require considerable computation. Fortunately, we only require the global energy-minimized geometry, which necessitates local minimization[23] of the overall electronic energy by varying the $\{\boldsymbol{R}_a\}$.

The force on a nucleus a is given by $\boldsymbol{F}_a = -\nabla_{\boldsymbol{R}_a} E_{gs}(\{\boldsymbol{R}_a\})$. We can arrive at a local energy minimum by eliminating the net forces on all nuclei. With a given geometry, $\{\boldsymbol{R}_a\}$, we solve the electronic structure problem to obtain E_{gs} at said $\{\boldsymbol{R}_a\}$, and we then compute $\{\boldsymbol{F}_a\}$. A chosen local root-finding algorithm then attempts[24] to produce a local root of $\{\boldsymbol{F}_a\}$,[25] i.e. a new $\{\boldsymbol{R}_a\}$ where each $\boldsymbol{F}_a = 0$. This new $\{\boldsymbol{R}_a\}$ becomes the new geometry. We then compute E_{gs} and $\{\boldsymbol{F}_a\}$ again with the new geometry. This iterative process, known as geometry relaxation, is repeated until each $\boldsymbol{F}_a \approx 0$ within a small threshold. The resulting atomic configuration is the local energy minimum geometry.

The global energy minimum geometry corresponds to the system's nuclear ground state, which are the statistically preferred equilibrium positions of those nuclei's vibrational motion.[26] We perform sufficient configuration sampling to find a reasonable candidate for the global energy minimum geometry.[27]

[23] The minimization, or search, over the energy surface is performed locally.

[24] The exact operations of these mathematical procedures are not appropriate for this thesis's content.

[25] Each $\boldsymbol{F}_a$ is a function of $\{\boldsymbol{R}_a\}$.

[26] Given a global energy minimum configuration and multiple energy minimum configurations that have similar energies, all of these configurations are relevant. Please refer to Subsection 4.1.3.

[27] We describe this "sufficient configuration sampling" in Subsection 4.1.1.

2.1.4 Periodic Systems

Additional theoretical framework is necessary in order to perform practical calculations for large periodic systems using the theories described above. Two pervasive modeling methods for solids are the cluster approximation and periodic method [53]. The cluster approximation simply models the material using a subsystem, with hydrogen atoms to terminate dangling bonds. The periodic calculation models an infinitely periodic system. Taking advantage of the periodic potential and imposing periodic boundary conditions on the single-electron wave function, we can model macro-scale host crystals without unreasonably increasing the calculation time.

The centerpiece of the periodic approximation, Bloch's Theorem, is a consequence of the periodic boundary condition and periodic potential [53, 54]. The periodic potential causes the single-electron Schrödinger equation to have translational symmetry. Single-electron Schrödinger-like equations with translational symmetry have solutions of the form of:

$$\psi_{i,\boldsymbol{k}}(\boldsymbol{r}+\boldsymbol{R}) = e^{i\boldsymbol{k}\cdot\boldsymbol{R}}\psi_{i,\boldsymbol{k}}(\boldsymbol{r}) \tag{13}$$

$$\psi_{i,\boldsymbol{k}}(\boldsymbol{r}) = e^{i\boldsymbol{k}\cdot\boldsymbol{r}}u_{i,\boldsymbol{k}}(\boldsymbol{r}) \tag{14}$$

$\psi_{i,\boldsymbol{k}}(\boldsymbol{r})$, known as a Bloch function, is the single-electron wave function associated with a specific wave vector $\boldsymbol{k}$. For each $\boldsymbol{k}$, an electron occupies a single-electron level, i,[28] based on the Aufbau principle. $\boldsymbol{R}$ is a Bravais lattice vector. Whenever a Bloch function is translated by $\boldsymbol{R}$, it is merely multiplied by a phase factor, $e^{i\boldsymbol{k}\cdot\boldsymbol{R}}$. In Eq. 14, $u_{i,\boldsymbol{k}}(\boldsymbol{r})$ has the same periodicity as the Bravais lattice, which consists of the set of all possible $\boldsymbol{R}$,

[28]For a temperature of 0 K, the $N^{(e)}$ electrons would occupy up to $\frac{N^{(e)}}{2}$ levels rounded up, of course starting from lowest energy levels first until all electrons are accounted for.

$$\boldsymbol{R} = n_1\boldsymbol{a}_1 + n_2\boldsymbol{a}_2 + n_3\boldsymbol{a}_3. \tag{15}$$

Here, $\boldsymbol{a}_1$, $\boldsymbol{a}_2$, and $\boldsymbol{a}_3$ are three primitive lattice vectors,[29] and n_1, n_2, and n_3 are integers ranging from 0 to N_1, N_2 and N_3 respectively. $N = N_1N_2N_3$ is the total number of unit cells in the periodic system.

Lastly, the periodic boundary condition leads to the quantization of $\boldsymbol{k}$.[30] There are only a finite number of unique $\psi_{i,\boldsymbol{k}}$ from the infinite number of possible $\boldsymbol{k}$ that satisfy these boundary conditions. It can be shown that the actual single-electron wave functions, $\psi_i(\boldsymbol{r})$, can be represented as the sum of all unique Bloch functions [55],

$$\psi_i(\boldsymbol{r}) = \sum_{\boldsymbol{k}\in\{\boldsymbol{k}_{FBZ}\}} \psi_{i,\boldsymbol{k}}(\boldsymbol{r}) \tag{16}$$

Conventionally, the set of all unique Bloch functions are chosen to correspond to $\boldsymbol{k} \in \{\boldsymbol{k}_{FBZ}\}$, the wave vectors in the first Brillouin zone.

So far the above-described periodic machinery have been framed to be used with WF theory, but we can also use this machinery with DFT. We input the explicit expression of $\psi_{i,\boldsymbol{k}}$ and Eq. 16 into Eq. 11. With the Kohn-Sham SCF iteration, we can in principle compute ρ_{gs} by performing a summation over $\{\boldsymbol{k}_{FBZ}\}$ and determine E_{gs} for a given $\{\boldsymbol{R}_a\}$ of a unit cell inside the infinitely large host crystal. The problem is the large size of $\{\boldsymbol{k}_{FBZ}\}$.[31]

The $\{\boldsymbol{k}_{FBZ}\}$ summation can be replaced with an integral, but even the $\{\boldsymbol{k}_{FBZ}\}$ integration of a fitted $\psi_i(\boldsymbol{k})$ would require unreasonable computational time/resources. Fortunately, Monkhorst and Pack [56] showed that this integral can be replaced by a limited weighted summation over certain equally spaced members of $\{\boldsymbol{k}_{FBZ}\}$, which

[29] Physically, they are the three unique edges of the parallelepiped primitive unit cell.

[30] Periodic boundary conditions imply $e^{i\boldsymbol{k}\cdot\boldsymbol{R}_{max}} = 1$, where $\boldsymbol{R}_{max}$ is the extent of the Bravais lattice. This evidently leads to the quantization of $\boldsymbol{k}$.

[31] The number of $\boldsymbol{k} \in \{\boldsymbol{k}_{FBZ}\}$ is $N = N_1N_2N_3$, with N_1, N_2 and N_3 each approaching infinity.

are known as the $\boldsymbol{k}$-point mesh.

On a side note, the explicit expression of $u_{\boldsymbol{k}}(\boldsymbol{r})$ is basis-dependent [55]. Using LCAO expansion, $\psi_{i,\boldsymbol{k}}(\boldsymbol{r})$ and $u_{i,\boldsymbol{k}}(\boldsymbol{r})$ take the following forms [57],

$$\psi_{i,\boldsymbol{k}}(\boldsymbol{r}) = \sum_m c_m(\boldsymbol{k}) \sum_{\boldsymbol{R}} e^{i\boldsymbol{k}\cdot\boldsymbol{R}} \theta_{m,\boldsymbol{k}}(\boldsymbol{r} - (\boldsymbol{R} + \boldsymbol{R}_m)) \tag{17}$$

$$u_{i,\boldsymbol{k}}(\boldsymbol{r}) = \sum_m c_m(\boldsymbol{k}) \sum_{\boldsymbol{R}} e^{i\boldsymbol{k}\cdot(\boldsymbol{R}-\boldsymbol{r})} \theta_{m,\boldsymbol{k}}(\boldsymbol{r} - (\boldsymbol{R} + \boldsymbol{R}_m)) \tag{18}$$

Here, $\theta_{j,\boldsymbol{k}}(\boldsymbol{r} - \boldsymbol{R} - \boldsymbol{R}_a)$ is a j type atomic orbital for atom a and centered at its location, $\boldsymbol{R}_a$, and $(\boldsymbol{R} + \boldsymbol{R}_a)$ are equivalent locations throughout the Bravais lattice. The index, m, is shorthand for the three indices, the atomic orbital type, j, atom number, a, and element of atom a. $c_m(\boldsymbol{k})$ is the weight of each orbital. The expression of $u_{i,\boldsymbol{k}}(\boldsymbol{r})$ in Eq. 18 has manifestly the same periodicity as the Bravais lattice, which is of course indicative that this $\psi_{i,\boldsymbol{k}}(\boldsymbol{r})$ is a Bloch function.

2.1.5 Pseudopotentials

With the combined machinery of the Kohn-Sham method, geometry relaxation, and the periodic method, we can perform host crystal calculations and obtain local energy-minimum geometry configurations, but this procedure is still excessively time-consuming. To reduce the computational size of the problem, we take advantage of the fact that the tightly bound core electrons do not participate in chemical bonding. The pseudopotential approximation replaces the Coulombic potential of the nucleus and core electrons with an effective ionic potential, so we only need to solve for the valence electrons [58].

Proper execution of the pseudopotential approximation makes calculations more tractable, while still accurate [58]. The reduction of the number of electrons solved is very often over 50%. For example, consider Ge_2Se_3. Germanium has 4 valence elec-

trons and 32 total electrons. Selenium has 6 valence electrons and 34 total electrons. Per stoichiometric Ge_2Se_3 unit, 140 out of 166 electrons can be removed.

2.1.6 Defect Modeling and Supercell Approximation

So far, our discussion only pertain to host crystals; the machinery rigorously models defect-free crystalline environments. With typical neutral defect concentrations being $1:10^5$ to $1:10^7$, they are isolated from one another. To extend our theoretical machinery to this situation, we use the supercell approximation [59] to model neutral isolated defects.

The supercell is a finite periodic replication of the primitive unit cell. We introduce one or more point defect into the supercell and use the defected supercell as the unit cell in the combined theoretical machinery described so far. In principle, we can use the supercell approximation to study arbitrary defect concentrations. However, typical concentrations cannot be achieved in practice. Fortunately, neutral defect energies quickly approach the infinite dilution value as cell size increases. To determine the minimally sufficient cell size, we have performed convergence studies involving equivalent defect configurations of varying unit cell sizes.

2.1.7 Calculation Details

Using the the supercell approximation, we performed host crystal and neutral defect calculations to obtain local energy-minimum geometries (relaxed geometries), their respective energies and Kohn-Sham orbitals. Our defect studies pick a number of representative starting geometries to implement the prescribed theoretical machinery to sufficiently sample the variational space of that defect configurations in the host crystal. We now summarize the calculation details used in our defect studies. We performed all calculations with SeqQUEST [44], an LCAO, pseudopotential, DFT electronic structure code. The exchange-correlation functional used was the spin-

polarized Perdew-Burke-Ernzerhof (PBE) exchange-correlation functional [60]. We used the Hamann pseudopotential [61] for germanium, selenium and silver atoms, and the Troullier/Martins pseudopotential [62] for oxygen atoms. We represented the atomic orbitals with double-zeta basis functions including polarization functions [63].

The PBE exchange-correlation functional is one of several GGA functionals [60]. To extend the LSDA and incorporate the inhomogeneity of the electron density, GGA adds $\nabla\rho$ dependence to $E^{(XC)}[\rho]$ [60]. Hamann and Troullier/Martins pseudopotentials are both norm-conserving pseudopotentials [64]. The double-zeta basis uses contracted Gaussian functions to represent two Slater type orbitals [63], which are then used to represent a Kohn-Sham orbital. Polarization functions add the flexibility needed to capture bonding behavior [63].

SeqQUEST uses two kinds of grids, a real space sampling grid and a $\boldsymbol{k}$-space grid, also known as $\boldsymbol{k}$-point mesh [44]. The orbitals in an LCAO basis set are generally not orthogonal to each other, so evaluation of overlap integrals is necessary. The real space sampling grid controls how finely they are numerically evaluated. In Subsection 2.1.4, we mentioned that finite sums of Monkhorst-Pack $\boldsymbol{k}$-points are used to compute $\rho(\boldsymbol{r})$; the $\boldsymbol{k}$-point mesh determines the number of Monkhorst-Pack $\boldsymbol{k}$-points included. To determine the minimally sufficient dimensions of real space grid and $\boldsymbol{k}$-point mesh used, we conducted convergence studies, which involves performing host crystal calculations and varying real space grid and $\boldsymbol{k}$-point mesh dimensions.

2.1.8 Nudged Elastic Band Method

As part of our studies, we need to determine barrier heights[32] to escape a given defect configuration and transition to another defect configuration. Using barrier heights and kinetic theory,[33] we can determine the time for the given defect con-

[32]Barrier heights are also known as activation energies.
[33]Refer to Subsection 4.1.3 for relevant details regarding kinetics.

figuration to transition to another. The nudged elastic band (NEB) method is a technique to determine the barrier height between two states, the two given defect configurations, by finding the local minimum energy path [65].

The NEB method involves performing several image calculations (Images 1 through N) connected sequentially by fictitious computational springs; the two ends of this sequence are the two given defect configurations [65].[34] We input specific image geometries, so the sequential gradual geometric variation from the first defect configuration to Images 1 through N to the second defect configuration "morphs" one defect configuration to the other; regarding energy surfaces, the images map out a transition path between the two defect configurations that crosses over the energy barrier in question. The fictitious computational springs constrain the geometry relaxations of the images to result in the local minimum energy path.

After completing the NEB calculation, the transition state is the image with the highest energy. Using the two unchanged defect configurations and the transition state geometry, the energy difference between the first defect and the transition state is the barrier height to access the second defect configuration from the first; the energy difference between the second defect and the transition state is the barrier height to access the first defect configuration from the second.

2.1.9 Projected Density of States

For every wave number, $\boldsymbol{k}$, each electron has its own set of single-electron states. The density of states is the binning of energies of all single-electron states of the solid to show the number of states within each energy interval [66].[35] In principle, the density of states should be based on all sets of single-electron states from all $\boldsymbol{k}$ in

[34] For example, for an NEB calculation with three images, the first defect configuration (D1 or I0, Image 0) is connected to Image 1 (I1), Image 1 is connected to Image 2 (I2), Image 2 is connected to Image 3 (I3), and Image 3 is connected to the second defect configuration (D2 or I4, or Image 4). D1-I1-I2-I3-D2.

[35] The energy of each single-electron state would fall within an energy interval and count as one for that energy interval.

$\{\boldsymbol{k}_{FBZ}\}$. In practice, only the single-electron states of Monkhorst-Pack $\boldsymbol{k}$-points are used. Increasing number of $\boldsymbol{k}$ does not change important band structure features, such as band edges, band gap and gap state.

Note that the single-electron states used in this thesis are the Kohn-Sham eigenstates, not the real single-electron states. Also, calculations done with pseudopotentials do not include the core electron states in the density of states. Fortunately, they do not determine the band structure features mentioned, because the core electron energies are too low and not remotely close to the band gap. While the density of states shows changes to the band structure features of the supercell, we require each atom's projected density of states to study electron localization.

Projected density of states of an atom is the binning of energies of all single-electron states of that atom. Population analysis methods determine the percentage of a single-electron state or Kohn-Sham eigenstate "belonging" to each atom.[36] In the studies of this thesis, we used Mulliken population analysis [67], which provides a reasonable representation of ionicity.

[36]For a projected density of states of an atom, the energy of a single-electron state still falls within an energy interval but count as the atom-assigned percentage. If an electron "belongs" to a specific atom, the atom-assigned percentage would be high. Of course, the sum of all percentages of a single-electron state over all atoms is 100%.

Chapter 3: Crystalline Model of Ge_2Se_3

3.1 Modeling Amorphous Ge_2Se_3

In Chapter 2, we described the supercell approximation for investigating defects in host crystals. However, the Ge_2Se_3 material we are interested in is an amorphous semiconductor, which lacks long range periodicity. Nevertheless, it still possesses short-range order, i.e. the local chemistry of each atom still determines its nearby environment [68, 69]. In past decades, researchers performed theoretical modeling of amorphous semiconductors with crystalline models [70, 71]. With chemically ordered[37] amorphous semiconductors, the short-range order is paramount in their description and modeling. In this section, we motivate the use of a crystalline model for studying amorphous Ge_2Se_3.

3.1.1 Short-Range Order and Chemical Order of Ge_2Se_3

In terms of structural order, amorphous materials are comparable to classical liquids [72]. They lack long-range periodicity but still possess short-range order. Notably, the resistivities of most crystalline solids do not change drastically after melting [73]. This naïvely suggests that the loss of periodicity does not cause significant property changes.

Indeed, it is known that short-range order determines the opto-electronic properties in amorphous semiconductors [73]. For example, the density of states as a function of binding energy of amorphous (a-)Si and crystalline (c-)Si are similar. Calculations have shown that the minor difference is due to the changes in the short

[37] Chemical ordering is defined below.

range order,[38] not the loss of long range periodicity [73]. The topological nature of the network in some semiconductors, perhaps Ge_2Se_3, is more important than the long-range periodicity, because electronic properties depend on the short-range order of these semiconductors.

With these motivations, we focus on the short-range order of Ge_2Se_3. To employ the supercell approximation to model an amorphous compound semiconductor, its short-range atomic configuration must be chemically ordered; i.e. with each element having a strongly preferred coordination number and bonds to specific number of atoms of specific elements [74]. Ge_2Se_3 is ordered this way [75, 76].

Zhou *et al.* [75] report that germanium-selenium glasses are chemically ordered. In Table 1 of Ref. [75], for Ge_2Se_3,[39] germanium on average bonds with 3 ± 0.3 seleniums and 1 ± 0.2 germaniums thus is approximately 4-fold coordinated, and selenium on average bonds with 1.9 ± 0.2 germaniums and thus is approximately 2-fold coordinated.

In the first principles periodic molecular dynamics studies on glassy (g-)Ge_2Se_3, Le Roux *et al.* [76] report that for g-Ge_2Se_3,[40] selenium on average bonds with 0.01 seleniums and 2.14 germaniums, so its average coordination number is 2.15; germanium on average bonds with 3.21 seleniums and 0.52 germaniums, so its average coordination number is 3.73. As seen in Figure 2, for g-Ge_2Se_3, Le Roux *et al.* [76] found that roughly 77% of germanium atoms are 4-fold coordinated and roughly 85% of selenium atoms are 2-fold coordinated. Out of the 77% 4-fold coordinated germanium atoms, 33% (from the 77%) bond with three seleniums and one germanium, and 35% bond with four seleniums [76]. Out of the 85% 2-fold coordinated selenium atoms, 83% (from the 85%) bond with two germaniums [76].

These theoretical results are largely consistent with the experimental results re-

[38] In a-Si, there are odd numbered rings, five-fold and seven-fold, while in c-Si, there are only 6 fold rings [73].

[39] Ge_2Se_3 is notated $Ge_{40}Se_{60}$ in Ref. [75].

[40] In Ref. [76], Le Roux used the term, g-Ge_2Se_3. This is the same as amorphous Ge_2Se_3.

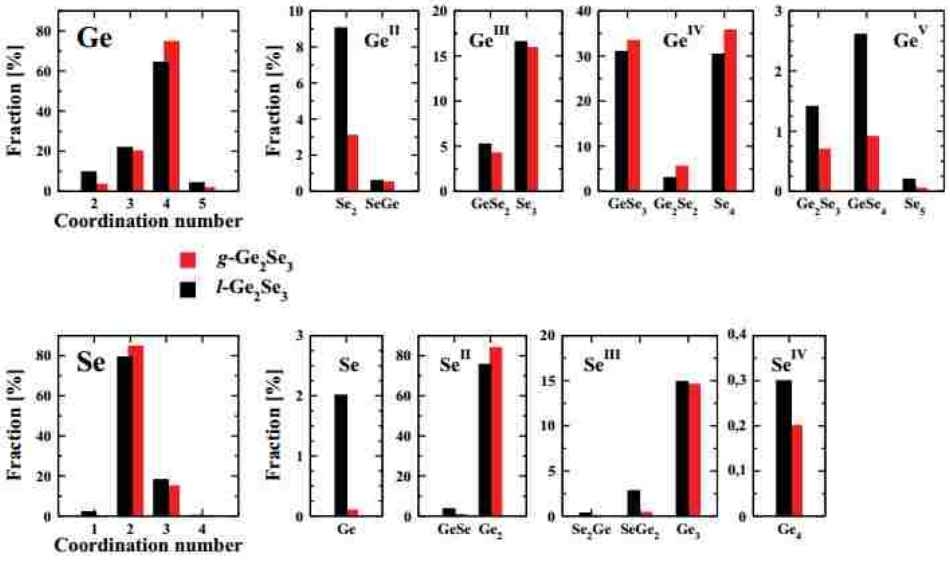

Figure 2: Chemical order details for Ge_2Se_3. This figure was taken from Ref. [76], and the liquid (l)-Ge_2Se_3 data comes from Ref. [77]. Glassy (g)-Ge_2Se_3 and l-Ge_2Se_3 are labeled in red and black, respectively. The coordination numbers of all germanium and selenium atoms in the study was tabulated and presented as fractions. For each element and coordination number, the nearest neighbors are specified.

ported by Zhou *et al.*, but the difference in average bond type of germaniums is significant. For 4-fold coordinated germanium atoms, nearest neighbors of three seleniums and one germanium and nearest neighbors of four seleniums contribute nearly equally. Note that this departure from experimental values may be due to the small sample size of 120 atoms/cell in this study.

3.1.2 Characteristics of Crystalline Model of Ge_2Se_3

In past studies that were the starting point for the present work, Edwards *et al.* used a crystalline model of Ge_2Se_3 (shown in Figure 3) based on Si_2Te_3 to investigate silver defects, self-trapped electrons (STE) and STE caused by silver and tin incorporation [1, 16, 17]. The theoretical level, computational details and practices used

in the studies of this thesis are largely identical to those Edwards *et al.* used.[41]

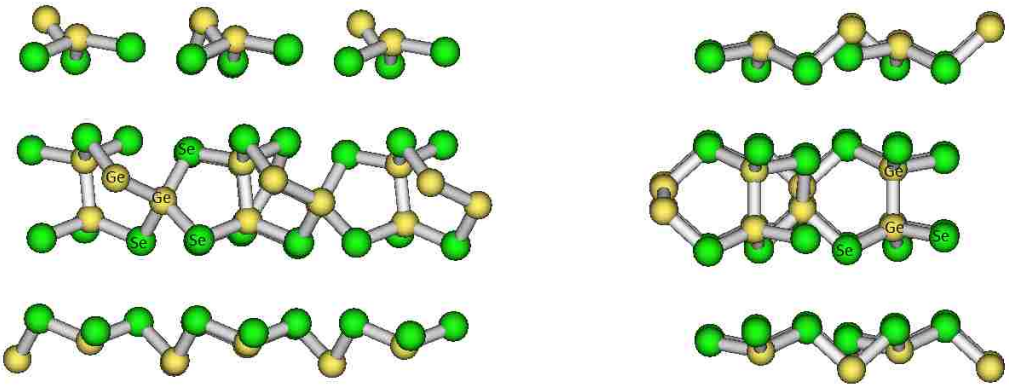

(a) Perspective#1 (b) Perspective#2

Figure 3: Crystalline model of Ge_2Se_3 from 2 perspectives. For all geometry figures, germanium atoms are shown in yellow and selenium atoms in green.

In this crystalline model, each germanium is 4-fold coordinated and bonds with three seleniums and one germanium, and each selenium is 2-fold coordinated and bonds with two germaniums. In Table 3, we compiled characteristic physical and electrical values for Ge_2Se_3, $GeSe_2$ and the crystalline model to make theoretical versus experimental comparisons. The significant difference between experimental and theoretical band gap is expected, because DFT often underestimates the band gap [79]. The experimental versus theoretical bond length and number density differences are minor. The differing stoichiometry likely contributed to the minor bond angle differences. The layered structure of the crystalline model is a significant departure from experimental results. Despite this cell structural difference, the chemically ordered

[41] Aside from a set of cluster calculations using the B3LYP [78] exchange-correlation potential in Ref. [16], we used largely identical methodology details as those Edwards *et al.* used in Refs. [1, 16, 17], and unless specifically stated, they are the same.

crystalline model sufficiently captures the collective short-range order of Ge_2Se_3.

Table 3: Experimental and theoretical characteristics of Ge_2Se_3 and $GeSe_2$.

	Characteristics			
	Band Gap (eV)	Ge-Ge Bond Length (Å)	Ge-Se Bond Length (Å)	Number Density (atoms/Å^3)
Ge_2Se_3 (Experiment)	2.2 [1]	2.41 [75]	2.36 [75]	0.0341 [80]
Crystalline Model (Theory)	0.98 [1]	2.49 for $(\text{Ge-Ge})_{\parallel}$[42] [1], 2.40 for $(\text{Ge-Ge})_{\perp}$[43] [1]	2.41 ± 0.02 [1]	0.0316

	Characteristics	
	Ge-Se-Ge Bond Angle (degrees)	Se-Ge-Se Bond Angle (degrees)
$GeSe_2$ (Experiment)	98 ± 8.2 [75]	113 ± 11 [75]
Crystalline Model (Theory)	99.0 ± 5.6 [1]	110.6 ± 7.5 [1]

3.1.3 Band Gaps of c-$GeSe_2$ and a-$GeSe_2$

We have not directly provided support for the claim that the short-range order of Ge_2Se_3 determines its electrical properties in the last two subsections. We examined the band gaps of c-$GeSe_2$ and a-$GeSe_2$ to make a fair crystalline versus amorphous comparison to argue that long-range periodicity does not contribute significantly to the electrical properties of Ge_2Se_3. Inoue *et al.* [81] reported that the band gaps of c-$GeSe_2$ and a-$GeSe_2$ are respectively 2.6 eV and 2.2 eV. This moderate agreement is consistent with the notion that the short-range order of $GeSe_2$ determines its electrical properties. Furthermore, Inoue *et al.* [81] stated the similarities of photoemission

[42] We define $(\text{Ge-Ge})_{\parallel}$ in Subsection 3.2.1.
[43] We define $(\text{Ge-Ge})_{\perp}$ in Subsection 3.2.1.

spectra[44] of c-$GeSe_2$ and a-$GeSe_2$ is due to their similar short-range order. While a-Ge_2Se_3 and a-$GeSe_2$ have significant structural difference,[45] they are similar enough to lend credence to the notion that the short-range order of Ge_2Se_3 determines its electrical properties, because the relevant electrical properties of c-$GeSe_2$ and a-$GeSe_2$ are similar.

3.2 Preliminary Study Procedures

Environments in and local features of the crystalline model represent locations of interest in Ge_2Se_3. Sufficient sampling of defect configurations involves geometry relaxation of defects placed at locations of interest, so first their identification is crucial. Next, we must perform convergence studies to determine the minimally sufficient real space sampling grid point and $\boldsymbol{k}$-point mesh densities for the crystalline model system; the resulting grid densities ensure calculation precision.[46]

3.2.1 Physical Description and Locations of Interest in Crystalline Model of Ge_2Se_3

The first and second lattice vectors of the 20-atom primitive unit cell are almost the same in length, and the third is approximately twice in length of the first and second. The first lattice vector length is roughly 14.6 a_0, where a_0 is the Bohr radius. For the majority of studies in this thesis, we used an 80-atom unit cell replicated from the primitive unit cell by repeating the cell twice along the first and second lattice vector directions, so that the 80-atom unit cell is roughly cubic. This 20-atom primitive unit cell is the same primitive unit cell Edwards *et al.* used to create the 80-atom unit cell used in Refs. [1, 16, 17]; the 80-atom unit cell is the same as well.

[44] Photoemission spectra are similar to density of states.

[45] a-Ge_2Se_3 have germanium dimers, but a-$GeSe_2$ do not [81].

[46] We use the minimally sufficient grid densities to conserve computational resources while ensuring precision.

As seen in Figure 3, the 80-atom unit cell is layered; extensive empty space separates the identical layers. Within the layers, there are some empty spaces. Due to the chemical ordering of the crystalline model, only germanium dimers and Ge-Se exist in the crystalline model. There are two types of germanium dimers, parallel to layer Ge-Ge, $(\text{Ge-Ge})_{\parallel}$, and perpendicular to layer Ge-Ge, $(\text{Ge-Ge})_{\perp}$. Each germanium dimer is part of a $(\text{Ge-Ge})_{\parallel}/(\text{Ge-Ge})_{\perp}$ pair site, where they are positioned very closely together as seen in Figure 4b. In Figure 4b, features refer to moities of interest to defect formation, such as the two germanium dimer types, Ge-Se bonds, germaniums and seleniums for oxygen substitutional defects.

In Ref. [1], Edwards and Campbell reported that the variations in bond lengths of and bond angles involving Ge-Se are small, so we treat all Ge-Se equivalently; likewise, we also treat all selenium sites equivalently. The empty separations can represent extensive void environments in the Ge_2Se_3 material. The layers represent the denser environment in the Ge_2Se_3 material. Empty spaces within a layer correspond to micro-void environments in the Ge_2Se_3 material. The two types of germanium dimers can limitedly represent the local-environmentally varying germanium dimers in the Ge_2Se_3 material. The variational space of germanium dimers (orientation, bond lengths and local bond angles) may be enormous. $(\text{Ge-Ge})_{\parallel}$ and $(\text{Ge-Ge})_{\perp}$ are very different in orientation, bond lengths and local bond angles, so the two may represent enough of the variational space for our studies. $(\text{Ge-Ge})_{\parallel}/(\text{Ge-Ge})_{\perp}$ pairs can represent small groups or pairs of Ge-Ge dimers in the Ge_2Se_3 material.

3.2.2 *k*-Point Sampling Mesh

In Table 4, we present the results of the ***k***-point and real space sampling convergence studies on the 20-atom primitive unit cell. The criterion of this study for convergence is for the error$<$ 0.01 eV. The table shows significant and consistent differences from the 2x2x1 ***k***-point mesh to the 4x4x2 and 6x6x3 ***k***-point meshes with all

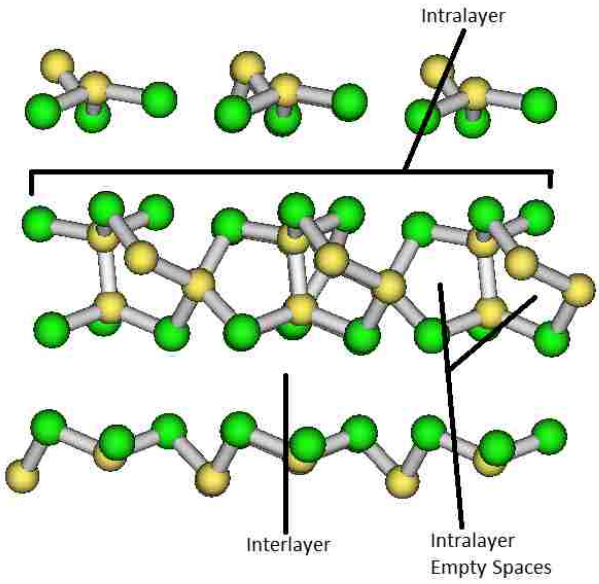

(a) Various environments

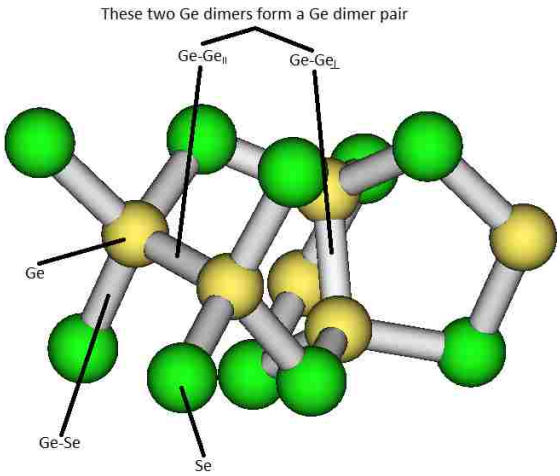

(b) Various local features

Figure 4: Structures in the crystalline model. These are locations of interest.

real space sampling. From 2x2x1 to 4x4x2, the energies differ consistently by around 0.035 eV for all real space sampling grids. From 4x4x2 to 6x6x3, the energy differences are negligible. Based on these results, the minimally sufficient $\boldsymbol{k}$-point mesh for the primitive unit cell is 4x4x2. For the 80-atom unit cell we mainly used, the $\boldsymbol{k}$-point mesh was appropriately scaled from 4x4x2 to 2x2x2.

Table 4: Convergence of $\boldsymbol{k}$-point and real space sampling for the 20-atom primitive unit cell. These energies are configuration energies relative the highest configuration energies in the set ($140 \times 140 \times 280$ real space sampling grid paired with $4 \times 4 \times 2$ and $6 \times 6 \times 3$ $\boldsymbol{k}$-point meshes) in eV.

	Real Space				
$\boldsymbol{k}$-Point	60 × 60 ×120	80 × 80 ×160	100 ×100 ×200	120 ×120 ×240	140 ×140 ×280
$2 \times 2 \times 1$	-0.0408	-0.03808	-0.03808	-0.03672	-0.03536
$4 \times 4 \times 2$	-0.00544	-0.00272	-0.00272	-0.00136	0
$6 \times 6 \times 3$	-0.00544	-0.00408	-0.00136	-0.00136	0

3.2.3 Real Space Sampling Grid

Table 4 shows minor differences with increasing real space sampling levels (60x60x120, 80x80x160, 100x100x200, 120x120x240 and 140x140x280). The differences were in the thousandth place in eV. The greatest energy difference was between 60x60x120 and 80x80x160. Grid spacing from 0.2-0.3 a_0/(grid point) is needed for atoms with very compact wave functions, which include oxygen [44]. With 75 grid points along that lattice vector, the grid spacing is 0.195 a_0/(grid point), which is more than sufficient. The minimally sufficient real space sampling grid for the primitive unit cell is 75x75x150. For the 80-atom unit cell, we appropriately scaled the real space sampling grid to 150x150x150.

Chapter 4: Oxygen Defects

4.1 Introduction and Approach

As stated in Section 1.3, oxygen is highly abundant and highly reactive, so it is important to investigate whether oxygen defects play a significant role in the electrical properties of EMB memristors. It is well known that atomic oxygen and O_2 defects exist in SiO_2 and play an important role in electrical properties and radiation response of semiconductor materials [82, 83]. Experimentally, Campbell has observed only atomic oxygen, not O_2, in the Ge_2Se_3-based memristors she has manufactured [84]. This motivates us to study the properties of oxygen defects in Ge_2Se_3 using the tools introduced in Chapters 2 and 3. Before presenting the results, the remainder of this section is devoted to the details of the approach and the analysis methods used for these defects.

4.1.1 Approach

In studying impurities, the examination focuses on the process of foreign atoms entering the material to form defect configurations. Standard states provides reference energies used in computing the energies of formation, seen in Eq. 1. Since the standard state of oxygen is O_2, this suggests we should look for defect configurations involving O_2 in addition to atomic oxygen. Figure 4a shows a number of environments for the atomic oxygen or O_2 to reside: interlayer, intralayer and intralayer void environments. Within the intralayer environment, we also sampled local features which are labeled in Figure 4b.

Based on thermodynamics, the configuration with the lowest energy of formation per defect atom is the lowest energy configuration, which is the most abundant. The relative abundance of these defect configuration, thus their relevance to this study,

is assessed by comparing their energies with this lowest energy configuration. The changes to electronic properties of the host crystal due to relevant defect configurations reflect the effects of corresponding impurities in the material. Lastly, we used projected density of states analyses to extract information on the electrical properties of these preferred configurations.

4.1.2 Energy of Formation

The related defect formation process begins with the foreign atom outside the host crystal in its standard state and ends with the isolated neutral defect configuration. The energy change associated with this defect formation process is the energy of formation of interest. If $\Delta E_f < 0$, the defect formation process is exothermic; if $\Delta E_f > 0$, the defect formation process is endothermic. Thermodynamically, if the process is exothermic, then it will complete without aid; if endothermic, then it will not.

4.1.3 Equilibrium Statistical Thermodynamics and Kinetics

Energies of formation comparisons are interpreted by equilibrium statistical thermodynamics [85]. In thermodynamic equilibrium, the probability $P(E)$ for the defect system to take a specific stable configuration is related to the partition function and Boltzmann factor as

$$P(E) = \frac{1}{Z} e^{-\frac{E}{K_B T}}. \tag{19}$$

Here, Z is the partition function, E is the configuration energy, T is the temperature and K_B is Boltzmann's constant. The probability ratio, which is also abundance ratio, between two defect formation processes with the same numbers and types of elements is

$$\frac{P_1(\Delta E_{f,1})}{P_2(\Delta E_{f,2})} = e^{-\frac{(\Delta E_{f,1} - \Delta E_{f,2})}{K_B T}}. \tag{20}$$

To use the above expression to determine relative abundances of defects, we used the fabrication process temperature, as it most likely will reflect the defect distribution. The temperature of the wafers during the fabrication process of Ge_2Se_3 is less than 80 C° [84]. For both silver and oxygen defects, we used 360 K is the temperature of defect processes in these studies. For the abundance ratio to be 1:500 at 360 K, $\Delta E_{f,1} - \Delta E_{f,2}$ is roughly 0.2 eV. We regard defects with abundance ratio relative to the lowest energy/most abundant configuration of less than 1:500 to be not relevant to this study. Thus defects with energies such that $\Delta E_{f,2} - \Delta E_{f,min} > 0.2$ eV, where $\Delta E_{f,min}$ is the energy of formation of the lowest energy configuration, irrelevant as it is relatively rare.

In our studies, we have also considered the kinetics of some defect formation processes. The kinetics of these defect processes depends on the activation energy and attempt frequency. The rates for the processes of interest are given by the Arrhenius equation [86, 87],

$$k = Ae^{-\frac{E_a}{K_B T}} \tag{21}$$

Here, k is the rate, A is the attempt frequency, and E_a is the activation energy. The timescale for a process is inverse of the rate. If the timescale for a process is about one month given at a 10^{13} Hz attempt frequency[47], then E_a is roughly 1.40 eV at 360 K. Processes with $E_a > 1.40$ eV are not observable on typical experimental timescales.

[47] This attempt frequency figure is a safe over-estimate. Refer to appendix section A.1. Using the stricter criterion did not change the conclusions of this thesis.

4.1.4 Band Gap, Gap State and Electron Localization

As mentioned in Subsection 2.1.9, projected density of states analysis reveals band structure information, such as band edges, band gap and gap state and allows for studying electron localization. The band gap and potential electron localization determine certain electrical properties of the material. Consider Figure 13a, the complete projected density of states plot of the host crystal. The Fermi level (ε_F) in a semiconductor is the energy of an hypothetical state that if it existed would have a 50% occupation probability in thermodynamic equilibrium [88], and we use it to determine the location of the band gap region. In Figure 13b, we have zoomed into the band gap region of Figure 13a. The energy range with no bulk atom single electron states[48] is the band gap, and it separates the valence and conduction bands. The lower and upper ends of the band gap are respectively the valence band edge and conduction band edge.

In this thesis, we are looking at extrinsic point defects, and there are two types of extrinsic point defects, solutes and impurities; solutes result from intentional introductions of foreign atoms into a material, and impurities result from unintentional introductions [89]. Doping a semiconductor is the intentional introduction of foreign atom (extrinsic) defects to dramatically change the conductivity of the semiconductor. To achieve this, the dopants create single electron states in the band gap (gap states) and introduce excess or deficit of electrons in very specific ways [90]. Impurities can function similarly as dopants to create gap states; gap state indicates sites of potential spatial electron localization. These sites include defect sites and sites in certain materials that can inherently trap excess electrons [16, 17].

In examining a configuration with electron localization, one would observe a gap state in the projected density of states figure, and the atoms corresponding to that

[48]Bulk atoms are not within the effect range of defects. In this case, all atoms are bulk, because there is no defect in the host crystal.

state would have density of states in the gap, and the electron in that state is spatially localized.

4.2 Preliminary Studies

So far, our discussions have strictly been on the theoretic and modeling framework for studying extrinsic defects in Ge_2Se_3, provided calculation details and mapped out the research procedures; we now present the results, starting with two preparatory sets of calculations. The first set, a defect cell size convergence study, determines the minimally sufficient cell size for studying oxygen defects. The second set determined preferences of spin configurations oxygen structure. Tables 5 and 6 list all oxygen defects examined in this thesis and their respective designations.

Table 5: Oxygen defect designations (1). Listing of 1-atomic oxygen defects examined, their respective figure # and designation.

Environment	Oxygen Form	Defect Type	Notes	Figure	Designation
Intralayer	1 oxygen atom	Substitution	1 germanium	Not Included	O_{Ge}
Intralayer	1 oxygen atom	Substitution	1 selenium	6b	O_{Se}
Intralayer	1 oxygen atom	Displacement	1 selenium, and it relaxed interstitially elsewhere	Not Included	O_{Se}:I_{Se}
Intralayer	1 oxygen atom	Bridging Interstitial	$(Ge\text{-}Ge)_{\perp}$	11b	$BO_{\perp}$
Intralayer	1 oxygen atom	Bridging Interstitial	$(Ge\text{-}Ge)_{\parallel}$	5b	$BO_{\parallel}$
Intralayer	1 oxygen atom	Bridging Interstitial	Ge-Se	Not Included	$BO_{Ge\text{-}Se}$

Table 6: Oxygen defect designations (2). Listing of O_2 and 2-atomic oxygen defects examined, their respective figure number and designation.

Environment	Oxygen Form	Defect Type	Notes	Figure	Designation
Interlayer	O_2	Interstitial	Located at layer surface	7b	$I_{O_2}{}^{(1)}$
Intralayer	O_2	Interstitial		7c	$I_{O_2}{}^{(2)}$
Interlayer	2 oxygen atoms	Interstitial		8a	$I_{2O}{}^{(1)}$
Intralayer	2 oxygen atoms	Interstitial		8b	$I_{2O}{}^{(2)}$
Intralayer	2 oxygen atoms	Bridging Interstitial	Closest $(Ge\text{-}Ge)_{\perp}$ and $(Ge\text{-}Ge)_{\parallel}$	8d	$[BO_{\perp}{:}BO_{\parallel}]$

We now briefly explain the defect designation conventions used. The designations reflect defect type (substitution, interstitial or bridging interstitial) and elements involved. A_B denotes that atom A has substituted atom B, and I_C denotes an interstitial atom C defect. The super-scripted designation numbers, (1), (2), etc, only discriminate one defect configuration from another and do not infer configuration characteristics. "BO" denotes specifically an atomic oxygen bridging a dimer, and the corresponding subscripts, $\perp$, $\parallel$ and Ge-Se, denotes the dimer type, $(Ge\text{-}Ge)_{\perp}$, $(Ge\text{-}Ge)_{\parallel}$ and Ge-Se, respectively. Defect D : Defect E is a combination defect and denotes multiple defects in one unit cell; $F_G{:}I_G$ represents atom F displacing atom G. Defect H + Defect J denotes two infinitely separated and thus non-interacting defects and is useful for comparisons with interacting combination defects. The energy of formation of this combination is the sum of the energies of formation of those two individual defects. Lastly, [Defect K : Defect L] denotes an intimate-pair.

4.2.1 Atomic Oxygen Defect Cell Size Convergence Study

In this study, we determined the minimally sufficient cell size for studying atomic oxygen defects, i.e. the cell size for which the defect can be regarded as not interacting with its periodic images. The results provided confidence for the assertion made in Subsection 2.1.6 about defect interaction range. The criterion of this study for convergence is for the energy difference to be less than 0.05 eV. Table 7 shows that the difference of energies of formation of $BO_{\parallel}$ (shown in Figures 5a and 5b) at the 20-atom and 80-atom cell sizes is 0.058 eV and is marginally too large for infinite dilution energy convergence. Thus, the defect interaction range is slightly larger than the primitive unit cell for $BO_{\parallel}$. The energies of formation at the 80-atom and the 360-atom cell sizes differ by only 0.015 eV, so the minimally sufficient cell size is between the 20-atom and 80-atom cell sizes.

To obtain the $BO_{\parallel}$ defect, we placed the atomic oxygen next to the center of $(Ge\text{-}Ge)_{\parallel}$, and it spontaneously bridged the dimer.

Table 7: Convergence of energies of formation of 3 oxygen defects for 3 different unit cell sizes.

	Energies of Formation (eV)		
Defect	20-Atom	80-Atom	360-Atom
$BO_{\parallel}$	-2.008	-2.066	-2.051
O_{Se}	-1.36	-1.469	-1.495
$BO_{\perp}$	Not Available	-1.673	-1.705

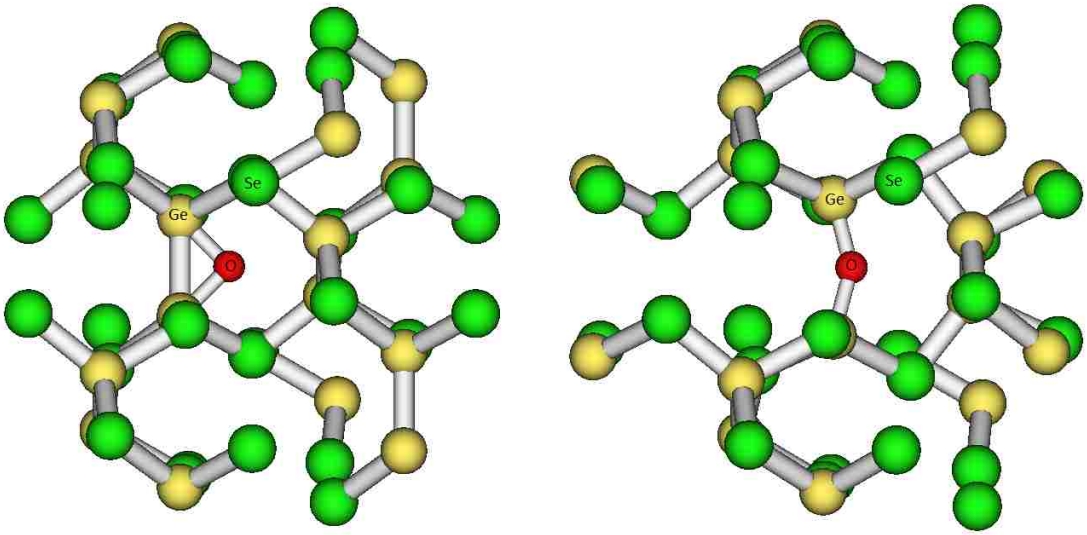

(a) Starting geometry of $BO_{\parallel}$.

(b) Relaxed geometry of $BO_{\parallel}$.

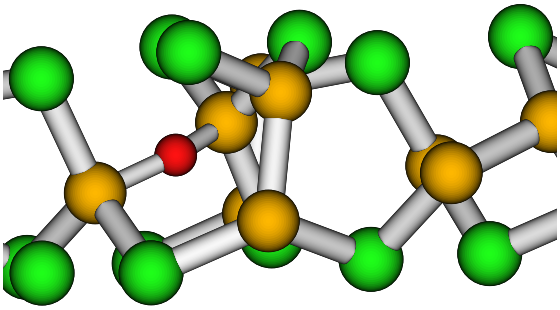

(c) Relaxed geometry of $BO_{\parallel}$ in orientation to show layers.

Figure 5: Starting and relaxed geometries of $BO_{\parallel}$. No other major geometry relaxation occurred; for all defects in this thesis, we discussed all relevant geometry relaxation. For all geometry figures, oxygen atoms are indicated in red. Most figures are not in the same orientation as Figures 3a and 3b; we oriented geometry figures in this thesis to best show the defect(s). From Figure 5c, we see the Ge-O-Ge bridge is parallel to the layer.

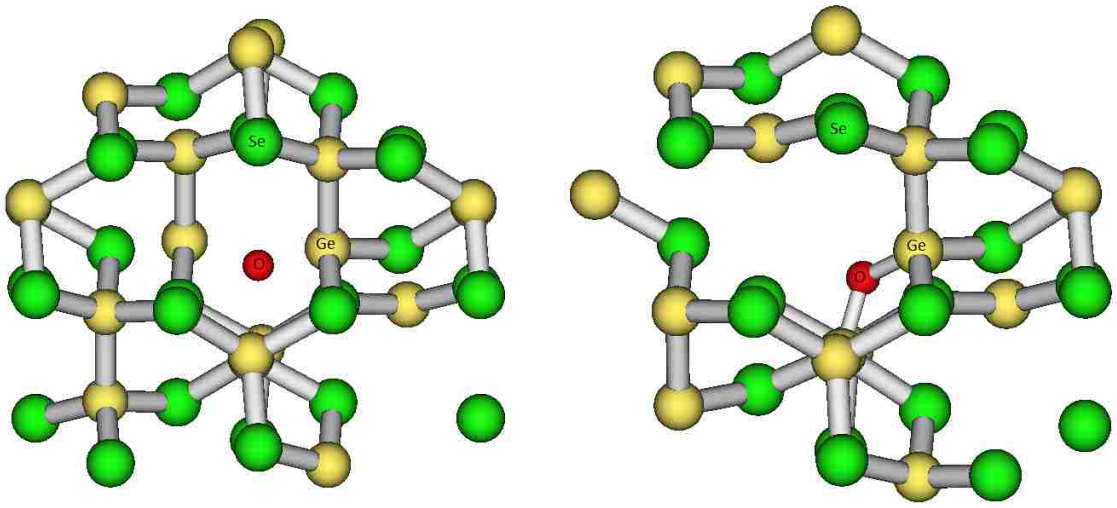

(a) Starting geometry of O_{Se}. (b) Relaxed geometry of O_{Se}.

Figure 6: Starting and relaxed geometries of O_{Se}.

For O_{Se} (shown in Figures 6a and 6b), the difference of energies of formation at the 20-atom and the 80-atom cell sizes is 0.106 eV, which is too large for infinite dilution energy convergence. The energies of formation at 80-atom and 360-atom cell sizes agree to 0.026 eV. Thus, the minimal sufficient cell size for O_{Se} is between 20 and 80 atoms.

To obtain the O_{Se} defect, we started with the host crystal cell, changed one of the selenium to an oxygen and left the configuration relax. Note that there is an activation energy associated with atomic oxygen displacing a selenium, so there may be an activation energy associated with this defect.

The 80-atom cell size is sufficient for studying atomic oxygen and 2-neighboring atomic oxygen defects in the crystalline model. This is the same 80-atom unit cell used in Refs. [1, 16, 17]. We did not discuss the trend for the $BO_{\perp}$ defect, because we do not have the data for the $BO_{\perp}$ defect at the 20-atom unit cell size.

4.2.2 Oxygen Defect Low Spin and High Spin Calculations

In isolation, the triplet state O_2 is preferred, and this study begins with this fact. Oxygen form, environment and high/low spin may interact unexpectedly; high spin O_2 may not be preferred over high spin O_2 or high/low spin atomic oxygen in intralayer locations. We examined five different oxygen defects, consisting of two O_2 and three 2-atomic oxygen configurations (shown in Figures 7b, 7c, 8a, 8b and 8d). ${I_{O_2}}^{(1)}$ and ${I_{2O}}^{(1)}$ are interlayer defect configurations, and ${I_{O_2}}^{(2)}$, ${I_{2O}}^{(2)}$ and $[BO_\perp{:}BO_\parallel]$ are intralayer defect configurations. Table 8 shows that the energy of formation differences from high spin to low spin were greater than 0.8 eV for all defects. The low spin configurations are preferred over high spin. Note that the computed energies for isolated O_2 with low spin and high spin have the triplet state preferred as expected from Hund's rule [91].[49]

Table 8: Examination of energies of formation to determine preferred spin, environments and oxygen form.

Defect	Low Spin ΔE_f (eV)	High Spin ΔE_f (eV)	Energy Difference (H-L)
${I_{O_2}}^{(1)}$	-0.109	0.721	0.829
${I_{O_2}}^{(2)}$	0.095	1.482	1.387
${I_{2O}}^{(1)}$	-1.972	-0.966	1.006
${I_{2O}}^{(2)}$	-1.659	-0.653	1.006
$[BO_\perp{:}BO_\parallel]$	-3.930	-2.761	1.169

To obtain the ${I_{O_2}}^{(1)}$ and ${I_{O_2}}^{(2)}$ defects, we placed O_2 in the interlayer and intralayer environments in host crystal cells and left these configurations to relax. All calculations, the ones shown above and others, involving inserting O_2 into locations of interest have starting geometries with O-O bond lengths around the typical 1.21 Å. To obtain the ${I_{2O}}^{(1)}$ and ${I_{2O}}^{(2)}$ defects, we placed two atomic oxygen in the intralayer and interlayer environments and left these configurations to relax. To obtain

[49] We used Eq. 1 and the configuration energy of gaseous O_2 to compute many energies of formation of defects in this thesis.

the $[BO_{\perp}:BO_{\parallel}]$ defect, we placed the O_2 between two Ge-Ge dimers, and it spontaneously dissociated during relaxation.

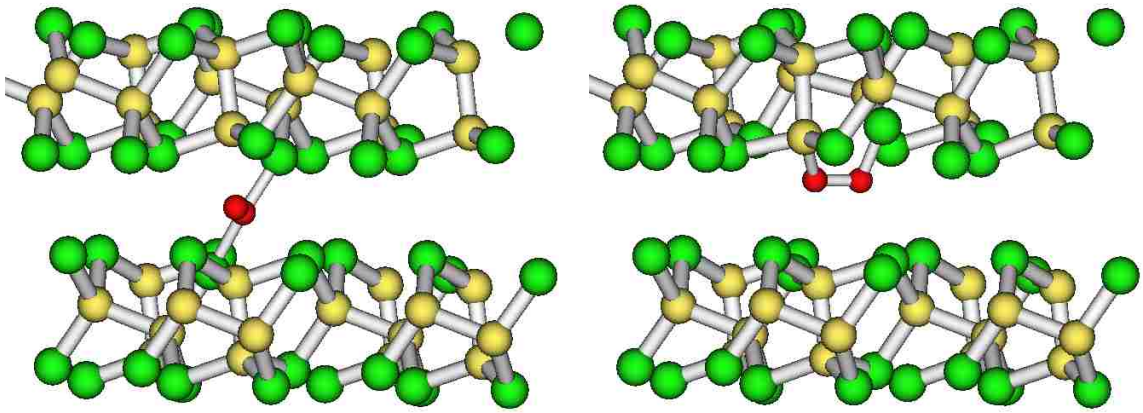

(a) Starting geometry of $I_{O_2}{}^{(1)}$.

(b) Relaxed geometry of $I_{O_2}{}^{(1)}$.

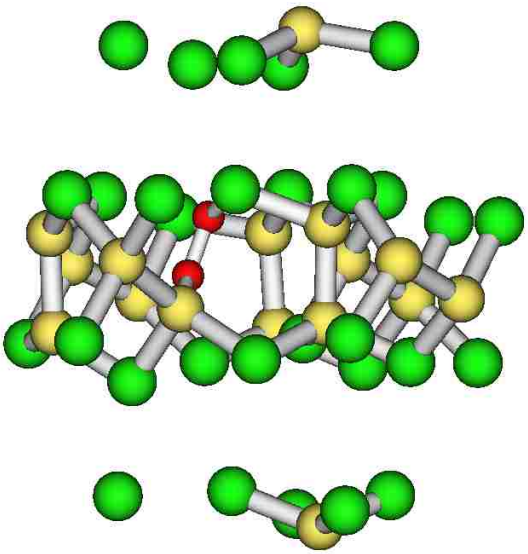

(c) Relaxed geometry of $I_{O_2}{}^{(2)}$.

Figure 7: Starting and relaxed geometries of an interlayer O_2 defect and an intralayer O_2 defect.

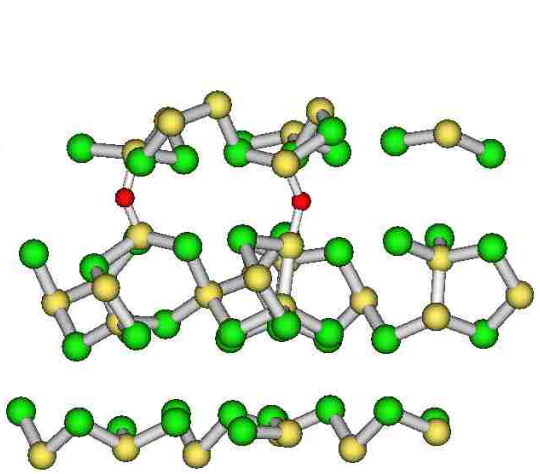

(a) Relaxed geometry of $I_{2O}{}^{(1)}$.

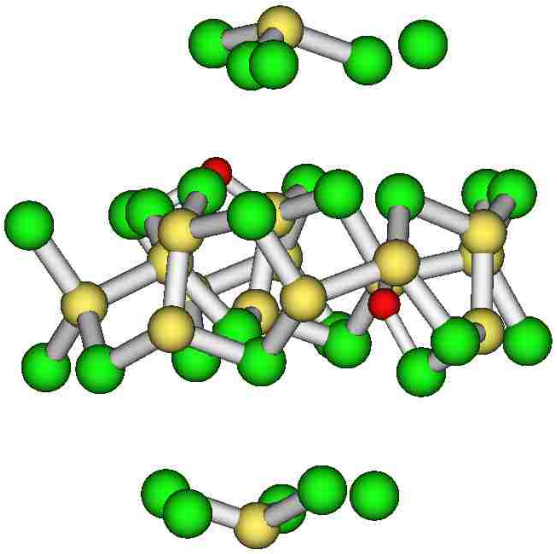

(b) Relaxed geometry of $I_{2O}{}^{(2)}$.

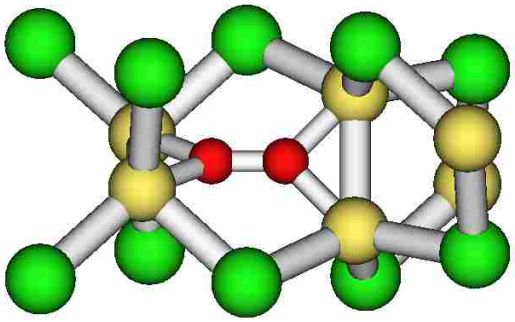

(c) Starting geometry of $[BO_{\perp}{:}BO_{\parallel}]$.

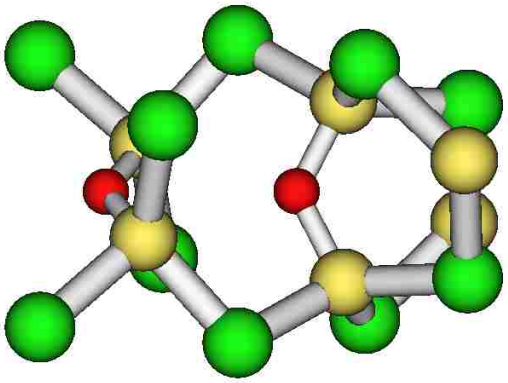

(d) Relaxed geometry of $[BO_{\perp}{:}BO_{\parallel}]$.

Figure 8: Starting and relaxed geometries of 2 two-atomic oxygen defect and an O_2 defect between 2 Ge-Ge dimers.

4.2.3 Oxygen Form

Continuing with just the low spin portion of Table 8, we note that relaxing an O_2 at an empty space inside a layer or at the surface of a layer corresponds to an endothermic process or a barely exothermic process, respectively; the energy of for-

mation of $I_{O_2}{}^{(2)}$ is positive, and the energy of formation of $I_{O_2}{}^{(1)}$ is barely negative. Thus, the two processes of bringing O_2 from outside and placing it inside the crystalline model are unfavorable. On the other hand, all processes of bringing O_2 from outside, dissociating it and placing the two atomic oxygen inside the crystalline model are highly exothermic; energies of formation of $I_{2O}{}^{(1\text{-}3)}$ are all highly negative. From the thermodynamic perspective, these results imply preference for O_2 dissociation.

Below, we present a possible path of O_2 dissociation. Figures 7a and 7b show that the interlayer O_2 spontaneously forms a peroxide linkage between a germanium and selenium at the surface of a layer after relaxation. This indicates oxygen will travel toward dense locations and bond with germaniums and seleniums. Specifically regarding $I_{O_2}{}^{(1)}$, the calculated O-O bond length is 1.509 Å, and the experimental O-O bond length of hydrogen peroxide is 1.49 Å [92]. The peroxide linkage formed relatively strong bond with the germanium and selenium. Note that $I_{O_2}{}^{(1)}$ and $I_{O_2}{}^{(2)}$ are both peroxide linkage configurations; the energy of formation of $I_{O_2}{}^{(1)}$ is lower than that of $I_{O_2}{}^{(2)}$ by 0.204 eV.

Next, in Figure 9, the NEB transition state calculation for a path from defect configuration $I_{2O}{}^{(2)}$ to defect configuration $I_{O_2}{}^{(2)}$ strongly supports dissociation in the intralayer environment. To dissociate O_2 to form two atomic oxygen, the reverse reaction, requires 2 eV, but the forward reaction only requires 0.27 eV. We have not studied the kinetics of the formation of the $I_{O_2}{}^{(2)}$ defect. Lastly, if O_2 is placed in between two seleniums (shown in Figure 10a), then O_2 spontaneously dissociates after relaxation (shown in Figure 10b). We see the same behavior again in Figures 8c and 8d, where O_2 was initially placed in the middle of a $(\text{Ge-Ge})_{\parallel}/(\text{Ge-Ge})_{\perp}$ pair.

We investigated the potential for O_2 to dissociate by nearby seleniums by placing O_2 between two seleniums, each at a layer surface, and the O_2 dissociates into two atomic oxygen. The relaxed geometry showed that the distance between the two atomic oxygen is 2.77 Å, which is more than 1 Å greater than typical O-O bond

lengths and signifies O_2 dissociation.

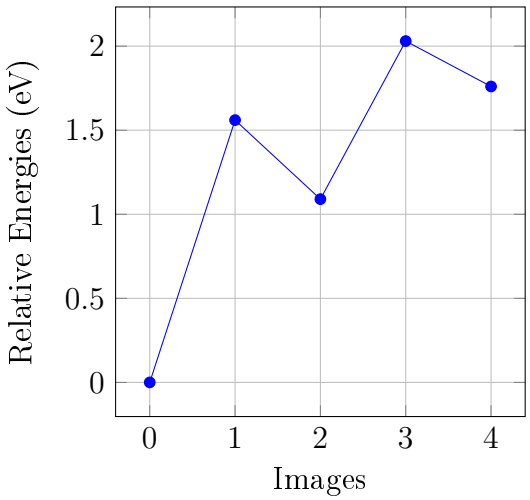

Figure 9: Transition state path energies between ${I_{2O}}^{(2)}$ (Image 0) and ${I_{O_2}}^{(2)}$ (Image 4) computed using the NEB method.

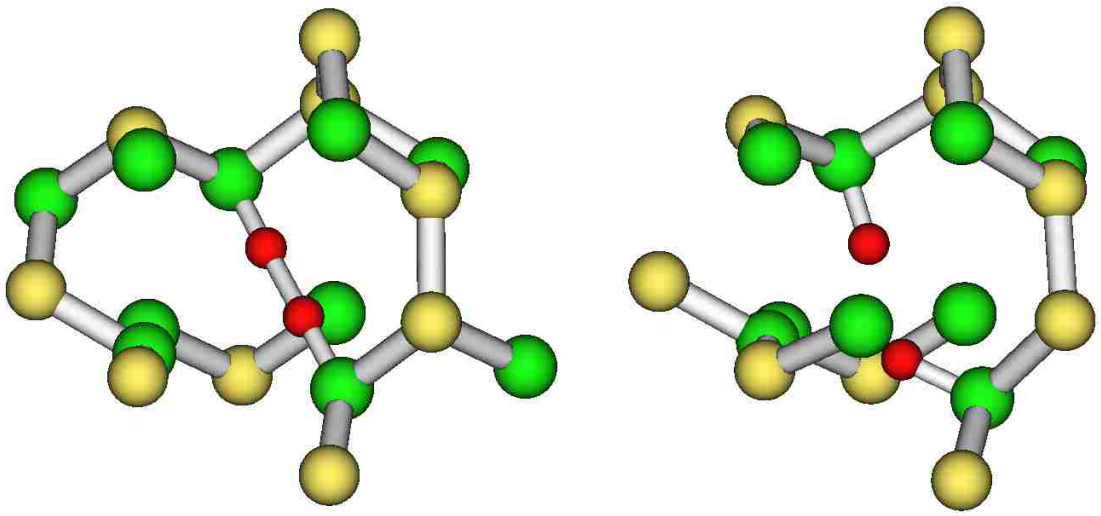

(a) Starting geometry of O_2 between 2 seleniums. (b) Relaxed geometry of O_2 dissociates between 2 seleniums.

Figure 10: Starting and relaxed geometries of interstitial O_2 placed between 2 seleniums. The distance between the 2 atomic oxygen after relaxation is 2.77 Å.

Based on the results, we see that O_2 tends to travel toward dense locations, where it will readily dissociate, and we find that the only relaxed oxygen form in Ge_2Se_3 is atomic oxygen. These conclusions agree with Campbell's experimental results, where Campbell observed only atomic oxygen in the material [84]. Our conclusions also agree with experimental results by Yan *et al.*, where they observed atomic oxygen bridging Ge-Ge dimers to form Ge-O-Ge bridges [93].

4.3 Intralayer Atomic Oxygen Defect Configuration Preferences

In Section 4.2, we identified the most probable oxygen form, which narrowed the variational space of defect configurations moving forward. Next, we examined the energetic preference of intralayer atomic oxygen defect configurations to compare their energies with the interlayer oxygen defect configurations and also determine the relevant atomic oxygen defects. Lastly, we looked at the potential of intralayer atomic oxygen defects to cluster.

In general, the internal structures of amorphous semiconductors follow continuous random network arrangements, i.e. the valence of all atoms must be satisfied. Valence satisfaction and conclusions from the last section guide this defect study. Our examination of on-site defects, such as substitutional defects or bond bridging defects, satisfies the 2-fold coordinated atomic oxygen valence without needlessly altering their geometry; this potentially provides stable and low energy atomic oxygen defect configurations.

The final set of studies present projected density of states analyses of the host crystal system and oxygen defect systems to determine the effects of oxygen defects on band structure. Due to a tendency of DFT to underestimate the band gap [79], we focused on trends only, in particular, the effects of defects on the band gap and

the potential introduction of gap state.

4.3.1 Intralayer Atomic Oxygen Defect Energetics

We studied five possible intralayer atomic oxygen substitution or bond bridging defects. The results in Tables 8 and 9 show that atomic oxygen defects prefer the intralayer environment. To compare 1-atomic oxygen defects with 2-atomic oxygen and O_2 defects, we normalize the energies of formation by the number of atomic oxygen in the cell. The lowest intralayer on-site atomic oxygen defects, O_{Se}, $BO_{\perp}$ and $BO_{\parallel}$, all have much lower energies of formation per atomic oxygen than the interlayer 2-atomic oxygen and O_2 defects, ${I_{O_2}}^{(1)}$ and ${I_{2O}}^{(1)}$.

To obtain $BO_{\perp}$, we placed atomic oxygen next to the center of $(Ge\text{-}Ge)_{\perp}$, and it spontaneously bridged the dimer.

Table 9: Energies of formation of intralayer atomic oxygen defects. In the case of O_{Se}:I_{Se}, we also considered several locations for the displaced selenium, and the lowest energy defect is listed.

Defect	Cell Size	ΔE_f (eV)	ΔE_f Relative to Lowest Energy Configuration (eV)
O_{Ge}	80	1.061	3.210
O_{Se}	80	-1.469	0.680
O_{Se}:I_{Se}	80	-1.333	0.816
$BO_{\perp}$	80	-1.673	0.476
$BO_{\perp}$	360	-1.705	0.480*
$BO_{\parallel}$	80	-2.149	0
$BO_{\parallel}$	360	-2.185	0*
$BO_{Ge\text{-}Se}$	80	-0.884	1.265

Next, we show in Table 9 the only relevant atomic oxygen defect is $BO_{\parallel}$ (shown in Figures 5a and 5b). While $BO_{\perp}$ (shown in Figures 11a and 11b) is not relevant, these two atomic oxygen defects together are the atomic oxygen-bridging germanium dimer defect type and limitedly represent atomic oxygen-bridging the environmentally

varying germanium dimers in Ge_2Se_3. As before, if the two types of germanium dimers represent enough of the variational space of germanium dimers, then the atomic oxygen-bridging germanium dimer defect type may be represented adequately by $BO_\perp$ and $BO_\parallel$. From the germanium dimer's perspective, the atomic oxygen occupies the dimer by bridging the dimer.

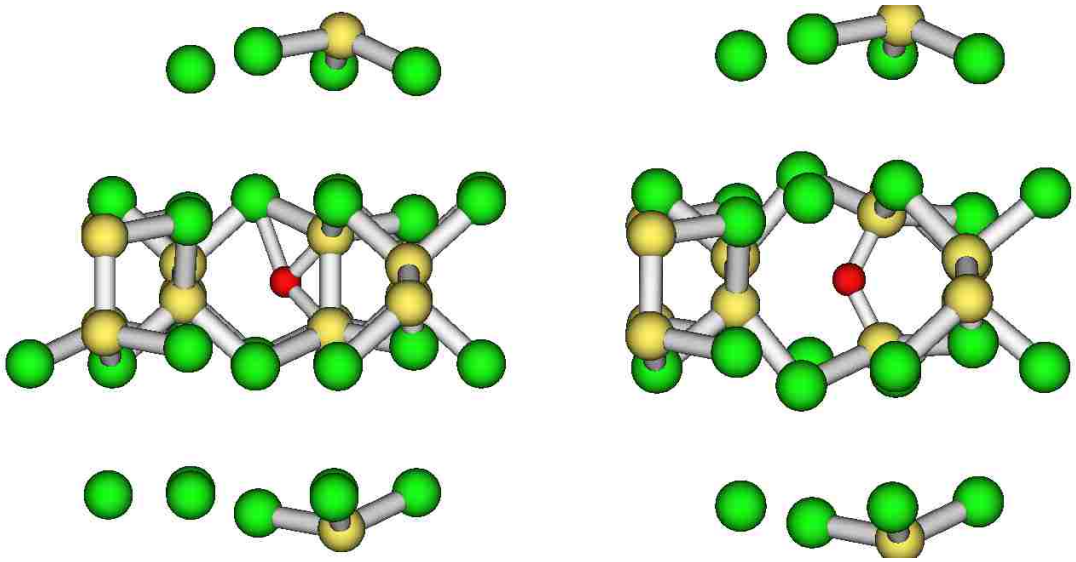

(a) Starting geometry of $BO_\perp$.

(b) Relaxed geometry of $BO_\perp$.

Figure 11: Starting and relaxed geometries of $BO_\perp$. From Figures 11a and 11b, we see the Ge-O-Ge bridge is perpendicular to the layer.

Our attention now shifts to preference of defect types, specifically whether the atomic oxygen-bridging germanium dimer defect type is preferred over the others. With energy of formation of $BO_\perp$ as the upper bound for its type, the next lowest energy configuration, O_{Se} (shown in Figures 6a and 6b), is still more than 0.2 eV higher, which corresponds to the thermodynamic preference of atomic oxygen-bridging germanium dimer defect type over the others. Regarding kinetics, $BO_\perp$ and $BO_\parallel$ do not possess formation activation energy requirements. No further studies on the kinetics of other atomic oxygen defect types is necessary, because they can only optimally lack

formation activation energy requirements; thermodynamic analysis is enough.

Lastly, we note the abundance of germanium dimers in Ge_2Se_3 .[50] Only complete (at least locally) saturation of them by atomic oxygen will cause O_{Se} to be relevant. We are thus convinced that the atomic oxygen-bridging germanium dimer defect type is the preferred oxygen defect type in Ge_2Se_3. In Ge_2Se_3 contaminated by high oxygen density or in selenium-rich Ge_xSe_{1-x} systems, O_{Se}, atomic oxygen-bridging Se-Ge and atomic oxygen-bridging selenium dimer defect types may play a greater role.

4.3.2 Clustering Behavior of Atomic Oxygen Defects

At the end of the previous subsection, we concluded atomic oxygen-bridging germanium dimer defect type is the only overall relevant defect type. Due to the overwhelming preference of atomic oxygen-bridging germanium dimer defect type,[51] movements of atomic oxygen within the material require those atoms to vacate from occupying germanium dimers. Movement of impurities are necessary for their clustering; immobile[52] impurities will not achieve thermodynamic distribution of configurations in meaningful timescales and thus will not cluster.

In Figure 12, the NEB transition state calculation for a path from defect configuration $BO_\perp$ to defect configuration $BO_\parallel$ strongly indicates immobile atomic oxygen. It shows that the intra-dimer group motion requires an 1.99 eV activation energy. As stated previously, the atomic oxygen-bridging germanium dimer defect type lacks formation activation energy requirements. The energy requirement for atomic oxygen to vacate from occupying germanium dimers is the major contribution to the barrier in Figure 12. The 1.99 eV barrier height is characteristic of the escape activation

[50] The Ge_2Se_3 system has one Ge-Ge dimer per five atoms.

[51] $BO_\perp$ is preferred over O_{Se}, the runner-up, by 0.204 eV, so the probability ratio of $BO_\perp$ to O_{Se} is $717:1$. The probability ratio of the two respective defect types should be similar optimally for the oxygen substituion of selenium defect type.

[52] From Subsection 4.1.3, a > 1.4 eV activation energy implies the defect formation is not observable. Impurities, taking on a preferred defect configuration with > 1.4 eV escape activation energy, are immobile.

energy of the defect type. Without additional calculations, we conclude that oxygen atoms are immobile after being introduced into Ge_2Se_3, so oxygen impurities will not cluster.

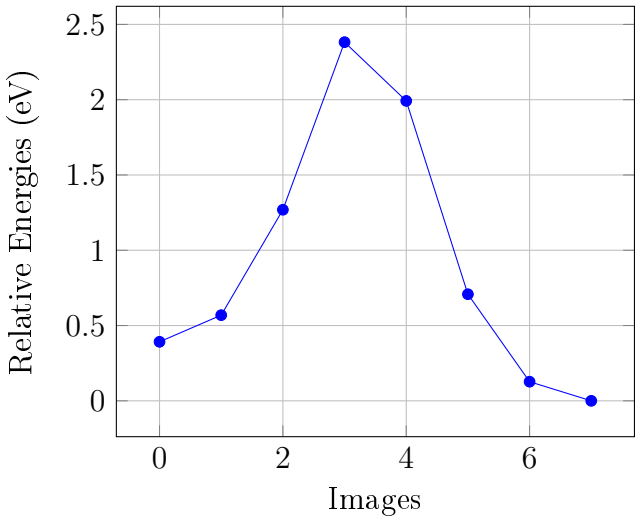

Figure 12: Transition state path energies between $BO_\perp$ (Image 0) and $BO_\parallel$ (Image 7).

4.3.3 Projected Densities of States of Host Crystal and Defect Configurations

Our oxygen defect study concludes with projected density of states analyses of the host crystal and defected systems. In these projected density of states figures, we plotted the projected densities of states of bulk germanium and selenium, which showed the band edges, in blue and green respectively, of the atomic oxygen defect in red and of any atoms contributing significantly to the gap state. Figures 13a and 13b show that Fermi level of the host crystal is -4.98 eV, and the band gap is 0.89 eV. We observe a clean gap, i.e. there is no gap state. Figures 14a and 14b show that the band gap of $BO_\parallel$ is 0.81 eV. Note that the germanium and selenium densities of states are altered by the presence of the defect, but no localized state is introduced

into the gap.

$BO_{\parallel}$ did not significantly alter the band gap or introduce gap state. Examination of the projected density of states for the next two lowest energy configurations (shown at Figures 15a and 15b for $BO_{\perp}$. Figures 16a and 16b for O_{Se}.) leads to similar results. As $BO_{\perp}$, $BO_{\parallel}$ and potentially O_{Se} represent virtually all observable oxygen defect configurations, we are convinced oxygen will not change the electrical properties of Ge_2Se_3 through alteration of the band gap or introduction of gap state.

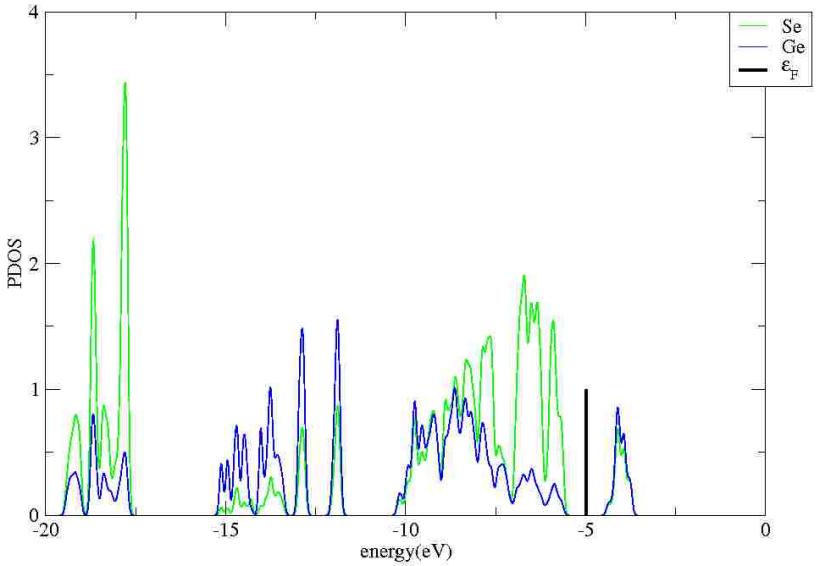

(a) Computed projected density of states.

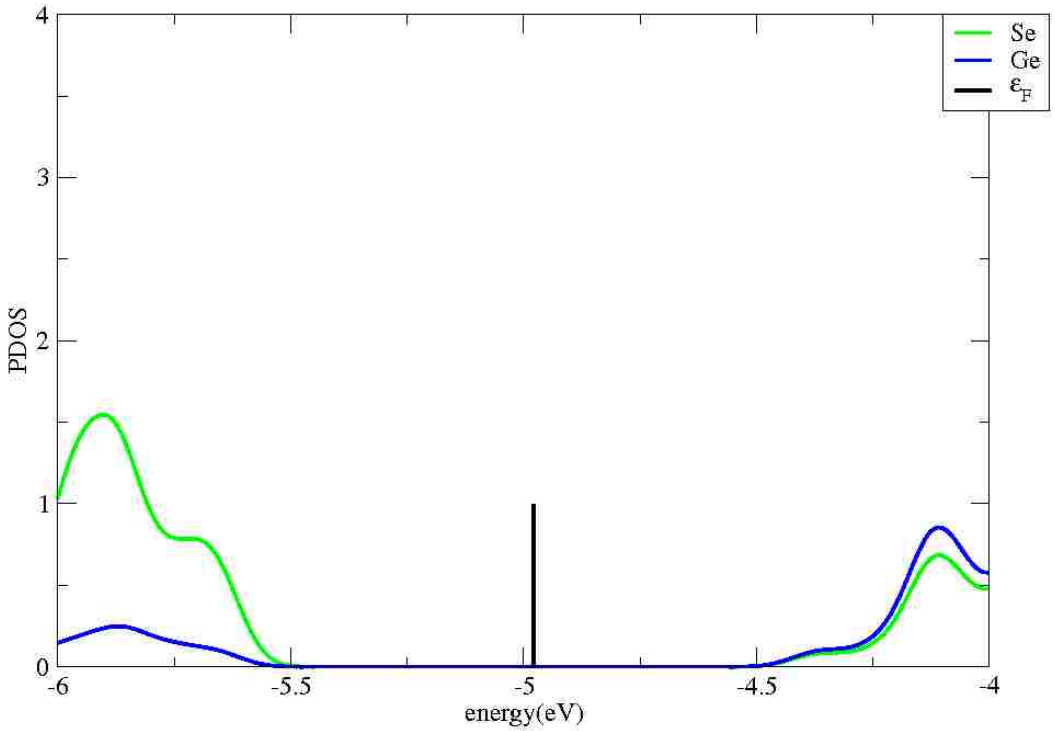

(b) Projected density of states in the band gap region.

Figure 13: Projected density of states of host crystal of the crystalline model of Ge_2Se_3. The valence band edge is at -5.44 eV, and the conduction band edge is at -4.55 eV.

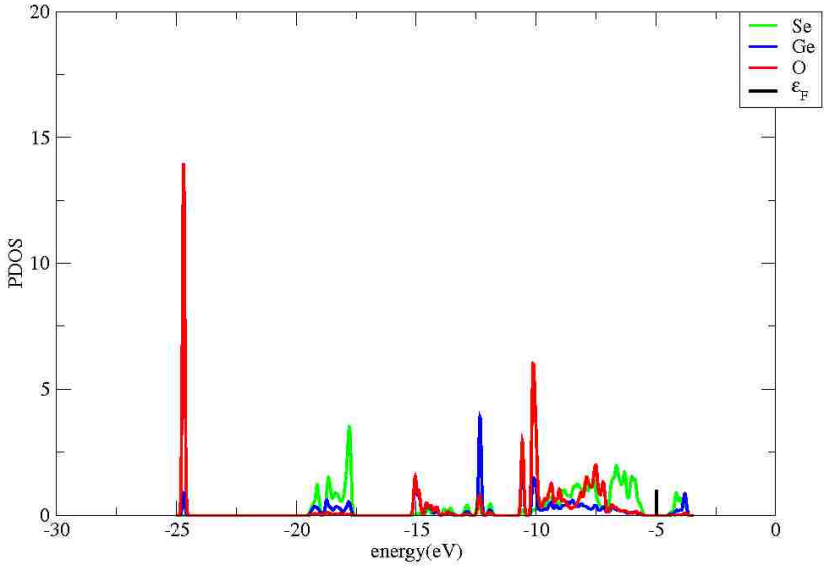

(a) Computed projected density of states.

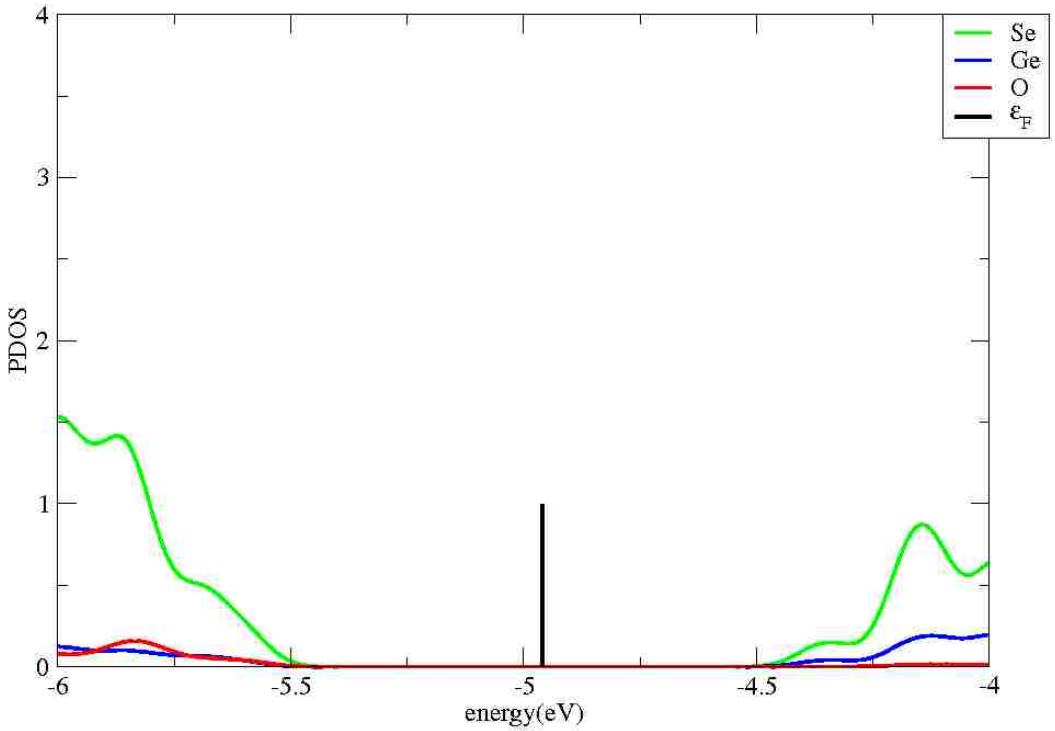

(b) Projected density of states in the band gap region.

Figure 14: Projected density of states of $BO_{\parallel}$ configuration. The valence band edge is at -5.37 eV, and the conduction band edge is at -4.55 eV. The germanium and selenium shown corresponds to atoms adjacent to the defect.

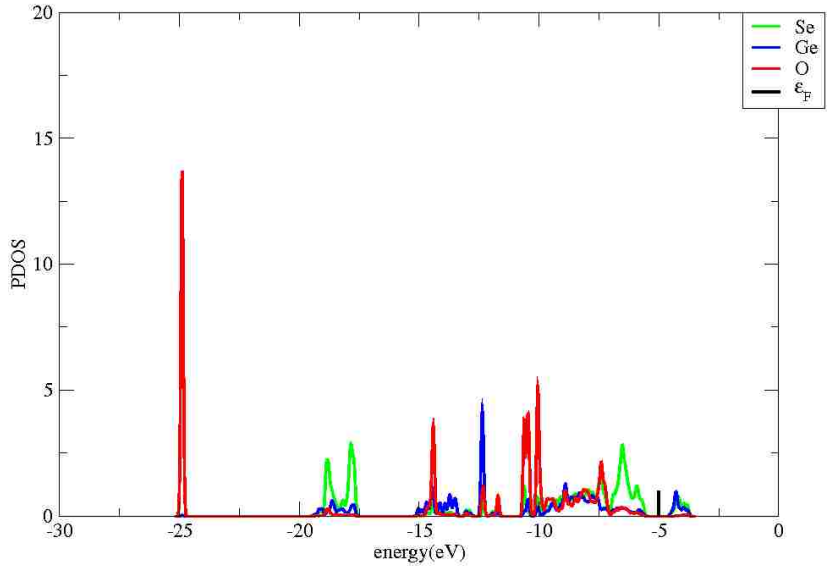

(a) Computed projected density of states.

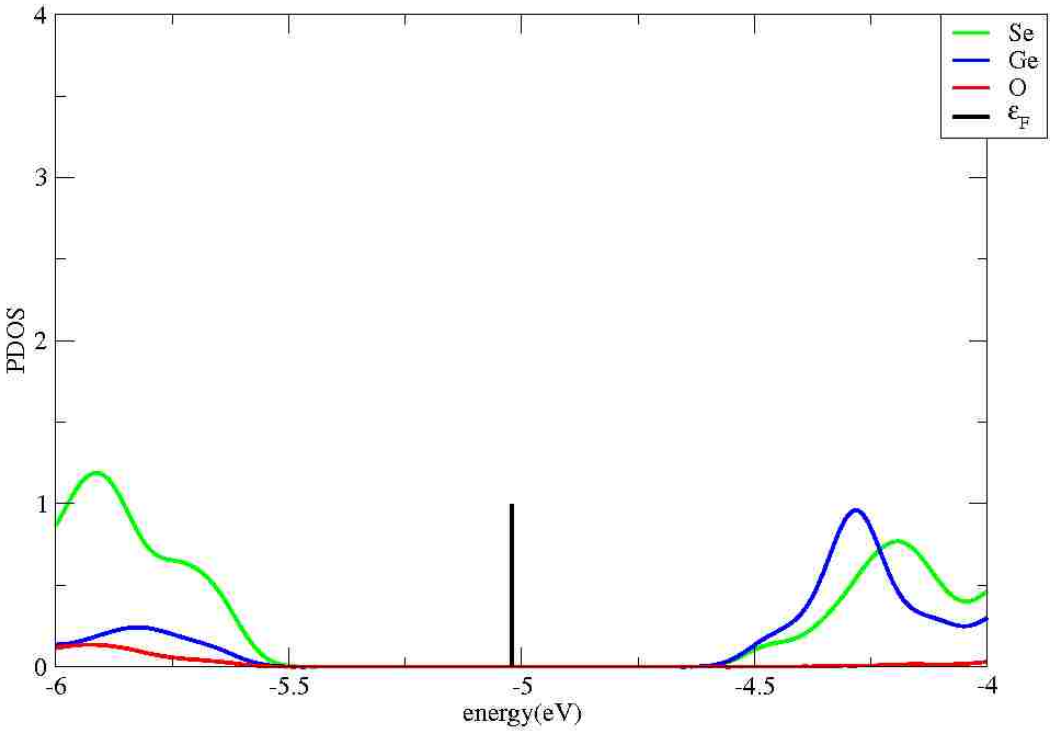

(b) Projected density of states in the band gap region.

Figure 15: Projected density of states of $BO_{\perp}$ configuration. The valence band edge is at -5.46 eV, and the conduction band edge is at -4.64 eV.

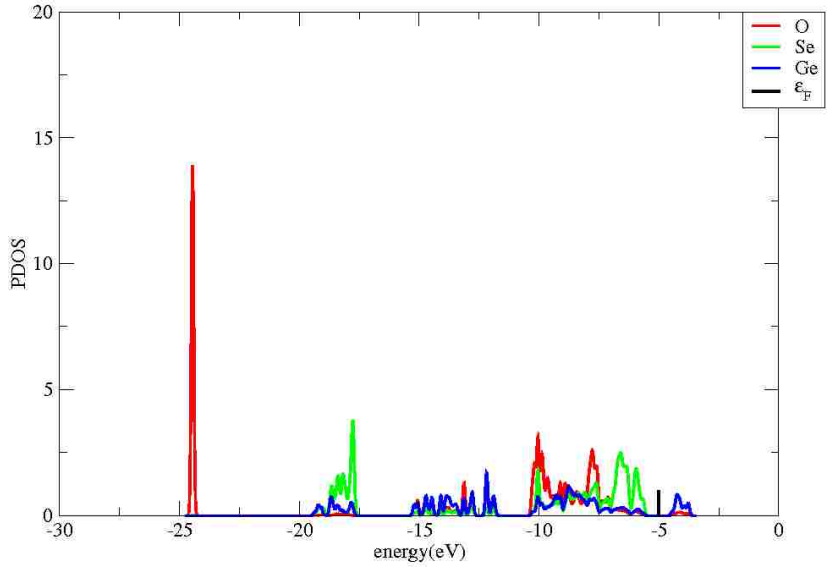

(a) Computed projected density of states.

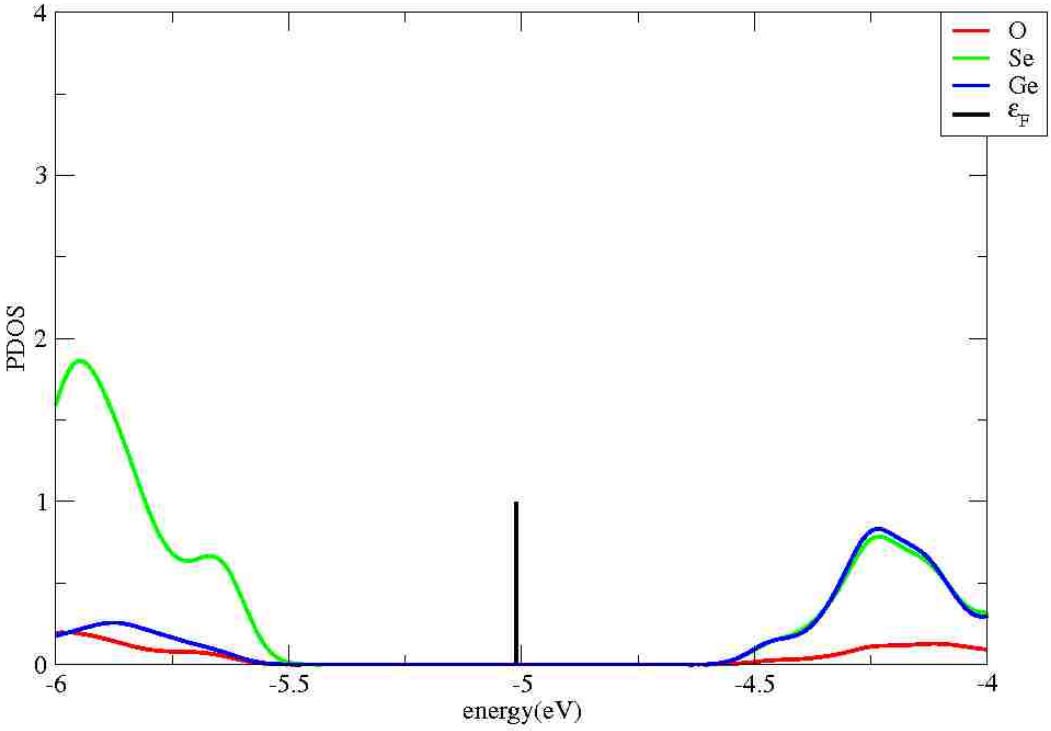

(b) Projected density of states in the band gap region.

Figure 16: Projected density of states of O_{Se} configuration. The valence band edge is at -5.45 eV, and the conduction band edge is at -4.62 eV.

Chapter 5: Silver Defects and Interactions of Silver and Oxygen Defects

5.1 Past Work and Silver Atom Defect Studies

The study of absorbed oxygen reported in Chapter 4 addressed its effects on Ge_2Se_3 used in EMB and SDC memristors. We found little changes to the Ge_2Se_3 electrical properties due to oxygen. In this chapter, we discuss the interaction of silver and atomic oxygen defects to determine interference of silver behavior in Ge_2Se_3 by atomic oxygen. First, identification of relevant silver defects is necessary. Refer to Tables 10 and 11 for all silver defects examined in this thesis and their respective designations.

Table 10: Silver defect designations. All silver defects examined and their respective figure number and designation.

Environment	Defect Type	Notes	Figure	Designation
Interlayer	Interstitial		19	$I_{Ag}^{(1)}$
Intralayer	Interstitial	Relaxed at an empty space near 4 seleniums	18	$I_{Ag}^{(2)}$
Intralayer	Interstitial	Relaxed at an empty space near 6 seleniums	20a	$I_{Ag}^{(3)}$
Intralayer	Interstitial	Relaxed at an empty space near 4 seleniums and 1 germanium	20b	$I_{Ag}^{(4)}$
Intralayer	Displacement	1 germanium, and it relaxed at a preferred interstitial location	17	Ag_{Ge}:I_{Ge}

Table 11: Silver/atomic oxygen defect designations. All silver/atomic oxygen combination defects examined and their respective figure number and designation. We used the 80-atom supercell to calculate for these defect pairings.

Pairing	Notes	Figure	Designation
$BO_{\parallel}$ with Ag_{Ge}:I_{Ge}	Same layer #1	26a	$(BO_{\parallel}$:Ag_{Ge}:$I_{Ge})^{(1)}$
$BO_{\parallel}$ with Ag_{Ge}:I_{Ge}	Same layer #2	26b	$(BO_{\parallel}$:Ag_{Ge}:$I_{Ge})^{(2)}$
$BO_{\parallel}$ with Ag_{Ge}:I_{Ge}	Same layer #3	26c	$(BO_{\parallel}$:Ag_{Ge}:$I_{Ge})^{(3)}$
$BO_{\parallel}$ with Ag_{Ge}:I_{Ge}	Different layers		$(BO_{\parallel}$:Ag_{Ge}:$I_{Ge})^{(4)}$
	1 atomic oxygen-bridging Ag-Ge	25	Ag-O-Ge
$BO_{\parallel}$ with Ag_{Ge}:I_{Ge}	Infinitely separated		$BO_{\parallel}$+Ag_{Ge}:I_{Ge}
$BO_{\parallel}$ with $I_{Ag}^{(2)}$	Same layer #1	27a	$(BO_{\parallel}$:$I_{Ag}^{(2)})^{(1)}$
$BO_{\parallel}$ with $I_{Ag}^{(2)}$	Same layer #2	27b	$(BO_{\parallel}$:$I_{Ag}^{(2)})^{(2)}$
$BO_{\parallel}$ with $I_{Ag}^{(2)}$	Same layer #3. 1 atomic oxygen occupies the original STE site, and the STE relocated to another $(Ge\text{-}Ge)_{\parallel}$	27c	$(BO_{\parallel}$:$I_{Ag}^{(2)})^{(3)}$
$BO_{\parallel}$ with $I_{Ag}^{(2)}$	Infinitely separated		$BO_{\parallel}$+$I_{Ag}^{(2)}$

5.1.1 Past Work

In Section 1.1, previous works by Edwards *et al* in Refs. [1, 16, 17] were briefly noted. We expand on these results in this section. Table 12 shows that silver has an intralayer environmental preference. With $I_{Ag}^{(A)}$ as the lowest energy configuration, Ag_{Ge}:I_{Ge} and $I_{Ag}^{(A)}$ are the two relevant configurations. Edwards reported that Ag_{Ge}:I_{Ge} has gap state and $I_{Ag}^{(A)}$ does not. In Subsection 5.1.3, we present our investigation on environmental and isolated silver defect preferences and compare them with the results in Ref. [1].

Table 12: Energies of formation of 3 defects from Ref. [1]. Note that Edwards did not use these designations in Ref. [1].

Defect	Designation	ΔE_f (eV)
Interstitial Ag Relaxed Intralayer	$I_{Ag}^{(A)}$	0.59
Interstitial Ag Relaxed Interlayer	$I_{Ag}^{(B)}$	0.81
Ag Substitutes Ge, and Ge Relaxes Interstitially	Ag_{Ge}:I_{Ge}	0.69

In Ref. [17], Edwards *et al* reported that interstitial silver atoms autoionize in Ge_2Se_3 and donate an electron to the cell. For $I_{Ag}^{(A)}$, the donated electron self-traps on a nearby $(Ge\text{-}Ge)_{\|}$ and an neighboring (to the $(Ge\text{-}Ge)_{\|}$) Ge-Se, and the STE expands $(Ge\text{-}Ge)_{\|}$ and Ge-Se bond lengths by 0.12 Å and 0.13 Å, respectively. In Ref. [16], Edwards *et al* first reported electron self-trapping in the absence of silver with charged cluster and supercell approximations.

5.1.2 Silver Defect Cell Size Convergence Study

As when we studied oxygen defects, we must also determine the minimally sufficient cell size for the silver defect studies. Table 13 shows the energies of formation of Ag_{Ge}:I_{Ge} and $I_{Ag}^{(2)}$ at the 80-atom and the 360-atom cell sizes. The energies of formation agree to 0.005 eV for both defects. The respective geometries are shown in Figures 17 and 18. Once again, we find that the 80-atom cell size is sufficient for silver atom defect studies.

To obtain the $I_{Ag}^{(2)}$ defect, we inserted the silver atom in an intralayer empty space; this and similar configurations formation are on observable timescales. After relaxation, the bond length of (Ge 1-Ge 2) of Figure 18 expanded from 2.49 Å to 2.56 Å. For details about Ag_{Ge}:I_{Ge}, see Ref. [1].

Table 13: Convergence of energies of formation of 2 silver defects for 2 different unit cell sizes.

	ΔE_f (eV)	
Defect	80-Atom	360-Atom
Ag_{Ge}:I_{Ge}	0.710	0.705
$I_{Ag}^{(2)}$	0.639	0.634

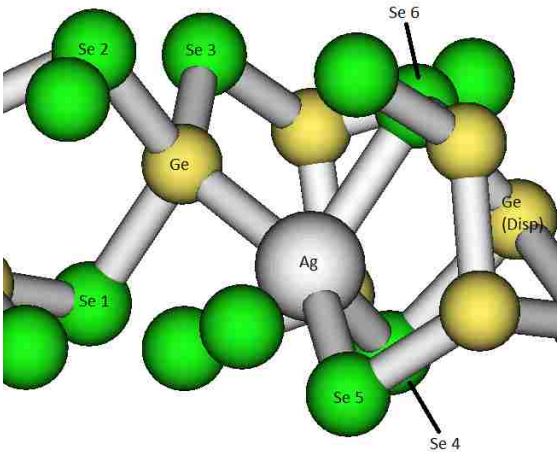

Figure 17: Relaxed geometry of Ag_{Ge}:I_{Ge}. The labeled atoms are referenced in Figures 22a and 22b. For all geometry figures, silver atoms are colored in silver.

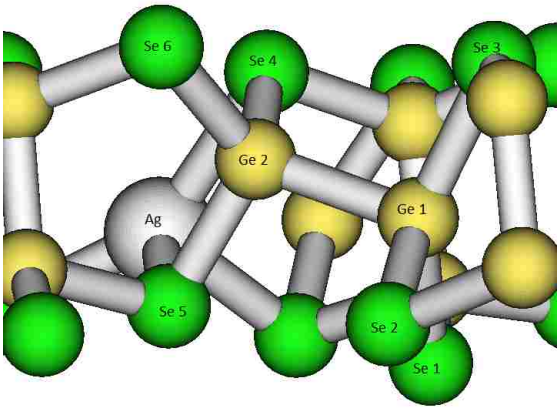

Figure 18: Relaxed geometry of $I_{Ag}{}^{(2)}$. The labeled atoms are referenced in Figures 23a and 23b.

5.1.3 Relevant Silver Defects

We studied interstitial silver and silver substituting for germanium to explore Campbell's model for dendrite growth. The sampling process resulted in four relaxed interstitial defect configurations, and the relaxed geometry of Ag_{Ge}:I_{Ge} was obtained from Edwards *et al* [1]. Table 14 shows that the energies of formation of all silver defects are positive. This is consistent with the need for an applied electric field for silver introduction into the Ge_2Se_3 layer.

Table 14: Energies of formation of interlayer and intralayer silver defect configurations. $I_{Ag}^{(1)}$ is the only interlayer configuration in this table.

Defect	ΔE_f (eV)	ΔE_f Relative to Lowest Energy Configuration (eV)
$I_{Ag}^{(1)}$	0.833	0.227
$I_{Ag}^{(2)}$	0.639	0.033
$I_{Ag}^{(3)}$	0.606	0
$I_{Ag}^{(4)}$	0.616	0.010
Ag_{Ge}:I_{Ge}	0.709	0.103

The interlayer defect configuration (shown at Figure 19) is higher in energy compared to all intralayer defect configurations; specifically, the energy of formation of $I_{Ag}^{(1)}$ is 0.227 eV higher than the lowest energy configuration. This is consistent with results of Edwards *et al* [1]; Table 12 shows a 0.22 eV preference for silver in the intralayer environment.

To obtain the $I_{Ag}^{(1)}$ defect, we placed the silver in the interlayer environment and let the configuration relax.

Finally, Table 14 shows four relevant silver defect configurations, $I_{Ag}^{(2)}$, $I_{Ag}^{(3)}$, $I_{Ag}^{(4)}$ and Ag_{Ge}:I_{Ge}. We have not calculated the activation energy for movement between any silver defects, so we cannot comment on their kinetics. $I_{Ag}^{(2)\text{ - }(4)}$ are geometrically and energetically very similar. In fact, we argue that $I_{Ag}^{(2)}$ and $I_{Ag}^{(4)}$ are metastable configurations of the $I_{Ag}^{(3)}$ defect. The Ag_{Ge}:I_{Ge} defect is the silver

displacement of a germanium, and from the perspective of the original germanium dimer, silver occupies the geramnium dimer site by displacing a germanium.

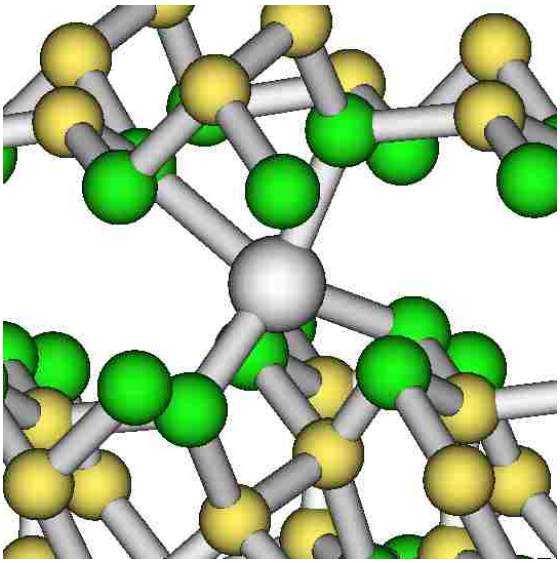

Figure 19: Relaxed geometry of $I_{Ag}^{(1)}$.

The method to obtain $I_{Ag}^{(3)}$ and $I_{Ag}^{(4)}$ defects is similar to the way to obtain $I_{Ag}^{(2)}$. We now go into some details regarding those first two intralayer silver defects. The figures show the silver is graphically connected to six seleniums (Figure 20a) and four seleniums/one germanium (Figure 20b). We calculated for the equilbrium geometry of molecular Ag_2Se, and the Ag-Se bonds are 2.46 Å. When compared to the Ag-Se distance in $I_{Ag}^{(3)}$ and $I_{Ag}^{(4)}$, the Ag_2Se Ag-Se bond is 0.38-0.6 Å and 0.29-0.47 Å shorter, respectively. The labeled atoms are referenced in Figures 21a, 21b, 24a and 24b. For $I_{Ag}^{(3)}$ and $I_{Ag}^{(4)}$, bond lengths of (Ge 1-Ge 2) respectively expanded from 2.49 to 2.61 and 2.56 Å after relaxation.

5.1.4 Projected Densities of States of Defect Configurations

We plotted the projected density of states figures in this subsection similarly to those in Subsection 4.3.3. In addition, these figures would include atoms with high

gap state peaks and/or notable atoms;[53] smaller gap state peaks have been excluded. For all projected density of states figures below, the projected densities of states of germaniums and seleniums with high gap state peaks appear in violet and dark green respectively, and silver and displaced germanium appear in silver and maroon, respectively.

Figures 21a and 21b show that the band gap of Ge_2Se_3 is unchanged by the $I_{Ag}^{(3)}$ defect. Labeled in Figure 20a, (Ge 1-Ge 2) bond length expanded by 0.12 Å, which indicates the donated electron self-trapped around the (Ge 1-Ge 2) site. Figures 22a and 22b shows that Ag_{Ge}:I_{Ge} has an 1 eV band gap. The Fermi level shifted from -4.98 eV to -4.79 eV. Figure 22b shows that the gap state localized on atoms, Ag, Ge and Se 1-6, labeled in Figure 17. The donated electron localized around the (Ag-Ge) site. These two defect configurations are in agreement with the corresponding configurations in Ref. [1].

We now discuss further details of the projected densities of states of the Ag_{Ge}:I_{Ge} defects. We note the atom correlation of gap state peak heights. From Figure 17, Ge (NN to Ag) is directly connected to Se 1,2 and 3, and their peak heights are similarly higher; Ag is directly connected to Se 4,5,6, and their peaks heights are similarly lower. The gap state localized more strongly on the germanium side rather than the silver side. We observe this pattern for many other defect configurations.

The projected densities of states of $I_{Ag}^{(2)}$ and $I_{Ag}^{(4)}$, although geometrically and energetically similar to $I_{Ag}^{(3)}$, deviate from results just mentioned in those projected densities of states. Figures 23a and 23b show that $I_{Ag}^{(2)}$ has a 1.04 eV band gap, which significantly differs from the band gap of $I_{Ag}^{(3)}$. The Fermi level shifted to -4.55 eV. Figure 23b shows that the gap state localized around the (Ge 1-Ge 2) site labeled in Figure 18. The bond length of (Ge 1-Ge 2) expanded by 0.07 Å; this is somewhat consistent with Ref. [17], and the reported characteristics still indicates

[53] These are the intrinsic and extrinsic defects.

STE. In Figures 24a and 24b, we see a 1.02 eV band gap; again, this differs from the band gap of $I_{Ag}^{(3)}$. The Fermi level shifted to -4.49. Figure 24b shows that the gap state localized around the (Ge 1-Ge 2) site labeled in Figure 20b. The bond length of (Ge 1-Ge 2) expanded by 0.7 Å.

From the projected density of states figures of relevant silver defect configurations, we conclude that the presence of silver in Ge_2Se_3 does not alter its band gap, but silver defects does introduce gap state.

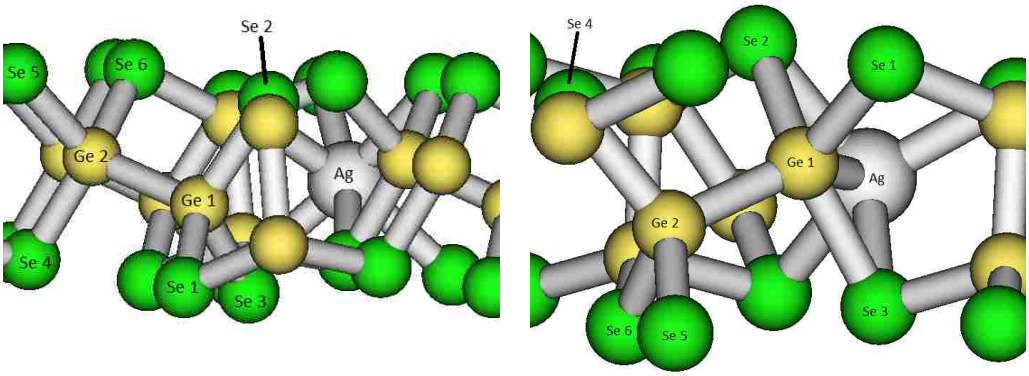

(a) Relaxed geometry of $I_{Ag}^{(3)}$. (b) Relaxed geometry of $I_{Ag}^{(4)}$.

Figure 20: Relaxed geometries of intralayer silver interstitial configurations. For the $I_{Ag}^{(3)}$ configuration, the Ag-Se bond lengths range from 2.84 Å to 3.06 Å. For the $I_{Ag}^{(4)}$ configuration, The Ag-Se bond lengths range from 2.75 Å to 2.93 Å.

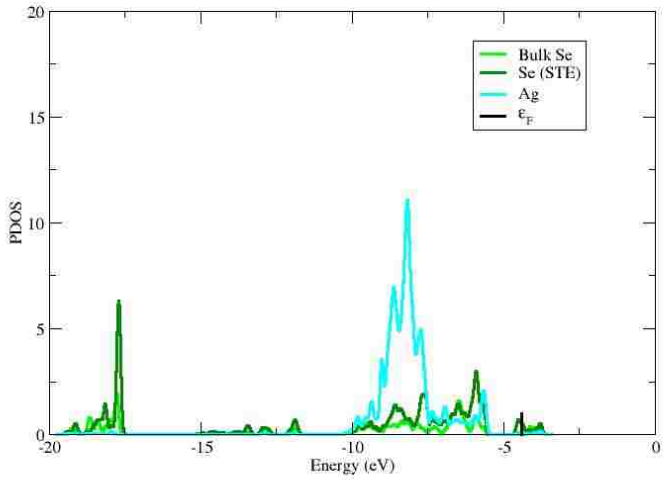

(a) Computed projected density of states.

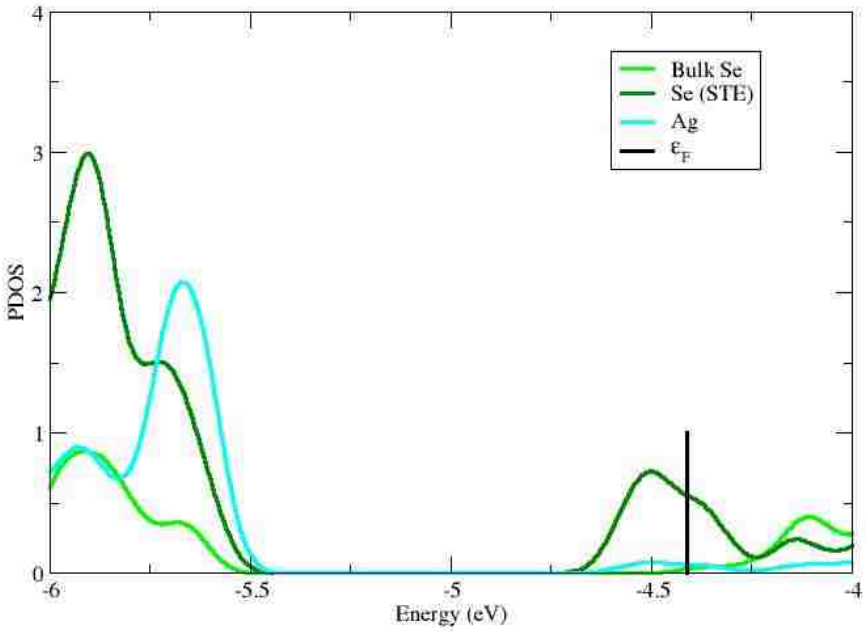

(b) Projected density of states in the band gap region.

Figure 21: Projected density of states of $I_{Ag}^{(3)}$ configuration, see Figure 20a. Bulk Se labeled are seleium states from the host crystal. Se (STE) labeled are states of the selenium at the STE site; this defines the gap state location, roughly -4.5 eV.

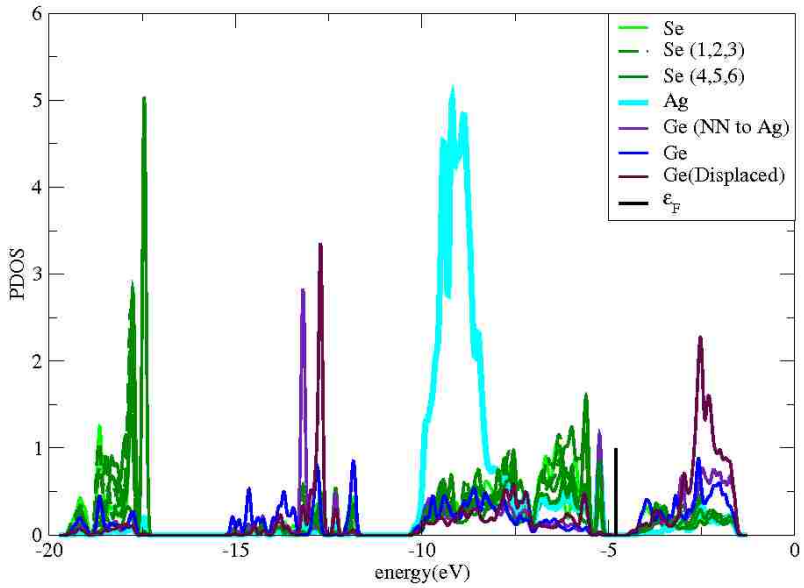

(a) Computed projected density of states.

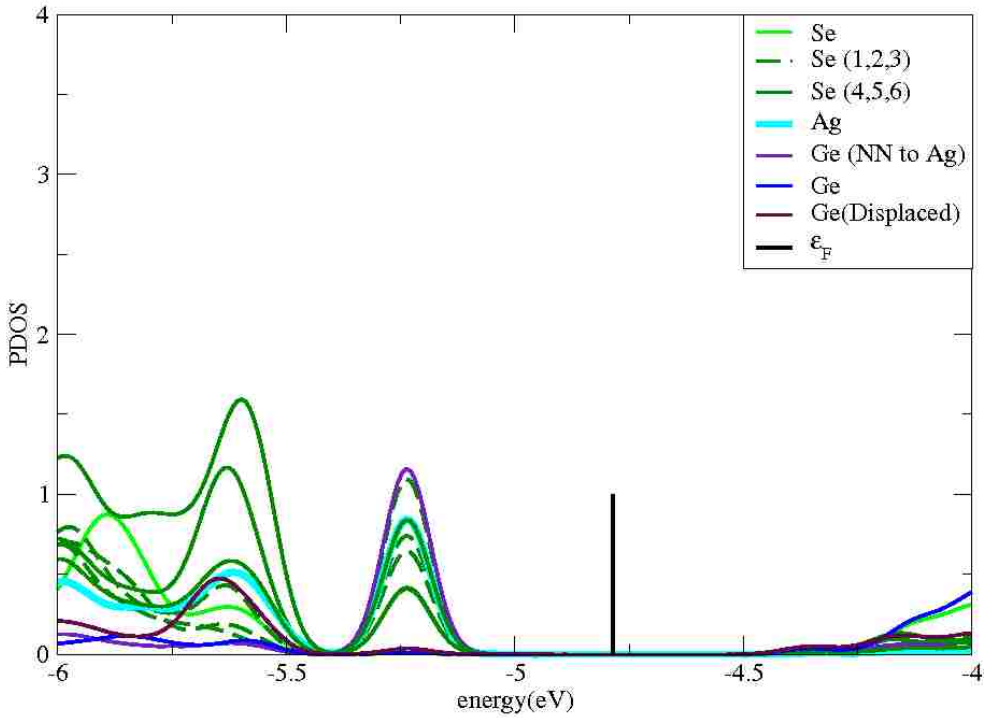

(b) Projected density of states in the band gap region.

Figure 22: Projected density of states of Ag_{Ge}:I_{Ge} configuration, see Figure 17. The valence band edge is at -5.44 eV and the conduction band edge is at -4.44 eV. The middle of the gap state peaks is at -5.23 eV.

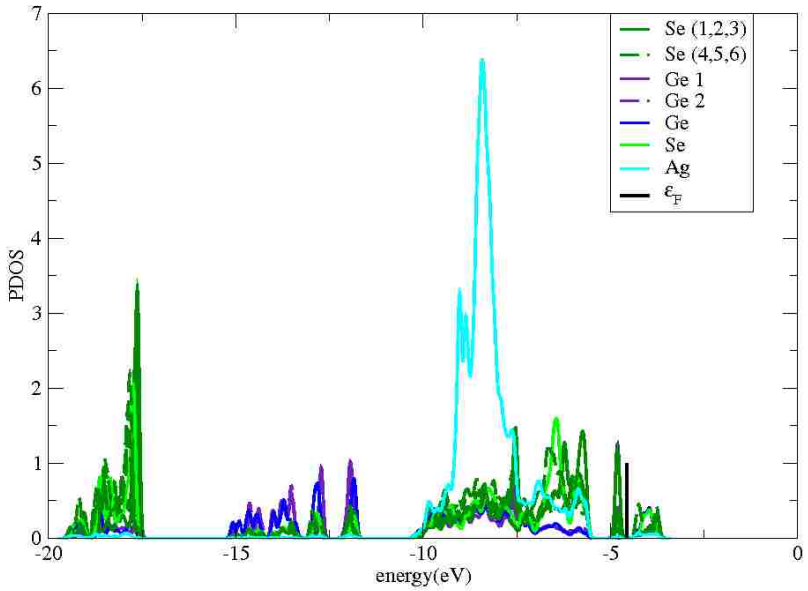

(a) Computed projected density of states.

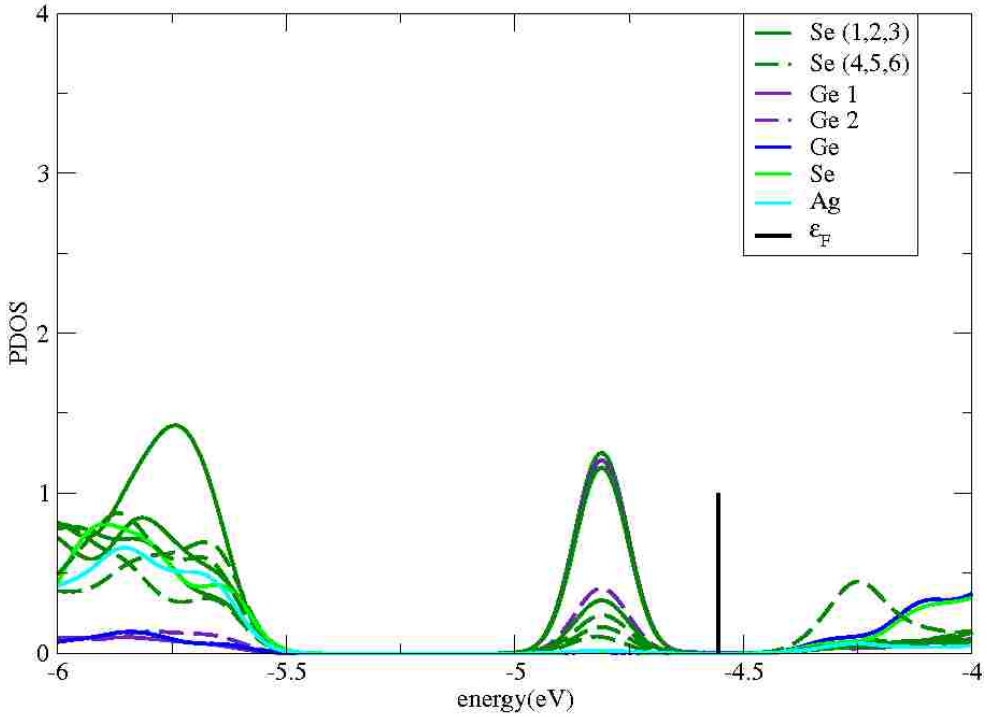

(b) Projected density of states of $I_{Ag}{}^{(2)}$ configuration in the band gap region.

Figure 23: Projected density of states of $I_{Ag}{}^{(2)}$ configuration, see Figure 18. The valence band edge is at -5.44 eV and the conduction band edge is at -4.40 eV. The middle of the gap state peaks is at -4.81 eV.

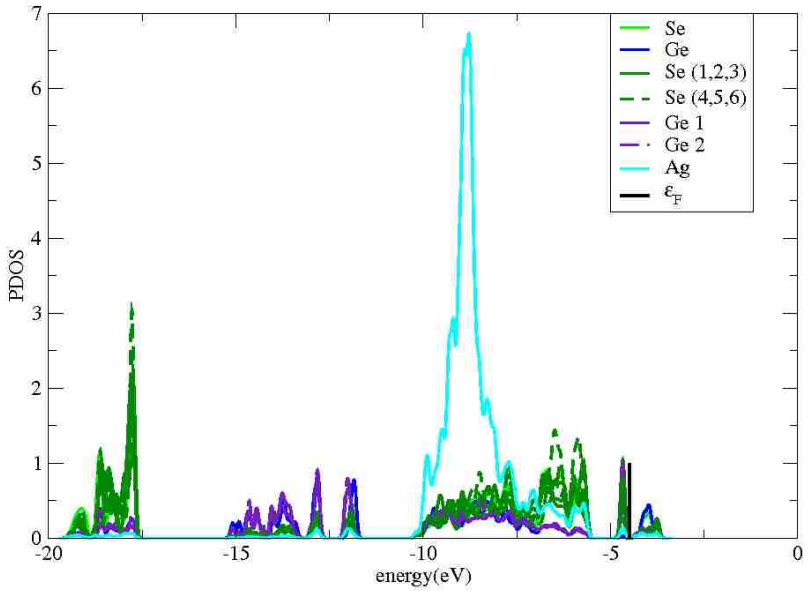

(a) Computed projected density of states.

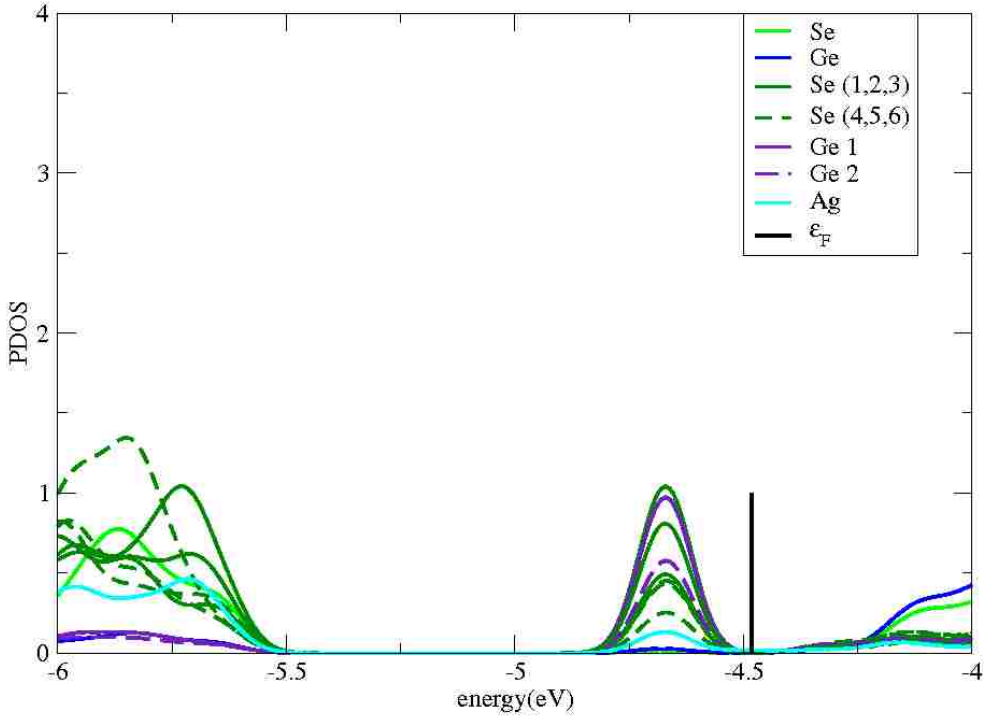

(b) Projected density of states in the band gap region.

Figure 24: Projected density of states of $I_{Ag}^{(4)}$ configuration, see Figure 20b. The valence band edge is at -5.45 eV and the conduction band edge is at -4.43 eV. The middle of gap state peaks is at -4.67 eV.

5.2 Silver and Atomic Oxygen Defect Interactions

In the previous section, we confirmed and added to silver defect results by Edwards *et al* [1, 17]. We now examine the interaction of silver and oxygen defects. The relevant silver and oxygen defects guide the sampling process. After determining the most energetically favored ways for silver and oxygen defects to interact, projected density of states analysis reveals any changes to band edges, band gaps, presence of gap/localized states and shifts of gap/localized states.

5.2.1 Relevant Silver and Atomic Oxygen Defect Interactions

This study paired the relevant silver defects, $I_{Ag}^{(2)}$ and Ag_{Ge}:I_{Ge}, with the only relevant oxygen defect, $BO_{\parallel}$. $I_{Ag}^{(2)}$ is typical of all intralayer silver interstitials. Similarly, Ag_{Ge}:I_{Ge} is an average representation of an intralayer silver displacement of germanium. For each silver defect configuration, we inserted atomic oxygen at several equivalent $(Ge\text{-}Ge)_{\parallel}$ sites, where they would normally form $BO_{\parallel}$. This allowed us to study the interaction of these silver and atomic oxygen defects as a function of their separation distance.

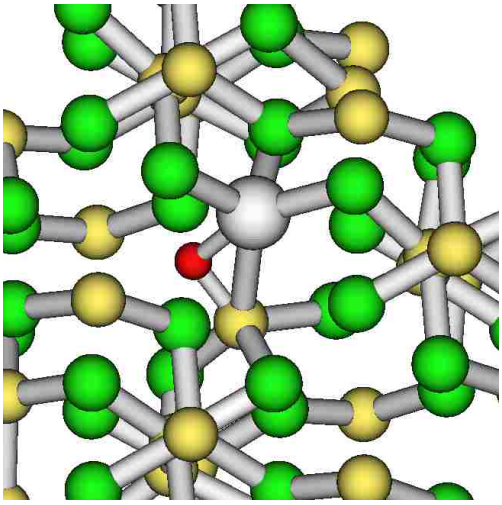

Figure 25: Relaxed geometry of Ag-O-Ge. Before oxygen bridging, the Ag-Ge bond length is 2.55 Å; after oxygen bridging, the Ag-Ge distance is 3.02 Å.

In the study of pairing atomic oxygen with Ag_{Ge}:I_{Ge}, we also bridged Ag-Ge with atomic oxygen. The equilibrium geometry is shown in Figure 25. Note that after the atomic oxygen spontaneously bridged the Ag-Ge bond, the its length increased by 0.47 Å; the bond is dramatically weaken. We now go into further details regarding the $BO_{\parallel}$:Ag_{Ge}:I_{Ge} pairings and their respective geometry figures. We selected nearby $(Ge\text{-}Ge)_{\parallel}$ sites in the same layer as the Ag_{Ge}:I_{Ge}. The labeled atoms are referenced in Figures 28a, 28b, 30a, 30b, 31a and 31b. In Figure 26a, $BO_{\parallel}$ and its specific location caused significant rearrangement on the local geometry of $(BO_{\parallel}Ag_{Ge}{:}I_{Ge})^{(1)}$ around Ag-Ge; this led to further energy reduction (see Table 15). In Figure 26b, there is no significant geometric rearrangement, but additional energy reduction suggests the silver and atomic oxygen defects interacted. In Figure 26c, there is little geometric rearrangement and energy minimization. The top half of Table 15 summarizes the results for these five pairings and an infinitely separated pair.

Table 15: Energies of formation of silver/atomic oxygen defect combination configurations. We used the comparisons to infinite separation and separation distance of silver and oxygen to study the interaction of defects and interaction range.

	ΔE_f (eV)	ΔE_f Relative to Lowest Energy Configuration (eV)	ΔE_f Relative to the Defect's Respective Infinite Separation Limit (eV)	Ag and O Separation Distance (Å)
$(BO_{\parallel}{:}Ag_{Ge}{:}I_{Ge})^{(1)}$	-1.640	0	-0.198	6.82
$(BO_{\parallel}{:}Ag_{Ge}{:}I_{Ge})^{(2)}$	-1.563	0.077	-0.121	6.23
$(BO_{\parallel}{:}Ag_{Ge}{:}I_{Ge})^{(3)}$	-1.450	0.190	-0.008	7.46
$(BO_{\parallel}{:}Ag_{Ge}{:}I_{Ge})^{(4)}$	-1.462	0.178	-0.020	8.45
Ag-O-Ge	-0.321	1.319	1.121	2.15
$BO_{\parallel}$+Ag_{Ge}:I_{Ge}	-1.442	0.198	0	∞
$(BO_{\parallel}{:}I_{Ag}{}^{(2)})^{(1)}$	-1.417	0.223	0.094	4.34
$(BO_{\parallel}{:}I_{Ag}{}^{(2)})^{(2)}$	-1.522	0.118	-0.011	5.22
$(BO_{\parallel}{:}I_{Ag}{}^{(2)})^{(3)}$	-1.544	0.096	-0.033	5.10
$BO_{\parallel}$+$I_{Ag}{}^{(2)}$	-1.511	0.129	0	∞

For separations $\leq$ 6.82 Å, the two defects (shown in Figures 26a and 26b) are weakly attracted. For separation around 7 Å, the attraction between these two defects (shown in Figure 26c), sharply drops off. The relatively high energy of formation of Ag-O-Ge indicates this configuration is very unlikely.

Before reporting the results for $BO_{\|}$:$I_{Ag}{}^{(2)}$ pairing, we first discuss further details regarding obtaining the pairings and their respective geometry figures. We selected nearby $(Ge\text{-}Ge)_{\|}$ sites in the same layer as the $I_{Ag}{}^{(2)}$. The labeled atoms are referenced in Figures 29a, 29b, 32a, 32b, 33a and 33b. We observe no significant geometric rearrangement for this pairing. For $(BO_{\|}$:$I_{Ag}{}^{(2)})^{(1)}$, the silver and atomic oxygen separation is the shortest, and the two foreign atoms interacted unfavorably (see Table 15). In Figures 27a and 27c, the bond lengths of (Ge 1-Ge 2) respectively expanded from 2.49 to 2.59 and 2.64 Å after relaxation. In $(BO_{\|}$:$I_{Ag}{}^{(2)})^{(3)}$, the atomic oxygen ejected the STE site to another $(Ge\text{-}Ge)_{\|}$. In $(BO_{\|}$:$I_{Ag}{}^{(2)})^{(2)}$ (shown at Figure 27b), the bond length of (Ge 1-Ge 2) expanded from 2.49 to only 2.52 Å after relaxation.

The bottom half of Table 15 summarizes results for three pairings of atomic oxygen with $I_{Ag}{}^{(2)}$ and an infinitely separated pair. At separation of 4.34 Å, the two defects (shown in Figure 27a) are weakly repulsive. At separations around 5 Å, the repulsion between these two defects (shown in Figures 27b and 27c) sharply drops off. The apparent attraction beyond 5 Å separation is insignificant.

Once an Ag-Ge bond forms, even a mobile oxygen atom will not disrupt that bond. We now consider the converse, i.e. whether a silver atom can disrupt a Ge-O-Ge bridge to form Ag-Ge bond. Considering the thermodynamics, we note the Ge-O bond is much stronger than the Ge-Ge bond, and silver disruption of Ge-O-Ge must involve breaking a Ge-O bond. 0.7 eV is required for breaking a Ge-Ge bond [94], and we expect the activation energy of Ag disruption of Ge-O-Ge to be significantly larger. Without performing an NEB transition state calculation, this process, with Ag-O-Ge as an intermediate state, would have a minimum activation energy of 1.32

eV, which corresponds to timescales on the order of tens of days. Without additional calculations, we do not know the timescale of this process more accurately. We conclude that ejection of atomic oxygen from a Ge-O-Ge bridge by silver is unlikely. Conversely, atomic oxygen cannot eject silver from a silver-germanium dimer because it is immobile.

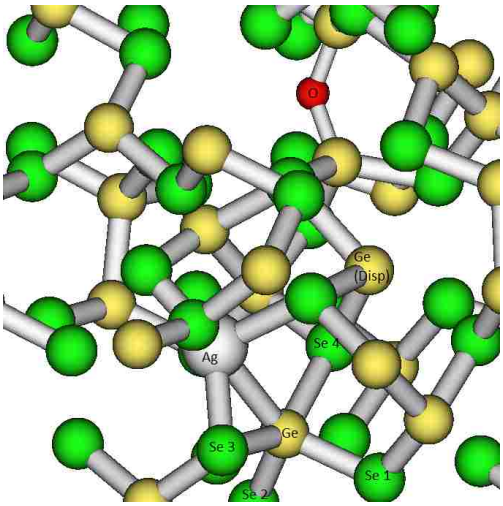

(a) Relaxed geometry of $(BO_{\|}{:}Ag_{Ge}{:}I_{Ge})^{(1)}$.

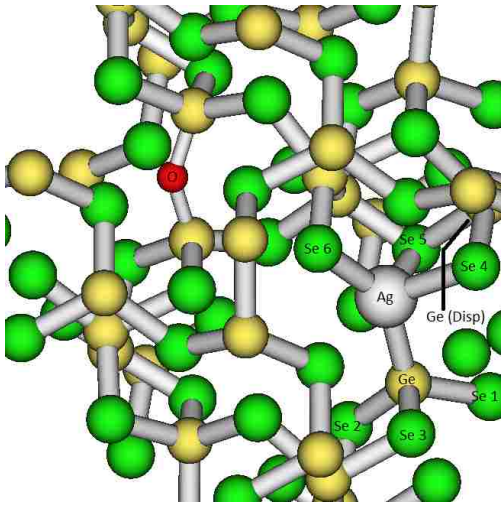

(b) Relaxed geometry of $(BO_{\|}{:}Ag_{Ge}{:}I_{Ge})^{(2)}$.

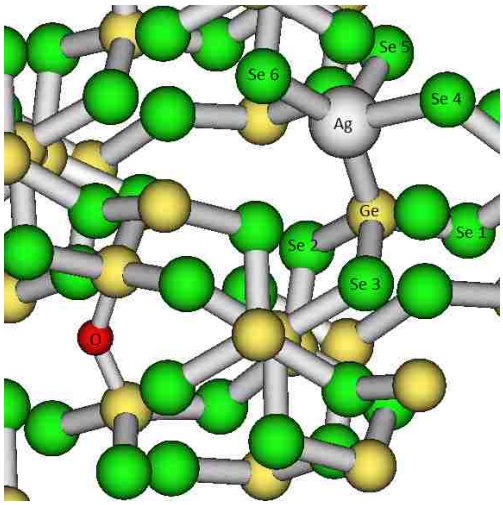

(c) Relaxed geometry of $(BO_{\|}{:}Ag_{Ge}{:}I_{Ge})^{(3)}$.

Figure 26: Relaxed geometries of $(BO_{\|}{:}Ag_{Ge}{:}I_{Ge})$ pairings. For the $(BO_{\|}{:}Ag_{Ge}{:}I_{Ge})^{(1)}$ configuration, the Ag-Se 3 bond length is 2.61 Å. The Ge-Se 3 bond length is 2.73 Å. The Ag-Ge bond length is 2.98 Å.

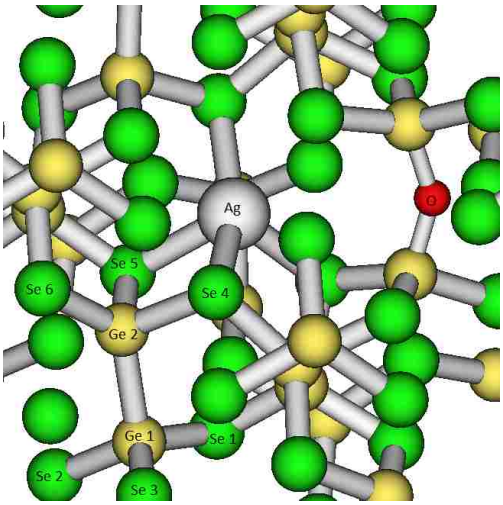

(a) Relaxed geometry of $(BO_{\|}{:}I_{Ag}{}^{(2)})^{(1)}$.

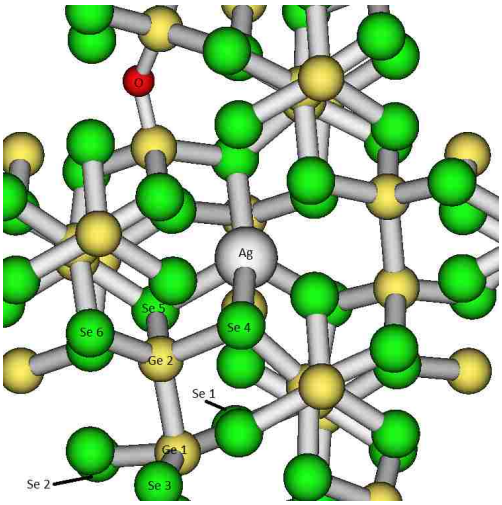

(b) Relaxed geometry of $(BO_{\|}{:}I_{Ag}{}^{(2)})^{(2)}$.

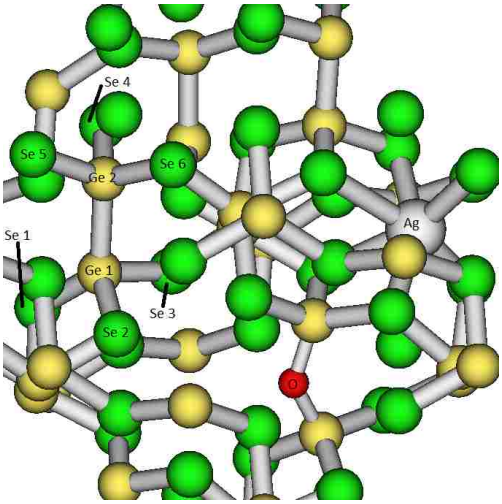

(c) Relaxed geometry of $(BO_{\|}{:}I_{Ag}{}^{(2)})^{(3)}$.

Figure 27: Relaxed geometries of $(BO_{\|}{:}I_{Ag}{}^{(2)})$ pairings.

5.2.2 Projected Densities of States of Silver and atomic oxygen Defect Combinations

The projected density of states of $(BO_{\|}{:}Ag_{Ge}{:}I_{Ge})^{(1)}$ (shown at Figures 28a and 28b) exhibits a band gap of 1.02 eV and gap state with energy at -4.50 eV. Figure 28b shows that the gap state localized on the atoms, Ge, Se 1, Se 2, Se 3 and Se 4, labeled in Figure 26a. Originally, the Ag was not bonded to the Se 3, and the Ge

was not bonded to Se 4. This introduction of the $BO_{\|}$ caused significant geometry rearrangement. Seemingly, Se 3 bonded with Ag and became 3-fold coordinated, and the Ag remained 4-fold coordinated Se 4 bonded with Ge, and the Ge became 5-fold coordinated. The Ag-Se 3 bond length is Figure 28b shows that the gap state contribution of silver and two of its nearest neighbor seleniums diminished compared to the isolated Ag_{Ge}:I_{Ge} configuration, while the gap state is still localized. When compared to Ag_{Ge}:I_{Ge}, the band edges and band gap changed minimally, and the gap state energy shifted from -5.23 to -5.14 eV. Note that the localized states did not shift out of the band gap.

The projected density of states of $(BO_{\|}$:$I_{Ag}{}^{(2)})^{(1)}$ (shown at Figures 29a and 29b) exhibits a band gap of 1.01 eV and gap state with energy at -4.65 eV. The densities of states of Ge 1 and Ge 2 remain correlated with their respective nearest neighbor selenium atoms compared to the $I_{Ag}{}^{(2)}$ configuration. Figure 29b shows that the gap state localized on atoms, Ge 1, Ge 2 and Se 1-6, labeled in Figure 27a. When compared to $I_{Ag}{}^{(2)}$, the band edges and band gap changed minimally, and the gap state energy shifted from -4.81 to -4.65 eV. Again the localized state did not shift out of the band gap.

In Table 16, we see minimal or no changes to band edges and band gap of silver defects due to atomic oxygen defects. Certain gap state energy shifts were significant, but no silver/atomic oxygen defect combination results in localized states shifting out of the band gap; we have no evidence of atomic oxygen drastically changing the electrical behavior of silver defects in Ge_2Se_3.

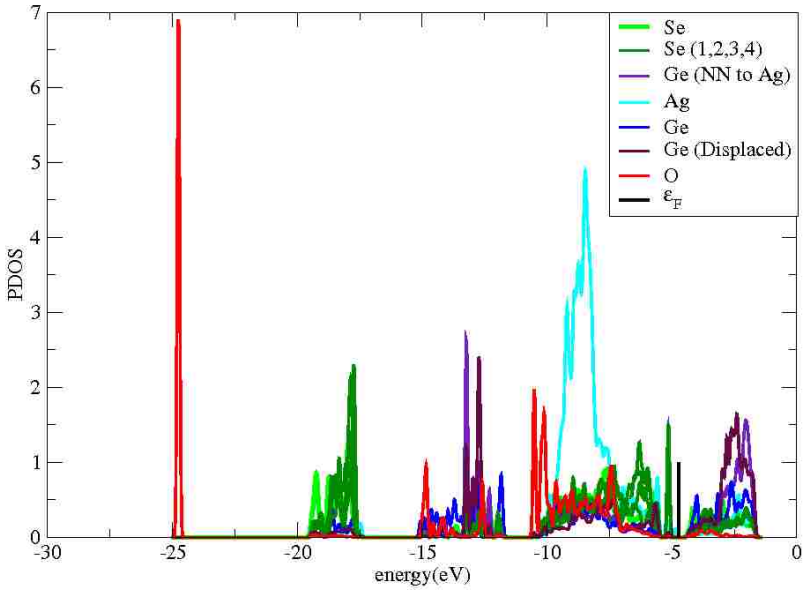

(a) Computed projected density of states.

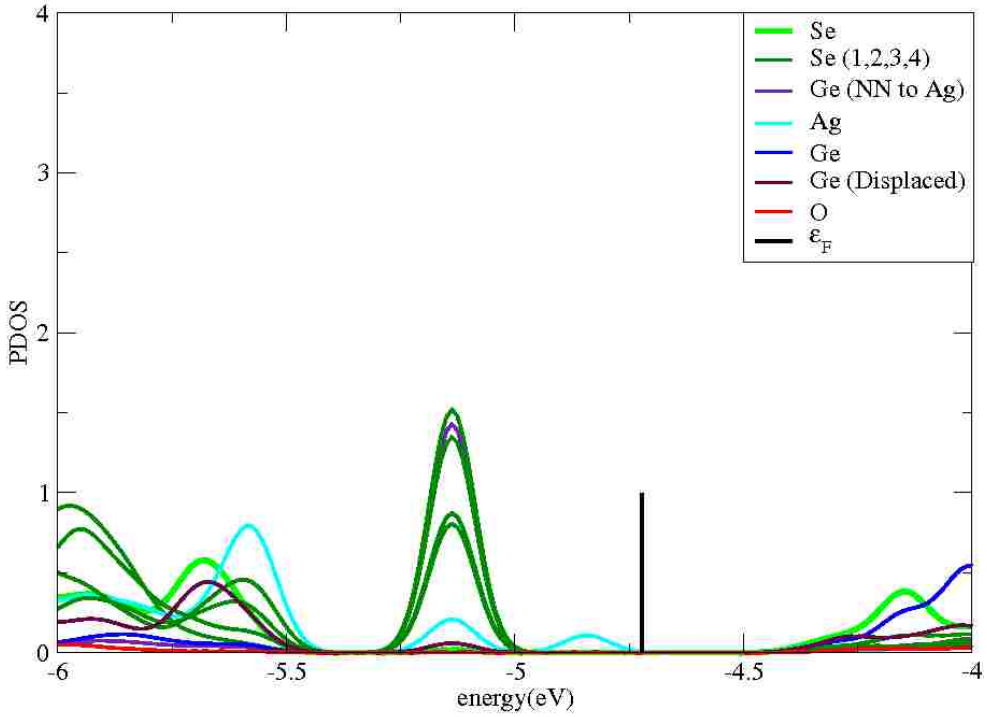

(b) Projected density of states in the band gap region.

Figure 28: Projected density of states of $(BO_{\parallel}{:}Ag_{Ge}{:}I_{Ge})^{(1)}$ configuration, see Figure 26a. The valence band edge is at -5.42 eV and the conduction band edge is at -4.50 eV. The gap state energy is -5.14 eV.

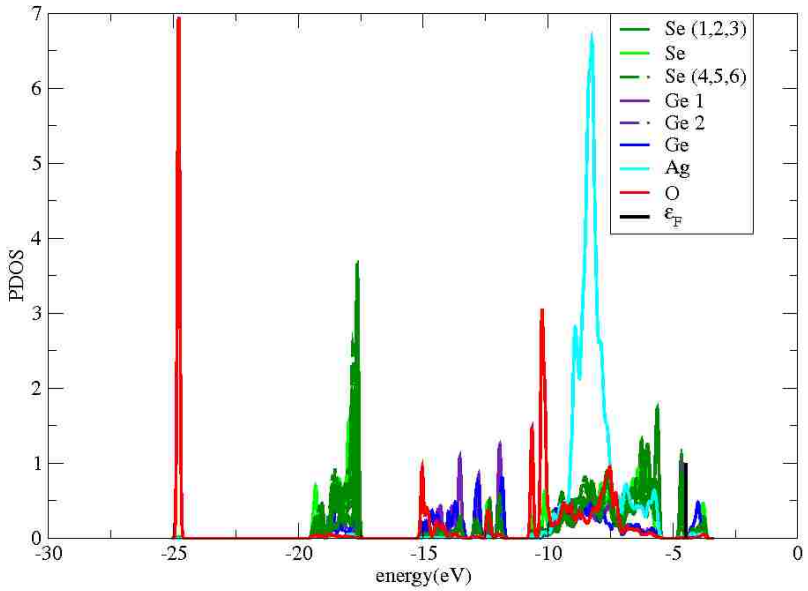

(a) Computed projected density of states.

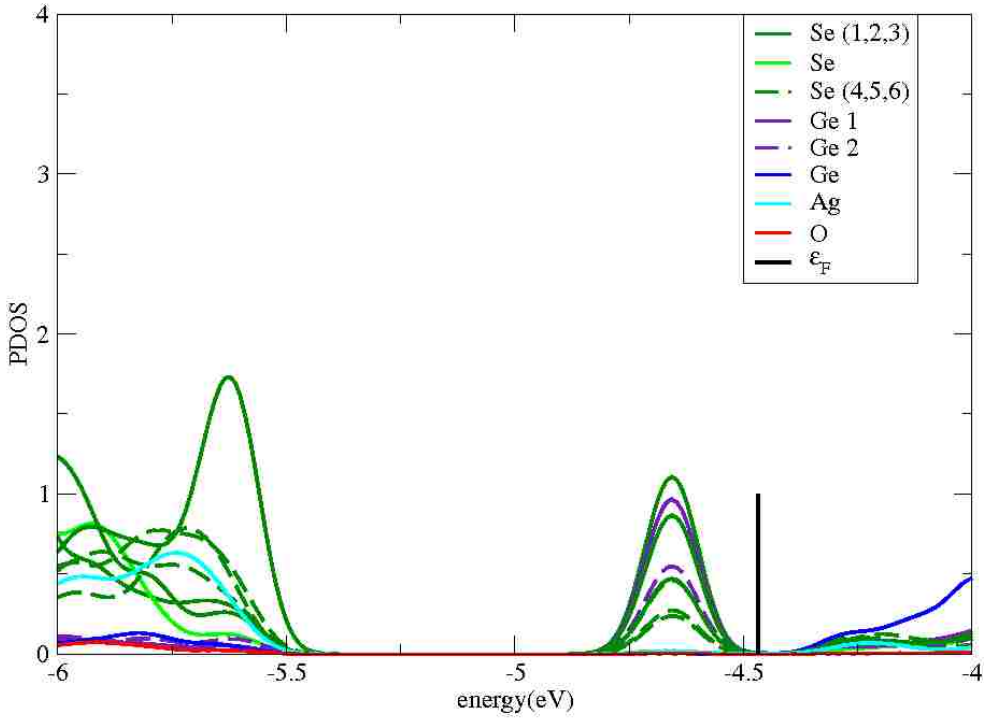

(b) Projected density of states in the band gap region.

Figure 29: Projected density of states of $(BO_{\parallel}{:}I_{Ag}{}^{(2)})^{(1)}$ configuration, see Figure 27a. The valence band edge is at -5.43 eV and the conduction band edge is at -4.42 eV. The gap state energy is -4.65 eV.

Table 16: Projected density of states results for silver/atomic oxygen defect combination configurations.

Defect Combination	Valence Band Edge (eV)	Conduction Band Edge (eV)	Band Gap (eV)	Electron Localization?	Gap State Energy (eV)
Ag_{Ge}:I_{Ge}	-5.44	-4.44	1.00	on Ag-Ge	-5.23
$(BO_{\parallel}$:Ag_{Ge}:$I_{Ge})^{(1)}$	-5.42	-4.50	0.92	on Ag NN Ge	-5.14
$(BO_{\parallel}$:Ag_{Ge}:$I_{Ge})^{(2)}$	-5.40	-4.45	0.95	on Ag-Ge	-5.24
$(BO_{\parallel}$:Ag_{Ge}:$I_{Ge})^{(3)}$	-5.43	-4.23	1.2	on Ag-Ge	-5.26
$I_{Ag}{}^{(2)}$	-5.44	-4.40	1.04	STE on Ge 1-Ge 2	-4.81
$(BO_{\parallel}$:$I_{Ag}{}^{(2)})^{(1)}$	-5.43	-4.42	1.01	STE on Ge 1-Ge 2	-4.65
$(BO_{\parallel}$:$I_{Ag}{}^{(2)})^{(2)}$	-5.41	-4.49	0.92	STE on Ge 1-Ge 2	-4.98
$(BO_{\parallel}$:$I_{Ag}{}^{(2)})^{(3)}$	-5.44	-4.41	1.03	STE on Ge 1-Ge 2	-4.65

Chapter 6: Conclusion and Future Work

6.1 Conclusion

The results in Chapters 4 and 5 demonstrated minimal impacts of oxygen defects on Ge_2Se_3 and on silver defects in Ge_2Se_3. We now summarize these results and discuss them in further detail in the context of the EMB device. In Subsection 4.2.3, thermodynamic and kinetic results showed that O_2 will dissociate after traveling toward dense environments of Ge_2Se_3 or upon absorption. In Subsection 4.3.1, we studied three intralayer atomic oxygen defects, $BO_\perp$, $BO_\parallel$ and O_{Se}, which are the three dominant oxygen defects. The atomic oxygen-bridging germanium dimer defect type, represented by $BO_\perp$ and $BO_\parallel$, are energetically favored over the other types.

We studied oxygen clustering using an NEB calculation with $BO_\perp$ and $BO_\parallel$ as the two end points in Subsection 4.3.2 and found that clustering does not occur, because oxygen atoms are immobile in Ge_2Se_3. The oxygen study then concluded with the projected density of states of the relevant defects in Subsection 4.3.3. Projected densities of states of the three dominant defects showed no gap state or significant change to the band gap of Ge_2Se_3.

In Subsection 5.1.3, we reported that silver, like oxygen, has an intralayer preference. In Subsection 5.1.4, projected densities of states of the two relevant defect types, silver displacing germanium and silver interstitial, showed no significant change to band gap for all defect configurations included. Although we did observe shift of Fermi levels and introduction of gap state in both the silver defect types.

Finally, in Section 5.2, we discussed the interaction of silver defects with oxygen defects. Due to the short interaction range, there is limited attraction or repulsion

between silver and oxygen. The Ag_{Ge}:I_{Ge} and $BO_{Ge\text{-}Ge}$ defect formations are competitive processes and operate on first-come, first-served basis. Ag ejecting (Ge-O-Ge) is kinetically unlikely; atomic oxygen ejecting (Ag-Ge) is kinetically impossible. We note that atomic oxygen bridging the Ag-Ge bond, while thermodynamically unlikely, results in Ag-O-Ge and dramatically weakens the Ag-Ge bond. Examination of projected densities of states showed again no significant change to the band gap. The presence of silver's gap state did not change due to oxygen.

We concluded earlier that the atomic oxygen-bridging germanium dimer defect type is the only relevant type barring high oxygen density in the material. Nevertheless, as reported by Campbell [84], Ge_2Se_3 made by sputtering deposition can have oxygen atom percentage as high as 5%. High oxygen density and Ge-Ge dimer saturation is unlikely but possible. However, under the reported circumstances, germanium dimers of the system could have been at least locally saturated. We mentioned that oxygen will not cluster in Ge_2Se_3, because they are immobile in the material. However, oxygen defects formed after fabrication will accumulate near the electrolyte layer edges and lead to local saturation, which can prevent local (Ag-Ge) structure formation and inhibit device function.

Finally, we are convinced that oxygen cannot disrupt EMB or SDC memristors operations by directly changing the electrical properties of Ge_2Se_3 or by changing interaction of silver with Ge_2Se_3. However, oxygen, immobile in Ge_2Se_3, can accumulate near the electrolyte layer edges if they enter into the material after fabrication. This can disrupt device operation by interfering with dendrite formation through forming Ge-O-Ge bridges.

6.2 Future Work

While our studies have been extensive, certain aspects remain to be studied. We therefore close this thesis with suggestions for future work. The results we have presented do not provide information on defect configuration preferences in Ge_2Se_3 at other Fermi levels; the Fermi level of a semiconductor can be shifted through doping [90]. We should perform calculations of varying charge states to determine the energies of formation as a function of the Fermi level for oxygen, silver defects and silver/oxygen combination defects. We were unable to perform the necessary charge calculations due to time constraints.

To definitively investigate O_2 dissociation in Ge_2Se_3, we need to perform one additional NEB transition state calculation. The goal is to determine the activation energy for O_2 to travel into the denser environment of Ge_2Se_3 while staying intact. A possible approach is to determine the activation energy for a peroxide linkage formed at the surface of a layer to transition into the peroixde linkage in the intralayer environment. We have shown in Subsection 4.2.3 that an intralayer peroxide linkage will dissociate. The remaining question is the kinetics of O_2 motion into the intralayer environment.

To definitively characterize the motion of silver, we need to perform additional NEB transition state calculations between stable locations of silver in the material. The first of two calculations would determine the activation energy, $E_a(\mathrm{Ag_{Ge}}{:}\mathrm{I_{Ge}})$, for silver to displace germanium, and the second would determine the activation energy, E_a(Ag ejects O), for silver to displace germanium and eject oxygen. $E_a(\mathrm{Ag_{Ge}}{:}\mathrm{I_{Ge}})$ addresses whether the defect configuration can be observed on typical experimental timescales. The kinetics of $\mathrm{Ag_{Ge}}{:}\mathrm{I_{Ge}}$ formation is crucial due to the mentioned notion that permanent (Ag-Ge) is the reason for consistent write/erase processes in EMB or SDC memristors that utilizes Ge_2Se_3 [13, 14, 15]. E_a(Ag ejects O) addresses convincingly if silver ejection of oxygen occupation is possible. Oxygen can only disrupt

EMB or SDC memristor operations by occupying germanium dimers before silver can displace a germanium atom. If silver can eject oxygen occupation of germanium dimers, then oxygen would not disrupt EMB or SDC memristor operations at all. NEB calculations are moderately difficult to complete; we recommend calculating for tin-assisted reactions to obtain $E_a(\mathrm{Ag_{Ge}}{:}\mathrm{I_{Ge}})$ and E_a(Ag ejects O).

Appendices

A.1 Harmonic Oscillator Approximation to Attempt to Escape Frequency

We consider nuclei in a solid to be classical particles under the influence of harmonic potentials near their relaxed geometry positions. The force constant, k, is related to the angular oscillation frequency, ω, and oscillation frequency, f, by Eq. 22,

$$\omega = 2\pi f = \sqrt{\frac{k}{m_a^{(N)}}} \tag{22}$$

We approximate the energy change from relaxed geometry to the nearest transition state geometry, ΔE, by Eq. 23,

$$\Delta E = \frac{1}{2}k\left(\sum_a (\Delta d)_a^2\right) \tag{23}$$

Here, $\left(\sum_a (\Delta d)_a^2\right)$ is the square of all nuclei displacement from their relaxed geometry positions.

In this thesis, two transition state studies using the NEB method determined kinetic barriers relevant to oxygen(O_2) dissociation and atomic oxygen movement in Ge_2Se_3. We approximate the order of magnitude attempt to escape frequency by using the second transition state study; the transition state path energies can be seen at Figure 12. We used the mass of oxygen atom for $m_a^{(N)}$, because atomic oxygen is the lightest element in the unit cell; this results in an upper bound. We compute $\left(\sum_a (\Delta d)_a^2\right)$ by using the displacement of all 81 atoms in the cell. ΔE is 0.127 eV. With these values, f is 2.98×10^{13} Hz. Alternatively, inferred vibrational spectra of

$GeSe_2$ in Ref. [95] show that the entire absorption range (for all modes and elements) is 400-1200 number of waves/cm. The corresponding frequency range is 1.9×10^{12}-5.7×10^{12} Hz.

A.2 Remaining Projected Densities of States of Silver and Atomic Oxygen Defect Combinations

Figures 30b, 31b, 32b and 33b display the missing details complied in Table 16. As before, no silver/atomic oxygen defect combination results in localized states shifting out of the band gap.

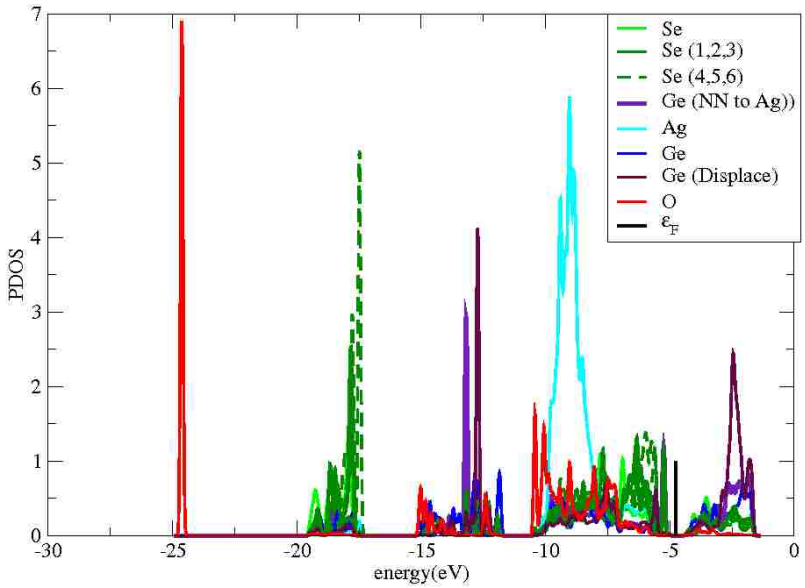

(a) Computed projected density of states.

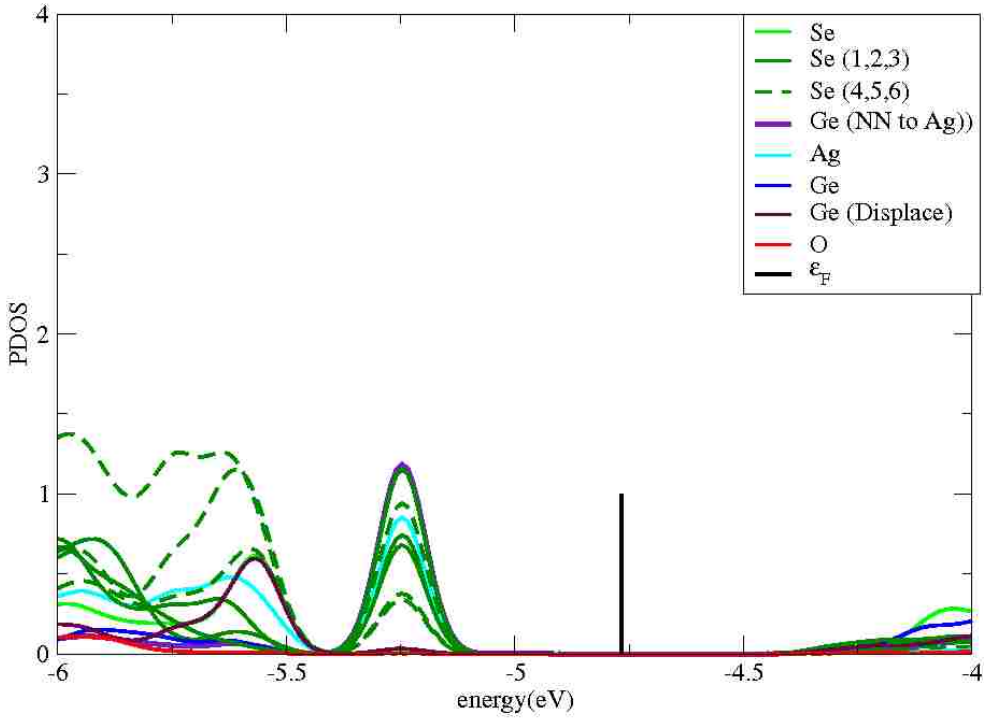

(b) Projected density of states in the band gap region.

Figure 30: Projected density of states of $(BO_{\parallel}{:}Ag_{Ge}{:}I_{Ge})^{(2)}$ configuration, see Figure 26b. The valence band edge is at -5.40 eV and the conduction band edge is at -4.45 eV. The gap state energy is -5.24 eV. The projected densities of states of silver and connected germanium are correlated with their respective nearest neighbor selenium atoms.

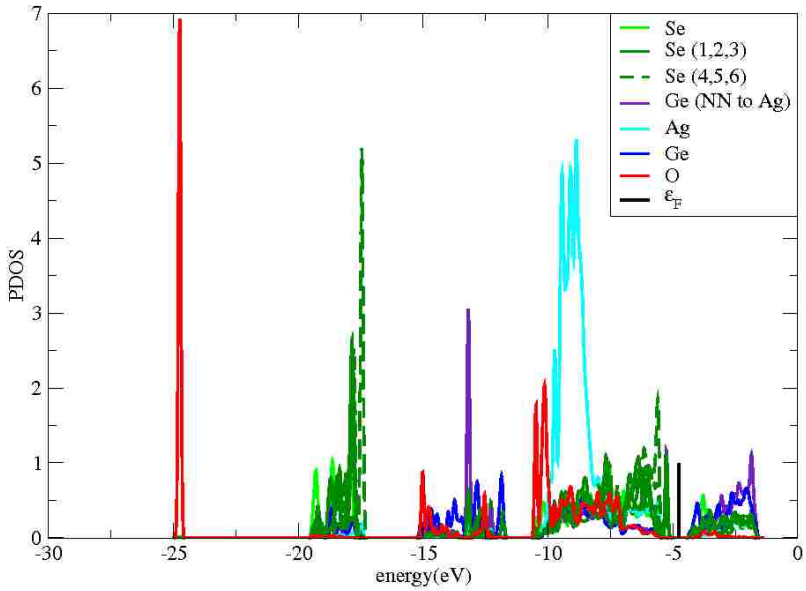

(a) Computed projected density of states.

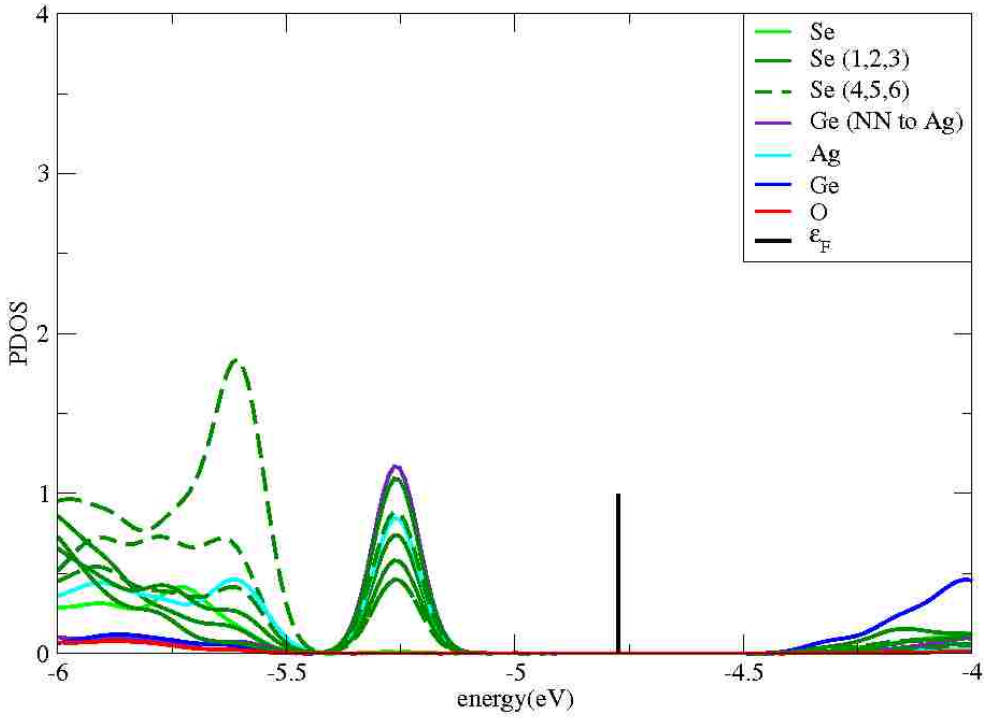

(b) Projected density of states in the band gap region.

Figure 31: Projected density of states of $(BO_{\parallel}{:}Ag_{Ge}{:}I_{Ge})^{(3)}$ configuration, see Figure 26c. The valence band edge is at -5.43 eV and the conduction band edge is at -4.23 eV. The gap state energy is -5.26 eV. The projected densities of states of silver and connected germanium are correlated with their respective nearest neighbor selenium atoms.

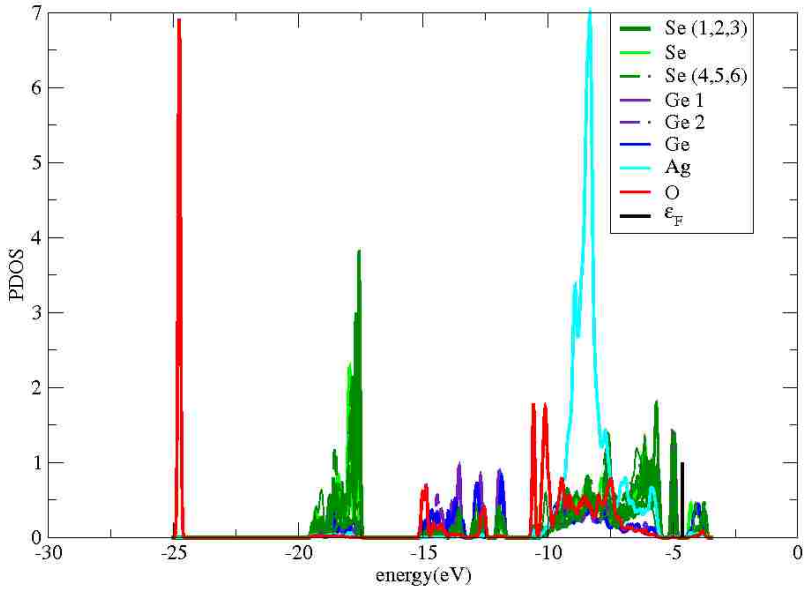

(a) Computed projected density of states.

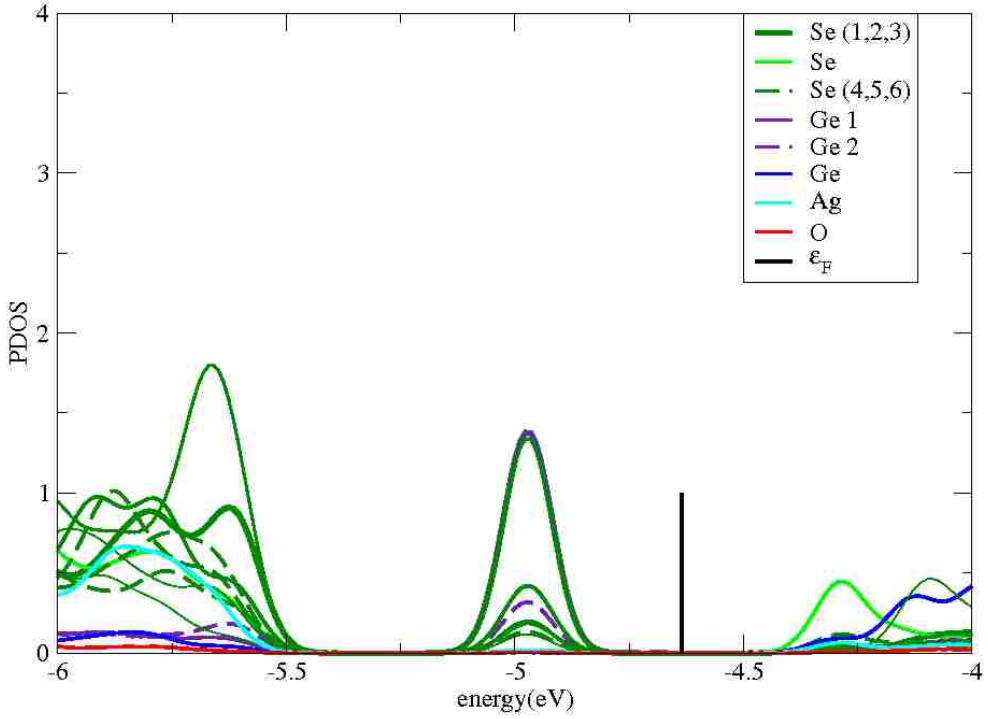

(b) Projected density of state in the band gap region.

Figure 32: Projected density of states of $(BO_{\parallel}{:}I_{Ag}{}^{(2)})^{(2)}$ configuration, see Figure 27b. The valence band edge is at -5.41 eV and the conduction band edge is at -4.49 eV. The gap state energy is -4.98 eV. The projected densities of states of Ge 1 and Ge 2 are correlated with their respective nearest neighbor selenium atoms.

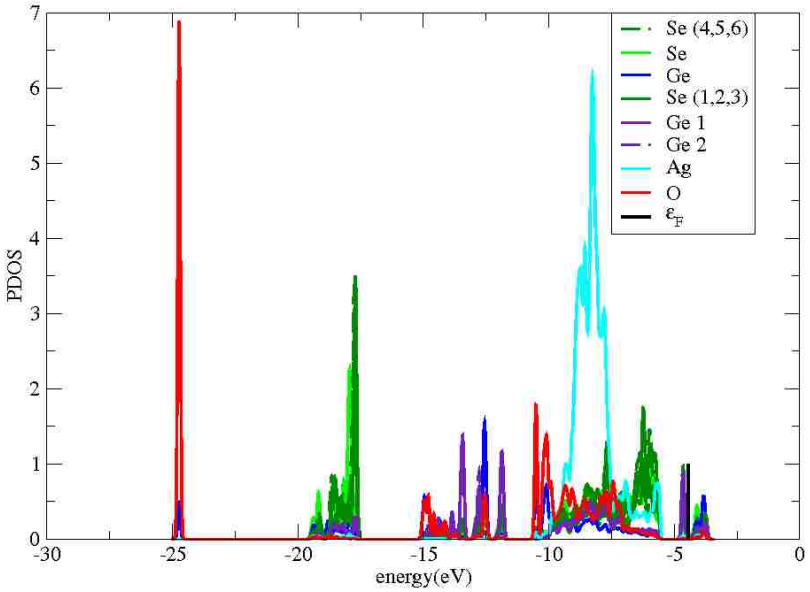

(a) Computed projected density of states.

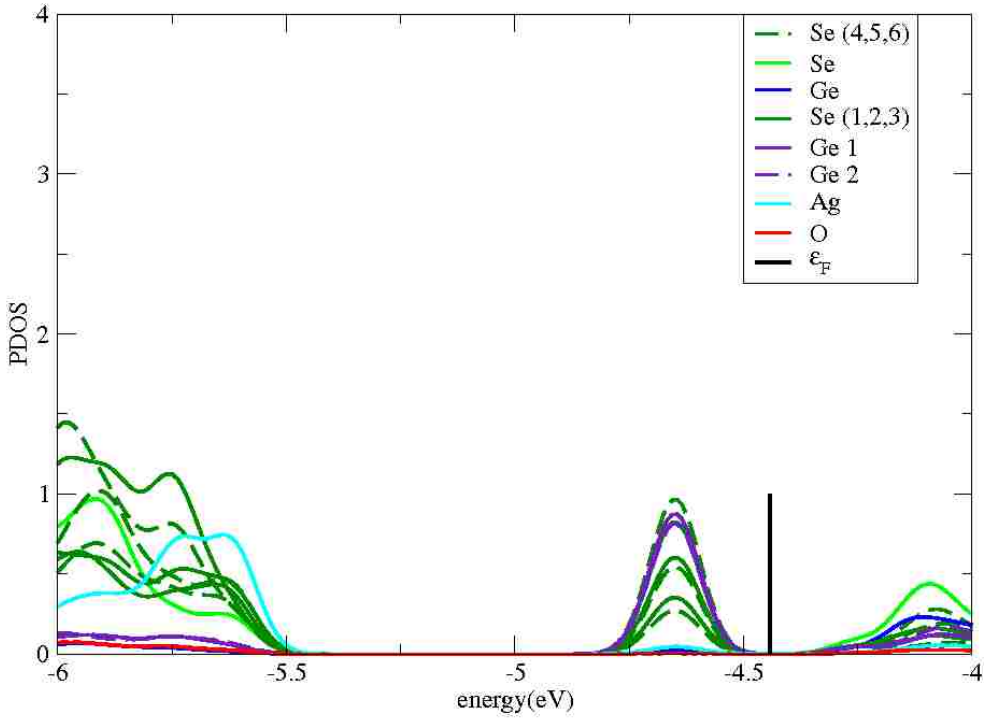

(b) Projected density of states in the band gap region.

Figure 33: Projected density of states of $(BO_{\parallel}{:}I_{Ag}{}^{(2)})^{(3)}$ configuration, see Figure 27c. The valence band edge is at -5.44 eV and the conduction band edge is at -4.41 eV. The gap state energy is -4.65 eV. The projected densities of states of Ge 1 and Ge 2 are correlated with their respective nearest neighbor selenium atoms.

References

1. A. H. Edwards and K. Campbell, "Density functional study of Ag in Ge_2Se_3," 2009 10th Annual Non-Volatile Memory Technology Symposium (NVMTS), 2009.

2. L. Chua, "Memristor-The missing circuit element," IEEE Transactions on Circuit Theory, vol. 18, no. 5, pp. 507–519, 1971.

3. J. Brewer and M. Gill, Nonvolatile Memory Technologies with Emphasis on Flash: A Comprehensive Guide to Understanding and Using Flash Memory Devices. Somerset: Wiley, 2011.

4. A. Thomas, "Memristor-based neural networks," Journal of Physics D: Applied Physics, vol. 46, no. 9, art. 093001, May 2013.

5. S. H. Jo, T. Chang, I. Ebong, B. B. Bhadviya, P. Mazumder, and W. Lu, "Nanoscale memristor device as synapse in neuromorphic systems," Nano Letters, vol. 10, no. 4, pp. 1297–1301, 2010.

6. A. H. Edwards, H. J. Barnaby, K. A. Campbell, M. N. Kozicki, W. Liu, and M. J. Marinella, "Reconfigurable memristive device technologies," Proceedings of the IEEE, vol. 103, no. 7, pp. 1004–1033, 2015.

7. L. Gao, F. Alibart, and D. B. Strukov, "Programmable CMOS/memristor threshold logic," IEEE Transactions on Nanotechnology, vol. 12, no. 2, pp. 115–119, 2013.

8. International Technology Roadmap for Semiconductors, 2007, [online] URL: http://www.itrs2.net/itrs-reports.html. Produced by Semiconductor Industry Association. Emerging Research Devices Chapter.

9. I. Valov, R. Waser, J. R. Jameson, and M. N. Kozicki, "Electrochemical metallization memories—fundamentals, applications, prospects," Nanotechnology, vol. 22, no. 28, art. 289502, Jun. 2011.

10. J. Brewer and M. Gill, Nonvolatile Memory Technologies with Emphasis on Flash: A Comprehensive Guide to Understanding and Using Flash Memory Devices. Somerset: Wiley, 2011. Subsection 13.2.3. Programming Speed.

11. A. Chen, "Ionic memories: Status and challenges," 2008 9th Annual Non-Volatile Memory Technology Symposium (NVMTS), 2008. DOI: 10.1109/NVMT.2008.4731188.

12. C. Gopalan, Y. Ma, T. Gallo, J. Wang, E. Runnion, J. Saenz, F. Koushan, and S. Hollmer, "Demonstration of conductive bridging random access memory (CBRAM) in logic CMOS process," Solid-State Electronics, vol. 58, no. 1, pp. 54-61, Apr. 2011.

13. K. A. Campbell, "Self-directed channel memristor for high temperature operation," Microelectronics Journal, vol. 59, pp. 10–14, 2017.

14. K. A. Campbell, 'Method of forming a memory device incorporating a resistance-variable chalcogenide element,' U.S. Patent no. 7785976, 31-Aug-2010.

15. K. A. Campbell, 'Method of forming a memory device incorporating a resistance-variable chalcogenide element,' U.S. Patent no. 8895401, 25-Nov-2014.

16. A. H. Edwards, K. A. Campbell, and A. C. Pineda, "Self-trapping of single and paired electrons in Ge_2Se_3," Journal of Physics: Condensed Matter, vol. 24, no. 19, art. 195801, 2012.

17. A. H. Edwards, K. A. Campell, and A. C. Pineda, "Electron self-trapping in Ge_2Se_3 and its role in Ag and Sn incorporation," MRS Proceedings, vol. 1431, 2012. DOI: 10.1557/opl.2012.1437.

18. G. A. Slack, L. J. Schowalter, D. Morelli, and J. A. Freitas, "Some effects of oxygen impurities on AlN and GaN," Journal of Crystal Growth, vol. 246, no. 3-4, pp. 287–298, 2002.

19. M. Born and J. R. Oppenheimer, "On the quantum theory of molecules," World Scientific Series in 20th Century Chemistry Quantum Chemistry, pp. 1–24, 2000.

20. A. D. Becke, "Perspective: Fifty years of density-functional theory in chemical physics," The Journal of Chemical Physics, vol. 140, no. 18, 2014. DOI: 10.1063/1.4869598.

21. C. C. J. Roothaan, "New developments in molecular orbital theory," Reviews of Modern Physics, vol. 23, no. 2, pp. 69–89, Jan. 1951.

22. G. Kresse and J. Hafner, "Ab initio molecular dynamics for liquid metals," Physical Review B, vol. 47, no. 1, pp. 558-561 1993.

23. G. Kresse and J. Hafner, "Ab initio molecular-dynamics simulation of the liquid-metal–amorphous-semiconductor transition in germanium," Physical Review B, vol. 49, no. 20, pp. 14251–14269, 1994.

24. G. Kresse and J. Furthmüller, "Efficiency of ab-initio total energy calculations for metals and semiconductors using a plane-wave basis set," Computational Materials Science, vol. 6, no. 1, pp. 15–50, 1996.

25. G. Kresse and J. Furthmüller, "Efficient iterative schemes for ab initio total-energy calculations using a plane-wave basis set," Physical Review B, vol. 54, no. 16, pp. 11169–11186, 1996.

26. R. Dovesi, R. Orlando, A. Erba, C. M. Zicovich-Wilson, B. Civalleri, S. Casassa, L. Maschio, M. Ferrabone, M. D. L. Pierre, P. Darco, Y. Noël, M. Causà, M. Rérat, and B. Kirtman, "CRYSTAL14: A program for the ab initio investigation

of crystalline solids," International Journal of Quantum Chemistry, vol. 114, no. 19, pp. 1287–1317, Nov. 2014.

27. C. Møller and M. S. Plesset, "Note on an approximation treatment for many-electron systems," Physical Review, vol. 46, no. 7, pp. 618–622, Jan. 1934.

28. R. Krishnan and J. A. Pople, "Approximate fourth-order perturbation theory of the electron correlation energy," International Journal of Quantum Chemistry, vol. 14, no. 1, pp. 91–100, 1978.

29. M. Head-Gordon, R. J. Rico, M. Oumi, and T. J. Lee, "A doubles correction to electronic excited states from configuration interaction in the space of single substitutions," Chemical Physics Letters, vol. 219, no. 1-2, pp. 21–29, 1994.

30. D. Maurice and M. Head-Gordon, "Analytical second derivatives for excited electronic states using the single excitation configuration interaction method: theory and application to benzo [a] pyrene and chalcone," Molecular Physics, vol. 96, no. 10, pp. 1533–1541, 1999.

31. D. R. Hartree, "The wave mechanics of an atom with a non-coulomb central field. Part I. Theory and methods," Mathematical Proceedings of the Cambridge Philosophical Society, vol. 24, no. 01, pp. 89, 1928.

32. V. Fock, "Näherungsmethode zur Lösung des quantenmechanischen mehrkörperproblems," Zeitschrift für Physik, vol. 61, no. 1-2, pp. 126–148, 1930.

33. A. Szabó and N. S. Ostlund, Modern Quantum Chemistry Introduction to Advanced Electronic Structure Theory. Mineola (N.Y.): Dover Publications, 1996. Subsection 2.2.4. The Hartree-Fock Approximation.

34. A. Szabó and N. S. Ostlund, Modern Quantum Chemistry Introduction to Advanced Electronic Structure Theory. Mineola (N.Y.): Dover Publications, 1996.

Chapter 4. Configuration Interaction and Chapter 6. Many-Body Perturbation Theory.

35. B. G. Johnson, P. M. W. Gill, and J. A. Pople, "Preliminary results on the performance of a family of density functional methods," The Journal of Chemical Physics, vol. 97, no. 10, pp. 7846–7848, 1992.

36. A. D. Becke, "Density-functional exchange-energy approximation with correct asymptotic behavior," Physical Review A, vol. 38, no. 6, pp. 3098–3100, Jan. 1988.

37. S. H. Vosko, L. Wilk, and M. Nusair, "Accurate spin-dependent electron liquid correlation energies for local spin density calculations: A critical analysis," Canadian Journal of Physics, vol. 58, no. 8, pp. 1200–1211, 1980.

38. W. Kohn and L. J. Sham, "Self-consistent equations including exchange and correlation effects," Physical Review, vol. 140, no. 4A, pp. A1133-A1138, 1965.

39. C. Lee, W. Yang, and R. G. Parr, "Development of the Colle-Salvetti correlation-energy formula into a functional of the electron density," Physical Review B, vol. 37, no. 2, pp. 785–789, 1988.

40. A. Svane, "Hartree-Fock band-structure calculations with the linear muffin-tin-orbital method: Application to C, Si, Ge, and α-Sn," Physical Review B, vol. 35, no. 11, pp. 5496–5502, 1987.

41. A. Grüneis, M. Marsman, and G. Kresse, "Second-order Møller–Plesset perturbation theory applied to extended systems. II. Structural and energetic properties," The Journal of Chemical Physics, vol. 133, no. 7, 2010. DOI: 10.1063/1.3466765.

42. M. Kobayashi and H. Nakai, "How does it become possible to treat delocalized and/or open-shell systems in fragmentation-based linear-scaling electronic structure calculations? The case of the divide-and-conquer method," Physical Chemistry Chemical Physics, vol. 14, no. 21, pp. 7629-7639, 2012.

43. P. A. Schultz, 2017. Private communication.

44. P. A. Schultz, "SeqQuest Electronic Structure Code," SeqQuest Home Page. [Online]. Available: http://dft.sandia.gov/Quest/. [Accessed: 12-Apr-2018].

45. L. H. Thomas, "The calculation of atomic fields," Mathematical Proceedings of the Cambridge Philosophical Society, vol. 23, no. 5, pp. 542-548, 1927.

46. E. Fermi, "Statistical method to determine some properties of atoms," Rendiconti Accademia dei Lincei, vol. 6, pp. 602-607, 1927.

47. P. A. M. Dirac, "Note on exchange phenomena in the Thomas atom," Mathematical Proceedings of the Cambridge Philosophical Society, vol. 26, no. 03, pp. 376-385, 1930.

48. J. C. Slater, "Statistical exchange-correlation in the self-consistent field," Advances in Quantum Chemistry, vol. 6, pp. 1–92, 1972.

49. J. C. Slater, "A simplification of the Hartree–Fock method," Physical Review, vol. 81, no. 3, pp. 385-390, 1951.

50. P. Hohenberg and W. Kohn, "Inhomogeneous electron gas," Physical Review, vol. 136, no. 3B, pp. B864-B871, Sep. 1964.

51. R. G. Parr and W. Yang, Density-Functional Theory of Atoms and Molecules. New York: Oxford University Press, 1989. Section 3.2. The Hohenberg-Kohn Theorems.

52. R. G. Parr and W. Yang, Density-Functional Theory of Atoms and Molecules. New York: Oxford University Press, 1989. Section 3.2. The Hohenberg-Kohn Theorems, Section 3.3. The v- and N-Representability of an Electron Density and Section 3.4. The Levy Constrained-Search Formulation.

53. N. W. Ashcroft and N. D. Mermin, Solid State Physics. Fort Worth: Saunders College, 1988. Chapter 8. Electron Levels in a Periodic Potential: General Properties.

54. F. Bloch, "Über die quantenmechanik der elektronen in kristallgittern," Zeitschrift für Physik, vol. 52, no. 7-8, pp. 555–600, 1929.

55. R. M. Martin, Electronic Structure: Basic Theory and Practical Methods. New York: Cambridge University Press, 2004. Section 4.3. Excitations and the Bloch Theorem.

56. H. J. Monkhorst and J. D. Pack, "Special points for Brillouin-zone integrations," Physical Review B, vol. 13, no. 12, pp. 5188–5192, 1976.

57. R. M. Martin, Electronic Structure: Basic Theory and Practical Methods. New York: Cambridge University Press, 2004. Section 14.1. Localized Atom-Centered Orbitals.

58. R. M. Martin, Electronic Structure: Basic Theory and Practical Methods. New York: Cambridge University Press, 2004. Chapter 11. Summary.

59. M. C. Payne, M. P. Teter, D. C. Allan, T. A. Arias, and J. D. Joannopoulos, "Iterative minimization techniques for ab initio total-energy calculations: Molecular dynamics and conjugate gradients," Reviews of Modern Physics, vol. 64, no. 4, pp. 1045–1097, Jan. 1992.

60. J. P. Perdew, K. Burke, and M. Ernzerhof, "Generalized gradient approximation made simple," Physical Review Letters, vol. 77, no. 18, pp. 3865–3868, 1996.

61. D. R. Hamann, "Generalized norm-conserving pseudopotentials," Physical Review B, vol. 40, no. 5, pp. 2980–2987, 1989.

62. N. Troullier and J. L. Martins, "Efficient pseudopotentials for plane-wave calculations," Physical Review B, vol. 43, no. 3, pp. 1993–2006, 1991.

63. A. Szabó and N. S. Ostlund, Modern Quantum Chemistry Introduction to Advanced Electronic Structure Theory. Mineola (N.Y.): Dover Publications, 1996. Section 3.6. Polyatomic Basis Sets.

64. R. M. Martin, Electronic Structure: Basic Theory and Practical Methods. New York: Cambridge University Press, 2004. Section 11.4. Norm-Conserving Pseudopotentials (NCPPs).

65. G. Henkelman and H. Jónsson, "Improved tangent estimate in the nudged elastic band method for finding minimum energy paths and saddle points," The Journal of Chemical Physics, vol. 113, no. 22, pp. 9978–9985, Aug. 2000.

66. N. W. Ashcroft and N. D. Mermin, Solid State Physics. Fort Worth: Saunders College, 1988. Chapter 8. Electron Levels in a Periodic Potential: General Properties, Section Density of States.

67. R. S. Mulliken, "Electronic population analysis on LCAO-MO molecular wave functions. I," The Journal of Chemical Physics, vol. 23, no. 10, pp. 1833–1840, 1955.

68. M. H. Brodsky, Ed., Amorphous Semiconductors. Berlin: Springer-Verlag, 1985. Section 1.1. Definition of Amorphous Semiconductors.

69. R. Zallen, The Physics of Amorphous Solids. NY: John Wiley & Sons, 1983. Section 1.3. Structure, Solidity, and Respectability and Section 2.1. Introduction: Geometry, Chemistry, and the Primacy of Short-Range Order.

70. B. Prasai, B. Cai, M. K. Underwood, J. P. Lewis, and D. A. Drabold, "Properties of amorphous and crystalline titanium dioxide from first principles," Journal of Materials Science, vol. 47, no. 21, pp. 7515–7521, Mar. 2012.

71. G. Galli, R. M. Martin, R. Car, and M. Parrinello, "Ab initio calculation of properties of carbon in the amorphous and liquid states," Physical Review B, vol. 42, no. 12, pp. 7470–7482, 1990.

72. R. Balian, Kléman Maurice, and J.-P. Poirier, Eds., Physique des Défauts = Physics of Defects. Amsterdam: North-Holland Pub. Co., 1981. Subsection 1.1.3. Classical Liquids and Subsection 1.1.4. Amorphous States

73. A. Madan and M. P. Shaw, The Physics and Applications of Amorphous Semiconductors. Burlington: Elsevier Science, 2012. Section 1.2. Basic Concepts.

74. R. Zallen, The Physics of Amorphous Solids. NY: John Wiley & Sons, 1983. Section 3.4. The 8-n Rule and the "Ideal Glass".

75. W. Zhou, M. Paesler, and D. E. Sayers, "Structure of germanium-selenium glasses: An x-ray-absorption fine-structure study," Physical Review B, vol. 43, no. 3, pp. 2315–2321, 1991.

76. S. Le Roux, A. Bouzid, M. Boero, and C. Massobrio, "Structural properties of glassy Ge_2Se_3 from first-principles molecular dynamics," Physical Review B, vol. 86, no. 22, 2012. DOI: 10.1103/PhysRevB.86.224201.

77. S. Le Roux, A. Zeidler, P. S. Salmon, M. Boero, M. Micoulaut, and C. Massobrio, "Structural properties of liquid Ge_2Se_3: A first-principles study," Physical

Review B, vol. 84, no. 13, 2011. DOI: 10.1103/PhysRevB.84.134203.

78. A. D. Becke, "Becke's three parameter hybrid method using the LYP correlation functional," Journal of Chemical Physics, vol. 98, pp. 5648–5652, 1993.

79. J. P. Perdew, "Density functional theory and the band gap problem," International Journal of Quantum Chemistry, vol. 30, no. 3, pp. 451–451, 1986.

80. P. S. Salmon, "Structure of liquids and glasses in the Ge–Se binary system," Journal of Non-Crystalline Solids, vol. 353, no. 32-40, pp. 2959–2974, 2007.

81. K. Inoue, T. Katayama, K. Kawamoto, and K. Murase, "Electronic structures of GeS_2 in crystalline, amorphous, and Ag-photodoped amorphous phases studied by photoemission and optical spectra," Physical Review B, vol. 35, no. 14, pp. 7496–7504, 1987.

82. L. Skuja and B. Güttler, "Detection of interstitial oxygen molecules in SiO_2 glass by a direct photoexcitation of the infrared luminescence of singlet O_2," Physical Review Letters, vol. 77, no. 10, pp. 2093–2096, 1996.

83. T. Bakos, S. N. Rashkeev and S. T. Pantelides, "Reactions and diffusion of water and oxygen molecules in amorphous SiO_2," Physical Review Letters, vol. 88, no. 5, 2002.

84. K. A. Campbell, 2016. Private communication.

85. D. V. Schroeder, An Introduction to Thermal Physics. San Francisco: Addison Wesley Longman, 2000. Chapter 6. Boltzmann Statistics.

86. S. Arrhenius, "Über die dissociationswärme und den einfluss der temperatur auf den dissociationsgrad der elektrolyte," Zeitschrift für Physikalische Chemie, vol. 4, no. 1, pp. 96-116, Jan. 1889.

87. K. J. Laidler, Chemical Kinetics. New York, N.Y.: HarperCollins, 1987. Chapter 3. The Mechanisms of Elementary Processes, Section The Arrhenius Law

88. E. H. Nicollian and J. R. Brews, MOS (Metal Oxide Semiconductor) Physics and Technology. New York: Wiley, 1982. Subsection 2.2.3. Intrinsic Case.

89. J. W. Morris, Jr., University of California, Berkeley A Survey of Materials Science, Lecture notes, 2007. URL: http://www.mse.berkeley.edu/groups/morris/MSE200/I-structure.pdf. Last visited on 4/16 2018.

90. S. M. Sze, Physics of Semiconductor Devices. New York: John Wiley & Sons, 1981. Section 1.4. Carrier Concentration at Thermal Equilibrium.

91. R. M. Martin, Electronic Structure: Basic Theory and Practical Methods. New York: Cambridge University Press, 2004. Chapter 1. Introduction.

92. P. A. Gigure and O. Bain, "Force constants in hydrogen and deuterium peroxides," The Journal of Physical Chemistry, vol. 56, no. 3, pp. 340–342, 1952.

93. Q. Yan, H. Jain, J. Ren, D. Zhao, and G. Chen, "Effect of photo-oxidation on photobleaching of $GeSe_2$ and Ge_2Se_3 films," The Journal of Physical Chemistry C, vol. 115, no. 43, pp. 21390–21395, 2011.

94. A. H. Edwards, 2018. Private communication.

95. M. Vlček, L. Tichý, J. Klikorka, and A. Tříska, "Influence of oxygen traces on physical properties of glassy $GeSe_2$," Journal of Materials Science, vol. 22, no. 6, pp. 2119–2123, 1987.